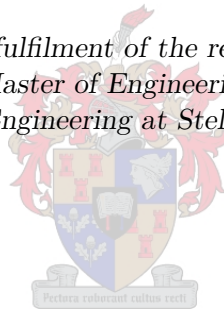


The Deployment of a Spinning Solar Sail

by

Luke Thirkell Hibbert

*Thesis presented in partial fulfilment of the requirements for the degree of
Master of Engineering
in the Faculty of Engineering at Stellenbosch University*



Supervisors:

Dr H.W. Jordaan Prof W.H. Steyn
Department Electrical and Electronic Engineering

April 2019

Plagiarism Declaration

1. I have read and understand the Stellenbosch University Policy on Plagiarism and the definitions of plagiarism and self-plagiarism contained in the Policy [Plagiarism: The use of the ideas or material of others without acknowledgement, or the re-use of one's own previously evaluated or published material without acknowledgement or indication thereof (self-plagiarism or text-recycling)].
2. I also understand that direct translations are plagiarism.
3. Accordingly all quotations and contributions from any source whatsoever (including the internet) have been cited fully. I understand that the reproduction of text without quotation marks (even when the source is cited) is plagiarism.
4. I declare that the work contained in this assignment is my own work and that I have not previously (in its entirety or in part) submitted it for grading in this module/assignment or another module/assignment.

L.T. Hibbert

Initials and Surname

April 2019

Date

Abstract

In recent years, interest in solar sailing has grown greatly, and significant research and resources are being contributed to its development and the development of similar and supporting technologies. Sailcraft utilise large deployable membrane structures to exchange momentum with photons in order to generate thrust from Solar Radiation Pressure. Many small solar sailing satellites make use of three-axis stabilisation and semi-rigid booms, however this design places limits on the sizes of sails possible due to the physical properties of these booms and the size of the deployment mechanisms required. Larger sails are desired in order to achieve greater solar thrust. The use of a spinning solar sailcraft with flexible booms makes it possible to deploy significantly larger sails, as the centrifugal force acts to deploy the sail and maintain the deployment thereof, eliminating the limits enforced by available semi-rigid boom technologies. The low cost and small size of CubeSats may be used to further develop spinning solar sail technology. This thesis focuses on the deployment of a spinning solar sail on a CubeSat platform.

The dynamic equations which describe the behaviour of a spinning solar sailing satellite with flexible booms during- and post- deployment are developed. These equations, which describe the system, are used to investigate the behavioural trends in the deployment under various deployment strategies. Particular focus is given to the passive deployment of the sail booms. No direct active control is placed on the boom deployment in this case; the deployment rate is instead indirectly controlled through the spin rate of the satellite. This is achieved by the application of rotational damping to the pulley on which the booms are stowed and where from they are deployed. Passive deployment cases are investigated where control is based on strategies including free spin, centrifugal force-based control and constant spin rate control. The dynamics of active deployment, where the deployment rate is directly controlled, are also investigated.

An experimental deployment mechanism is designed in order to validate the trends seen in the cases of passive deployment. This experimental deployment mechanism makes use of a geared rotary damper to apply a torque to the pulley from which the booms deploy - this slows the deployment rate with no external inputs. The trends seen in simulation are confirmed where possible. A control algorithm is developed, which is capable of detecting the deployment state of the booms based on the control input supplied to the motor driving the mechanism spin. Based on the deployment state detected, the spin rate of the mechanism can be appropriately adjusted.

Based on the practical experience and insights gained from experimentation, the designs of three deployment mechanisms are presented. Two of the mechanisms designed make use of rotary dampers in different configurations in order to achieve passive deployment. The third mechanism is intended for actively controlled deployment and possess an actuator to control the deployment rate directly. The design takes advantage of centrifugal force, which allows the actuating motor and the mechanism as a whole to be very small in size.

Uitreksel

In die afgelope jare het belangstelling in sonseilvaart gegroei, en beduidende navorsing en hulpbronne word bygedra tot die ontwikkeling daarvan, en die ontwikkeling van soortgelyke en ondersteunende tegnologieë. Sonseil ruimtetuie gebruik groot ontplooibare membraanstrukture om momentum met fotone te ruil, ten einde om stoot van sonstralingdruk te genereer. Die meeste klein sonseil ruimtetuie maak gebruik van drie-as stabilisasie en halfstyf maste, maar hierdie ontwerp beperk die mate van seile moontlik as gevolg van die fisiese eienskappe van hierdie maste en die grootte van die vereiste ontplooiingsmeganismes. Groter seile word verlang om groter sonkrag te verkry. Die gebruik van 'n draaiende sonseil ruimtetuig met buigsame draad-en-massa maste maak dit moontlik om aansienlik groter seile te gebruik, aangesien die sentrifugale krag optree om die seil te ontplooi en die ontplooiing daarvan in stand te hou. Die grense word afgedwing deur beskikbare halfstyf mas tegnologieë. Die lae koste en klein grootte van CubeSats kan gebruik word om sonseilvaart tegnologie verder te ontwikkel. Hierdie proefskrif fokus op die ontplooiing van 'n draaiende sonseil op 'n CubeSat-perron.

Die dinamiese vergelykings wat die gedrag van 'n draaiende sonseil ruimtetuig met buigsame maste, tydens en na die ontplooiing, beskryf word ontwikkel. Hierdie vergelykings, wat die stelsel beskryf, word gebruik om die gedragstendense onder verskillende ontplooiingsstrategieë te ondersoek. Daar word veral gefokus op die passiewe ontplooiing van die seil stelsel. Geen direkte aktiewe beheer word in hierdie geval geplaas op die ontplooiing van die maste nie. Die ontplooiingskoers word in plaas daarvan indirek beheer deur die draaitempo van die satelliet. Ontplooiing word bereik deur roterende demping aan die katrol toe te pas waarop die maste gestoor word en waar van hulle ontplooi word. Passiewe ontplooiingsgevalle word ondersoek waar beheer gebaseer is op strategieë insluitende van: vrye draai, sentrifugale kraggebaseerde beheer en konstante draaitempo beheer. Die dinamika van aktiewe ontplooiing, waar die ontplooiingspoed direk beheer word, word ook ondersoek.

'n Eksperimentele ontplooiingsmeganisme is ontwerp om die tendense wat in die gevalle van passiewe ontplooiing gesien word, te valideer. Hierdie eksperimentele ontplooiingsmeganisme maak gebruik van 'n roterende demper om 'n wringkrag aan die katrol toe te pas waaruit die maste ontplooi - dit vertraag die ontplooiingskoers sonder eksterne insette. Die tendense wat in simulاسie gesien word, word waar moontlik bevestig. 'n Kontroleringsalgoritme word ontwikkel, wat die ontplooiingstoestand van die maste kan opspoor, gebaseer op die kontroleinset wat aan die motor wat die meganisme draaitempo aandryf, verskaf. Gebaseer op die ontplooiingstoestande wat opgespoor is, kan die draaitempo van die meganisme aangepas word.

Op grond van die praktiese ervaring en insigte verkry uit eksperimentering, word die ontwerpe van drie ontplooiingsmeganismes aangebied. Twee van die ontwerpte meganismes maak gebruik van roterende dempers in verskillende konfigurasies om passiewe ontplooiing te bereik. Die derde meganisme is bedoel vir aktief beheer implementering deur 'n aktuator om die ontplooiingsvlak direk te beheer. Die ontwerp maak gebruik van sentrifugale krag, waardeur die aanstuurmotor en die meganisme as 'n geheel baie klein kan wees.

Contents

Abstract	iii
Uitreksel	iv
List of Figures	viii
List of Tables	x
Nomenclature	xi
Acknowledgements	xiv
1 Introduction and Problem Description	1
1.1 Background	1
1.2 Problem Definition	1
1.3 Thesis Layout	2
2 Literature Study	3
2.1 Introduction to Solar Sailing	3
2.2 Sailcrafts: Spinning Versus Three-Axis Stabilised	4
2.3 Sail Structures and Deployment	5
2.3.1 Sail Shapes	5
2.3.2 Boom Construction	6
2.3.3 Sail Membrane Materials	9
2.3.4 Sail Folding	10
2.4 Solar Sailing Missions	10
2.4.1 IKAROS	10
2.4.2 LightSail	11
2.4.3 NEA Scout	13
2.4.4 OKEANOS	14
2.5 Related Applications	18
2.5.1 Drag Sails	18
2.5.2 Deployable Trusses	18
2.5.3 Synthetic Aperture Radar	19
2.5.4 Electric Sails	20
2.5.5 James Webb Space Telescope	20
2.5.6 Breakthrough Starshot	21
2.6 Chapter Summary	21
3 Modelling	23
3.1 Conceptual Sail Model	23
3.1.1 Satellite Form	23

3.1.2	Sail	25
3.1.3	Booms	26
3.1.4	Controlling Deployment	26
3.2	Kinematic Problem	27
3.2.1	System Layout	27
3.3	Lagrangian Mechanics	28
3.4	Double Pendulum Model	29
3.5	Extended Model Deployment	34
3.5.1	Deploying Double Pendulum Model	34
3.5.2	Free Deployment	34
3.5.3	Damped Pulley	35
3.5.4	Boom Winding	37
3.6	Passive Deployment	40
3.6.1	Case 1: Free Damped Pulley Deployment	41
3.6.2	Case 2: Ensured Centrifugal Force Deployment	42
3.6.3	Case 3: Centrifugal Force Management	45
3.6.4	Case 4: Bus Rate Controlled Deployment	46
3.6.5	Passive Deployment Cases Summary	48
3.7	Active Deployment	48
3.8	Practical Deployment	50
3.8.1	Boom Node Elements	50
3.8.2	Booms as Euler Beams	51
3.8.3	Unbalanced Deployment	52
3.9	Influences of Pulley Design	57
3.10	Chapter Summary	59
4	Experimental Deployment Design	60
4.1	Specifications and Requirements	60
4.2	Experimental Architecture	61
4.3	Sensors and Data Acquisition	61
4.3.1	Spinning Sensors	61
4.3.2	Stationary Sensors and Drivers	63
4.4	Experimental Deployment Mechanism Design	65
4.4.1	Pulley Rotational Damping	65
4.4.2	Pulley	67
4.4.3	Boom Wire Path and Tip Mass Seating	67
4.4.4	Experimental Deployment Specifications	68
4.5	Experimental Layout	69
4.6	Experimental Procedure	70
4.6.1	Boom Winding	70
4.7	Chapter Summary	71
5	Experimental Deployment Findings	72
5.1	Manual Control	72
5.1.1	Pulley Static Friction	72
5.1.2	Pulley Constants	73
5.1.3	Deployment Behaviour	74
5.1.4	Bus Rate Spin Controller	77
5.2	Deployment Detection and Control	78
5.2.1	Deployment State Detection	78
5.2.2	Deployment Controller Concept Design	79
5.2.3	Controller Implementation and Results	81
5.3	Chapter Summary	84

<i>CONTENTS</i>	vii
6 Practical and Mechanical Experimental Observations	86
6.1 Lessons Learnt	86
6.1.1 Boom Winding Inconsistencies	86
6.1.2 Pulley Friction	88
6.1.3 Tip Mass Mounting	88
6.2 Revised Mechanical Design	88
6.2.1 Passive Deployment Design	89
6.2.2 Active Design	93
6.3 Chapter Summary	95
7 Conclusions	96
7.1 Modelling and Simulation	96
7.2 Experimental Passive Deployment	97
7.3 Deployment Mechanism Designs	98
7.4 Future Development	98
A Lagrangian Mechanics Derivation Algorithm	100
B Equations of Motion	102
B.1 Single Boom Dynamics	102
B.1.1 Single Boom non-Deploying	102
B.1.2 Single Boom Freely Deploying	102
B.1.3 Single Boom Controlled Deployment	103
B.2 Two Booms Dynamics	103
B.2.1 Two Booms non-Deploying	103
B.2.2 Two Booms Freely Deploying	104
B.2.3 Two Booms Freely Deploying in Inertial Space	105
Bibliography	106

List of Figures

2.1	Maximum SRP Available with Distance from the Sun	4
2.2	Rigid Square Solar Sail	6
2.3	Spin Sail Configurations	7
2.4	Boom Cross Sectional Shapes	8
2.5	Sail Membrane Folding Patterns	10
2.6	IKAROS Spacecraft	11
2.7	The LightSail Spacecraft	12
2.8	The NEA Scout Spacecraft and Deployment Mechanism	14
2.9	OKEANOS Spacecraft	15
2.10	Tape Spring Deployable Structures With Rotary Dampers	19
2.11	CIRES Membrane Radar Antenna	19
2.12	James Webb Space Telescope	21
3.1	Spin Stabilised Sailcraft Configurations	24
3.2	Illustration of the Changing Sail Shape During Deployment	26
3.3	Bus and Four Booms	28
3.4	Rotating Double Pendulum	30
3.5	Response of Simple Damped Double Pendulum Model	33
3.6	Effects of Free Deployment	35
3.7	Pulley Mechanism	36
3.8	Perfect Boom Winding on Pulley	38
3.9	Changing Effective Pulley Radius	40
3.10	Case 1: Free Damped Pulley Deployment	43
3.11	Case 2: Ensured Centrifugal Force Deployment	44
3.12	Case 3: Centrifugal Force Governed Deployment	46
3.13	Case 4: Constant Bus Rate Control	47
3.14	Active Deployment Rate Control	49
3.15	Effects of Deployment and Initial Bus Rate on In-Plane Boom Offset	50
3.16	Multi-Node Boom	51
3.17	Two Boom System	52
3.18	Inducted Body Torque Illustration	53
3.19	In-Plane Boom Offset with Unbalanced Tip Masses	53
3.20	Resultant Sail-Plane Force from Unbalanced Tip Masses	54
3.21	Initial Unbalanced In-Plane Boom Offset Angle: In-Plane Boom Angle	55
3.22	Initial Unbalanced In-Plane Boom Offset Angle: Resultant Sail-Plane Forces	55
3.23	Boom Length with Error Profile	56
3.24	Inconsistent Boom Winding Effects: Resultant Sail-Plane Forces	57
3.25	Inconsistent Boom Winding Effects: In-Plane Boom Angle	57
3.26	Effects of Pulley Design Decisions	58
4.1	Separation of Spinning and Stationary Experimental Aspects.	61

LIST OF FIGURES

ix

4.2	Spinning Sensing Hardware	63
4.3	Stationary Sensing and Control Hardware	64
4.4	Encoder Output Logic Signal Conditioning	64
4.5	Experimental Deployment Mechanism	66
4.6	Rotary Dampers	66
4.7	Experimental Component Stack	69
4.8	Winding Procedure Layout	70
5.1	Determination of Pulley Static Friction	73
5.2	Pulley Rotational Constants Line Fit	74
5.3	Deployed Boom Length Under Manual Control	74
5.4	Experimental Bus Spin Rate Under Manual Control	75
5.5	Focused Bus Spin Rate Behaviour	75
5.6	Simulated Deployment Result With Experimental Parameter Inputs	76
5.7	Spin Controller Output Under Manual Control	77
5.8	Deployment Controller Logic Diagram	80
5.9	Spin Controller Output and Deployment Controller States	82
5.10	Spin Rate with Deployment Controller	82
5.11	Boom Behaviour with Deployment Controller	83
5.12	Deployment Controller; Late Detection	84
6.1	Boom Windings	87
6.2	Proposed Winding Apparatus	88
6.3	Revised Geared Damper Design Exploded View	90
6.4	Pulley Assembly Cross Section	91
6.5	Central Damper Pulley Design Cross Section	92
6.6	Central Damper Pulley Design	92
6.7	Active Deployment Mechanism Design Cross Section	94
6.8	Active Deployment Mechanism Design	95
B.1	Single Boom System	102
B.2	Two Boom System	103

List of Tables

2.1	Sail Membrane Component Properties	9
2.2	Summary of Notable Sail Missions Past, Present and Future	17
3.1	Centrifugal Force Maintained by Select Missions	27
3.2	Methods of Calculating the Length of Wire Wound on a Pulley	40
3.3	Simulation Parameters	41
3.4	Passive Damped Pulley Deployment Case Results	48
4.1	Experimental Deployment Mechanism Specifications	68
5.1	Deployment Progression States	79

Nomenclature

Abbreviations and Acronyms

ADCS	Attitude Determination and Control System
BLE	Bluetooth Low Energy
CFRP	Carbon Fibre Reinforced Polymer
CoM	Centre of Mass
CoP	Centre of Pressure
COTS	Commercial Off The Shelf
CTM	Collapsible Tube Mast
DAQ	Data Acquisition
DC	Direct Current
EM-1	Exploration Mission 1
ESL	Electronic Systems Laboratory
FEM	Finite Element Analysis
IKAROS	Interplanetary Kite-craft Accelerated by Radiation Of the Sun
ISS	International Space Station
JWST	James Webb Space Telescope
JAXA	Japan Aerospace Exploration Agency
JPL	Jet Propulsion Laboratory
LEO	Low Earth Orbit
NASA	National Aeronautics and Space Administration
NEA	Near Earth Astroid
OKEANOS	Outsized Kitecraft for Exploration and AstroNautics in the Outer Solar system
PCB	Printed Circuit Board
PID	Proportional, Integral, Derivative
P-POD	Poly Picosatellite Orbital Deployer

PWM	Pulse Width Modulation
SANSA	South African National Space Agency
SHEARLESS	SHEAth-based Rollable Lenticular-Shaped and low-Stiction
SLS	Space Launch System
SPS	Solar Power Sail
SRP	Solar Radiation Pressure
STEM	Storable Tubular Extendible Member
SAR	Synthetic Appature Radar
TRAC	Triangular Rollable and Collapsible

Greek Letters

β	Bus rotation angle
η	Efficiency
ρ	Density
θ	In plane boom angle
ϕ	Pulley rotation angle
ψ	Threshold
ω	Rotation rate

Lowercase Letters

a	Pulley radii
a_o	Characteristic acceleration
b	Damping
h	Boom wire diameter
k	Winding factor
ℓ	Wire boom length
m	Mass
n	Total number of booms under consideration
\mathbf{p}	Variable vector
r	Distance from bus centre to boom exit point
w	Pulley width

Uppercase Letters

A	Area
-----	------

E	Spin controller output
I	Moment of inertia
\mathcal{L}	Lagrangian
P	Position of bus centre
R	Rayleigh dissipation function
S	Deployment state
T	Kinetic energy
V	Potential energy

Subscripts

0	Initial condition at $t = 0$ s.
b	Bus, referring to spacecraft or deployment mechanism bus or body.
eff	Effective
f	Final, referring to the end state.
i	Boom number
max	Maximum
min	Minimum
p	Pulley
s	Sail
SP	Set point
T	Total
x	x-axis
y	y-axis

Syntax and Style

\mathbf{A}	The matrix \mathbf{A}
\bar{E}	Mean of range of values of E
\dot{y}	First time derivative of y , $\frac{dy}{dt}$
\ddot{y}	Second time derivative of y , $\frac{d^2y}{dt^2}$

Non-Standard Unit Definitions

AU	1 Astronomical Unit or roughly the distance from Earth to the Sun, exactly 149 597 890.7 km
U	1 Unit or 100 mm x 100 mm x 100 mm cubed volume of micro-satellite. Used to classify sizes of satellites based on the CubeSat Standard.
rpm	Revolutions per minute
rps	Revolutions per second

Acknowledgements

In the pursuit of the title of Master of Engineering I have encountered many to whom I owe a debt of gratitude:

Firstly to the friends old and new from the Electronic Systems Laboratory (ESL) who were always there to offer light hearted respite from the toils of attempted academia in the form of coffee breaks, banter and the occasional computer game. Let it not be said that there is never someone in the ESL who will not leap at the opportunity to join one for coffee.

No small thanks is owed to the PCB Lab workshop staff namely: Wessel Croukamp, Wynand Van Eeden, Gift Locobo and Johan Arendse, who assisted in the manufacture of the experimental model and did not complain when tasked with the fabrication of many fine and intricate parts and several iterations of Printed Circuit Boards (PCBs).

Significant thanks is extended towards my supervisors. Willem Jordaan acted as the guiding force for the duration of this project, he provided guidance, direction, motivation and patience (particularly with side projects which may or may not have been in play) when necessary while delivering his own contagious enthusiasm for the topic and those related.

My undertaking of this project would not have been possible without the financial support of the South African National Space Agency (SANSA) who provided me with the monetary assistance to cover my tuition and living costs for the duration of this project. I so thanks SANSA, and particular the liaison there Juchelle Ontong for making this financially feasible.

I would like to thank Erin Hilmer for her support and encouragement at the end of the long days and nights past, although you might have felt that your words of encouragement were in vain they were most definitely not.

Lastly I would like to thank the reader, for without your attention to this work it would have been for naught.

Chapter 1

Introduction and Problem Description

1.1 Background

Within the last decade solar sailing has moved from the realm of science fiction and firmly established itself in reality. Several spacecraft have used solar sailing as a primary means of generating thrust, without the need for propellant, both in Low Earth Orbit (LEO) and interplanetary space. The magnitude of thrust produced by solar sailing is minute compared to what mission and trajectory designers may be accustomed to using, but the key advantage is that this thrust is present wherever there is solar radiation and this thrust is constantly applied. These two distinctions make it advantageous to many missions, particularly those in deep space, as there are fewer disturbance effects which may counteract those of a solar sail.

The useful effect that a solar sail may have is largely dependent on the size of the sail and the mass of the spacecraft. The greater the sail area and smaller the mass the more effective acceleration can be achieved. Large spacecraft require extremely large sails to generate useful thrust which adds significant complications to a mission. One platform to develop the concept of solar sailing as a whole is that of the CubeSat standard. This allows small to medium sized solar sails to be developed and tested at a much lower cost. Many small solar sailing and drag sail missions are presently being actively developed using CubeSats, which use many similar technologies.

Sailcraft can be divided into two distinct categories; spin and three-axis stabilised. The latter consists of common three axis controllers with the appropriate actuators and thrust capabilities as required. These craft require rigid structures to maintain the shape of the deployed sail. Spinning solar sails rather use the centrifugal force generated by the spinning motion to maintain the deployed shape of the sail and may use flexible supporting structures for this reason. The large angular momentum bias inherent in this design lends it far greater stability and disturbance rejection properties over the non-spinning alternative. It does however place limits on how the craft can be controlled and the payloads for which it is suitable.

1.2 Problem Definition

This research aims to investigate the deployment of a spinning solar sail with an understanding of both the theoretical dynamics and practical aspects thereof. This problem encapsulates the following components which require attention for a conclusion to be reached:

- Looking into the current state of the art in solar sailing with particular emphasis on missions, deployment mechanisms and strategies.

- Investigating the deployment dynamics of a spinning solar sail by developing a theoretical model of the system.
- Analysing these dynamics under various deployment strategies, techniques and constraints to understand how the system behaves during- and post-deployment.
- Developing a practical test model of the conceptualised system, to obtain experimental data and compare to simulated trends.
- Based on the lessons learnt from simulation and experiments conducted, refine the hardware design to the state of an engineering development unit suitable for further testing and final refinement.
- Providing conclusions, insights and recommendations for future development of the designed models and hardware.

1.3 Thesis Layout

Having introduced the topic of the thesis in the preceding sections, the layout of the thesis is provided as follows. Chapter 2 will provide a literature review on the basic mechanisms of solar sailing, types and construction of sailcraft, as well as present several notable solar sailing missions and related research regarding deployable space structures and propellant-less thrust. Here particular attention will be given to the constructions and deployment of solar sails and their supporting structures. Chapter 3 introduces the basis for the conceptual satellite which will be used for investigation and the dynamic equations of motion for this system will be derived and investigated under various conditions and deployment strategies. The consequences of design decisions made will be presented as well as their effect on the deployment of the solar sail both in a simulated and practical environments.

Based on the decision path followed in Chapter 3, Chapter 4 will follow the design of an experimental deployment hardware model and its utilisation. In Chapter 5 the results of the experimental findings are presented and how they compare to trends observed in simulated cases is discussed. Based on the lessons learnt in the conducted experiments, practical observations are made and the hardware design is refined and brought closer to a flight-ready form in Chapter 6. Finally Chapter 7 provides closing thoughts and insight into the findings of this thesis. Recommendations for future work, continuation of the project and refinement of the hardware model into a flight ready product are provided.

Chapter 2

Literature Study

The prospect of using the photons emitted from the sun for propulsion in space is not a new one. The potential thereof was first remarked on by Johannes Kepler in 1610 when he noted that comet trails always pointed away from the sun, and theorised that solar radiation pressure may be the cause. He also alluded to the idea which would become solar sailing [1]. Later, in the 1860s, Maxwell's theory of electromagnetism proved that electromagnetic fields had momentum in addition to carrying energy. Upon the discovery that photons of light fall into the category of electromagnetism it was realised that light could impart its momentum to an object, and thus apply a force on that object. The first investigation into the practical application of solar sailing was in the 1970s, when a mission was proposed by Wright [2] to use a spacecraft propelled by a solar sail to rendezvous with Haley's Comet. This proposal was pursued by the Jet Propulsion Laboratory (JPL) but the mission was eventually cancelled due to the agency focusing on other missions, particularly the Shuttle and International Space Station (ISS) programs, as well as funding constraints [2].

In this section the fundamentals of solar sailing will be addressed. The physical principles by which it works will be briefly discussed and the technologies and mechanisms which have been developed will be examined. Notable past, present and future solar sailing missions are presented detailing their working principles, as well as a discussion on similar technologies and where large deployable structures, particularly gossamer, in space are of use.

2.1 Introduction to Solar Sailing

Solar sailing spacecraft refer to those which use Solar Radiation Pressure (SRP) as a primary means of thrust. This is generally achieved by the use of large, thin, reflective membranes which are deployed in space in order to increase the surface area capable of interacting with the photons of light [1]. This is not to be confused with conventional spacecraft that may actively use SRP advantageously. The MESSENGER spacecraft completed several flybys of Mercury and used the effects of SRP to improve the accuracy of its flybys as well as to do momentum dumping from the on-board reaction wheels [3]. Here this method was particularly effective due to the close proximity to the sun. SRP, in most space flight, is seen as a disturbance force. The effect thereof is generally orders of magnitude below that of conventional propulsion systems, on the order of micro Newtons, and thus can be easily corrected for with infrequent applications of propellant. It is thus generally considered to be akin to other environmental forces such as those from gravitational and magnetic fields, atmospheric drag, etc. A notable distinction is that these other disturbance forces vary greatly with location and proximity to other bodies, SRP is generally constant and present at all locations in space.

Photons of light carry with them momentum and can thus impart this momentum on a body.

The amount of momentum transferred depends on several factors such as the spacecraft distance from the sun and the incident surface characteristics such as geometry, temperature and optical properties. The amount of available photons is dependent on the distance from the source, fewer photons result in a lower potential momentum exchange. This effect is illustrated in Figure 2.1, which shows how the maximum available SRP decreases with distance from the sun. Another major factor in the amount of momentum transfer which takes place is the angle at which the photons strike the surface of the sail. The closer to normal the angle of incidence is, the more momentum is transferred by reflection to the spacecraft. More coherent explanations of the mechanics of solar sailing are beyond the scope of this project but Fu *et al.* [1] provides an excellent introduction to the modelling of solar thrust and its application.

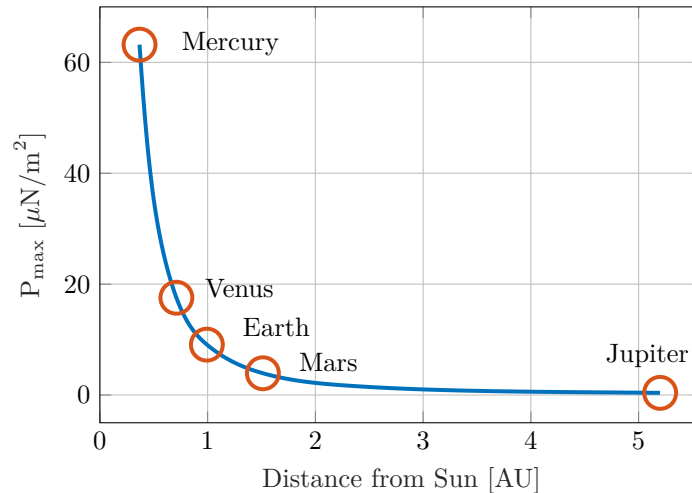


Figure 2.1: Maximum SRP Available with Distance From the Sun. Adapted from Fu *et al.* [1]

The performance of solar sailing craft can be expressed with several methods [4], but the most widely used is the characteristic acceleration defined by McInnes [5] as "light-pressure-induced acceleration experienced by the solar sail while oriented normal to the sun at a heliocentric distance of 1 AU". This fundamental quantity is a measure of the sail areal to mass ratio, expressed as

$$a_0 = \frac{2\eta P A_s}{m_T}.$$

Where m_T denotes the total mass of the spacecraft, A_s the solar sail area, P the magnitude of the SRP on a perfectly absorbing surface at a distance of 1 AU from the sun ($P = 4.568 \times 10^{-6} \text{ N}/\text{m}^2$) and η the sail efficiency which is typically ~ 0.85 . This efficiency is a function of the physical properties of the sail material as well as the sail state once deployed - factors such as sail creases or billowing can have an affect [4, p. 58]. The characteristic acceleration is a convenient quantification for comparing the effectiveness of different sail designs - several spacecraft are later compared in Table 2.2 on page 17.

2.2 Sailcrafts: Spinning Versus Three-Axis Stabilised

For the control of a satellite it is desirable that it is dynamically stable in both its attitude and orbit. Two means by which satellites can achieve stability are by implementing either

three-axis control or spin stabilisation. Three-axis stabilised satellites have minimal to zero rate of spin and, achieve stabilisation by tightly controlling rates in all three axes of rotation. These satellites can achieve relatively rapid attitude changes in any axis but are more sensitive to disturbances. Spin stabilised craft have a large angular momentum which provides stability and disturbance rejection. However, because of this significant angular momentum, attitude changes are slower and require more energy.

Sailcraft which are three-axis stabilised require stiff, rigid booms in order to maintain tension in the sail and prevent its collapsing. As these structures can be large, and the boom materials not perfectly rigid, the rates of attitude adjustments need to be limited in order to prevent buckling of the booms due to their own inertia. Non-spinning craft are well suited to applications requiring accurate pointing ability, for instance optical or earth observation payloads.

The use of spin stabilised craft removes the requirement that the booms of the sail be rigid. The booms and the sail can be deployed and kept so by the centrifugal force generated by the spinning motion. This allows sails of significantly larger sizes as the stiffness of the booms is no longer a limiting factor. The sail is also kept taut by this centrifugal force, reducing billowing and other inconsistencies in the sail surface. This does however add complications to the control of the satellite, and renders spin stable spacecraft unsuited for certain payloads. The greatest disturbance torque experienced by a sailcraft is the Centre of Mass (CoM) to Centre of Pressure (CoP) offset. This disturbance is averaged out over the course of one rotation, which is a significant advantage of spin stabilisation over the three axis variant.

2.3 Sail Structures and Deployment

The construction of a solar sail involves many facets which cover a wide range of disciplines ranging from material science, structural dynamics and advanced manufacturing techniques to origami. Some of the key areas considered in the design of a sail as a system are discussed, as well as potential design choices for the individual aspects of such a system.

2.3.1 Sail Shapes

A wide array of different sail shapes have been proposed - these can differ greatly in shape and control principles. Each requires a different method of deployment and subjects designers to unique challenges. Solar sail designs can be divided into two broad categories; rigid and non-rigid sails. Rigid sails are those which require supporting structure in order to maintain their deployment. Non-rigid sails do not require this structure and instead utilise centrifugal force. For this reason they are also commonly referred to as spin sails. [1]

2.3.1.1 Rigid Sails

The sail membrane can be kept deployed and taut by stiff supporting members to which the membrane is attached. There can be any number of members supporting a number of sail segments, and thus rigid sail designs can vary greatly in complexity, size, and functionality. One of the most commonly used designs is a square sail or clipper (Figure 2.2), comprising of either segments or a single piece of material, and mounted on a non-spinning platform by the use of deployable semi-rigid booms. Spacecraft such as LightSail [6] and Near Earth Astroid (NEA) Scout [7] used this design.

Variations of this concept include examples such as the quad and butterfly types. These designs are made up of individual constructions of sail segments mounted to rigging. This increases the complexity and mass fraction of the sail mechanism, but has the potential to offer greater control authority as the segments are individually articulated. These designs

scale well, to a point, and the stiff supports assist in minimising membrane deformation and billowing by maintaining tension on the sail. A reduction in sail surface defects has the potential to greatly increase the sail efficiency and decrease disturbance forces. [1]

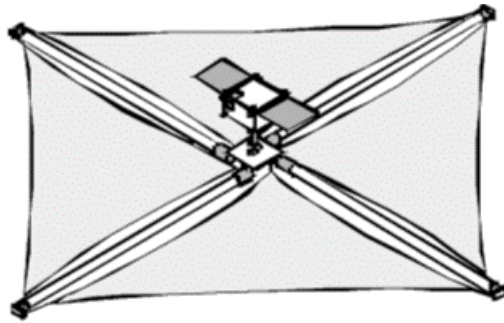


Figure 2.2: Rigid Square Solar Sail. [8; 9]

2.3.1.2 Spin Sails

Spin sails utilise the centrifugal force produced by a spinning spacecraft or a spinning portion of a craft. This eliminates the need for supporting members reducing the mass and volume of the sail mechanics. Spin sails are discussed in two categories: disc and heliogyro sails.

Heliogyro sails are composed of long individual rectangular segments or blades, which have lengths orders of magnitude greater than their widths as illustrated in Figure 2.3b. These rectangular segments are arranged symmetrically around a central rotating hub. The blades have masses along the outer narrow edges in order to maintain stiffness in the membrane, and to assist unrolling deployment of the blades. The blades can be made such that they are able to rotate around their longitudinal, axis allowing the magnitude and CoP of the solar thrust to be controlled.

Disc sails, Figure 2.3a, refer to spinning solar sails where a central hub or bus is surrounded by a large sheet of sail material. Although referred to as a disc sail, the geometry can take any shape. Hereafter disc sails will be referred to by the shape of the sail along with the mention that it is of the spinning persuasion. These disc sails use flexible booms made of wire or cable with masses attached at the tips. The sail membrane is attached at the tip and/or on sliding rings along the lengths of the boom. The use of wire booms makes it possible to fit exceedingly large booms into a compact volume and use mechanically simple deployment mechanisms.

Spinning sails have the potential to be far greater in size than rigid boom alternatives, as constraints such as boom stiffness are not as influential. Disturbances caused by imperfections in the sail are mitigated by the spinning nature of the craft as net disturbance torques are mitigated over the course of a revolution. A large spinning sail may have a moment of inertia similar to that of the spacecraft body; while this does improve stability, it also presents attitude control issues.

2.3.2 Boom Construction

Deployable structures in space are not a new concept, and are often used for things such as de-orbit devices, antenna, solar arrays and attitude control mechanisms, that being said, the size and load requirements of these deployable structures differ vastly with technology, application and mission. In the case of deploying solar sails the design constraints are more

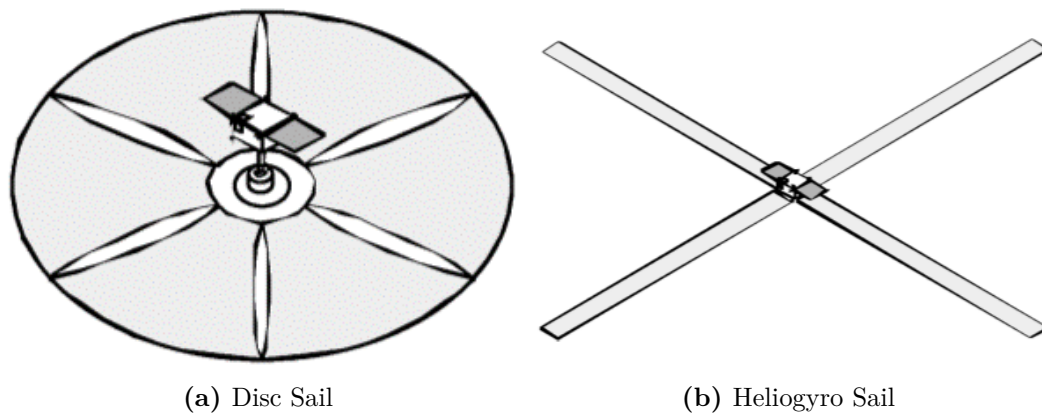


Figure 2.3: Spin Sail Configurations [8; 9].

challenging to realise, as the size of the deployable structure is vastly greater than that of the spacecraft body. This places more emphasis on reducing the mass of both the deployed structure as well as the associated deployment mechanism. Many solutions to this problem have been devised to suit a variety of mission types and sizes.

The deployment structure of solar sails can be broadly sorted into two distinct categories: semi-rigid and flexible booms. Semi-rigid implies that the sail booms are rigid once deployed but can be compactly stowed, while flexible booms require a constant force to be applied in order to maintain their shape. While fully rigid solutions such as telescopic booms do exist, these will not be discussed as they are limited to smaller structures, are bulky when stowed and generally have a high mass, making them unsuited for use in solar sailing applications. Some notable sail supporting structures are listed here for reference:

1. Flexible booms are thin wire members generally with masses attached at the boom tips. The wire is kept taut through centrifugal force, and thus requires the spacecraft to be constantly in a spinning state around the axis normal to the sail plane. The centrifugal force may also act as the driving force behind deployment, by pulling the coiled wire boom from the spacecraft body. The boom can be released through either active or passive means, but is generally actively released in a stepped fashion as this allows more control of the deployment process. A higher spin rate is often required at the start of the deployment process in order to provide sufficient centrifugal force, as well as to maintain the angular momentum of the spacecraft as its inertia increases.
2. Bi-stable tape springs pack tightly and have very predictable deployments. These consist of a thin coiled spring with an arced cross-section akin to that of a common tape measure (Figure 2.4a).
3. Non-bi-stable thin shelled booms cover a variety of cross-sectional shapes (Figure 2.4b-d). These type of booms tend to have significant stored energy when in the stowed position allowing them to self deploy to an extent. This leads to the requirement of highly effective methods of restraint in order to prevent unwanted boom deployment. The most notable types are [10; 11]:
 - A Storable Tubular Extendible Member (STEM), which has a hollow circular cross section. It can be rolled flat to be stowed and takes shape once deployed.

- A Collapsible Tube Mast (CTM), which is made of two bonded strips in the shape of omega symbols and which, while similar to the STEM, has a greater rigidity because of the flat sections.
- A Triangular Rollable and Collapsible (TRAC), which is similar to two of the bi-stable tape springs laser welded together and forming a 'V'-like shape offering greater rigidity.

Non-bi-stable booms require active deployment and can offer high boom rigidity at shorter spans, making them highly suitable for small- to medium-sized sails on non-spinning craft. Those with a hollow cross section and solid walls can be pressurised with gas to further improve their rigidity. These, however, are not favoured for very large sails as their stowed size, mass and energy become problematic. Buckling of the booms also becomes a major factor of concern for long extended boom lengths. Advancement in the use of composite materials could make this option more attractive in the future. Carbon Fibre Reinforced Polymer (CFRP) is becoming the preferred material for rigid booms [12]. Composite booms such as the Bi-TRAC boom are being developed where the two bonded halves are made to have differing material properties. This is an effort to increase the rigidity of the members in the deployed state which allow for compact stowage and winding of the boom with decreased potential energy [13].

4. SHEAth-based Rollable Lenticular-Shaped and low-Stiction (SHEARLESS) booms are lenticular/biconvex in shape. They are constructed by combining two tape springs face to face, and enveloping them in bonding sheath, Figure 2.4e. This sheath can be wound around the boom, can form a solid tube or be a braided sleeve. The tape springs are made from a metal, though recently composite materials have been used, while the outer sheath is made from a polymer such as Kapton[®]. These booms have a low potential energy when in the stowed configuration, but offer many similar favourable qualities to bi-stable booms. [13]

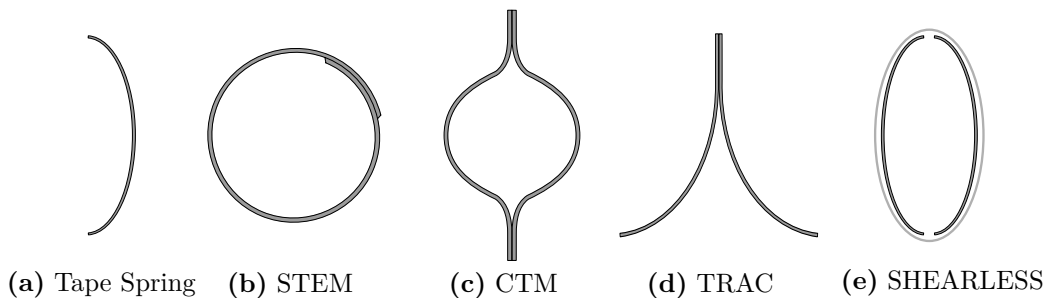


Figure 2.4: Boom Cross Sectional Shapes. Partially adapted from Parera [11]; Fernandez [13]

Semi-rigid booms see more use on small spacecraft, as the deployment is more predictable and the craft more controllable post-deployment. The requirement to have a spinning craft for flexible booms complicates the design of the satellite but does allow for far larger sails to be deployed. There are many variations of semi-rigid booms under development such as the SHEARLESS booms which combine aspects of different boom shapes, materials, manufacturing techniques and cross-sectional layout, the hybrid self-deployable Tubular CFRP boom by Chubachi *et al.* [14] is an example of this.

2.3.3 Sail Membrane Materials

The composition of the sail membrane is an important design consideration and has a direct impact on the performance of a sailcraft. Several aspects are considered when choosing the make-up of the sail membrane or film, including the base substrate and the reflective coating applied. Sail membranes are generally made by coating a substrate polymer film with a metallic material such as aluminium. The substrate material provides a base for manufacture and the strength for the thin and fragile material to withstand handling, folding and other stresses it may experience during testing and deployment. The metallised material is still extremely fragile and prone to tearing, which could severely impact sail performance. Thermal considerations are also of importance as the sail is so thin that thermal changes can be considered instantaneous. Dimensional thermal stability is important as the sail tension may vary to an unacceptable degree affecting aspects such as sail billowing and causing addition wear at connection points and fold lines. [4, p. 60]

Popular materials for the sail membrane substrate material include Kapton[®], Mylar[®] and Lexan[®]. Kapton[®] is the most commonly used material as it is highly stable both chemically and thermally, and has a high resistance to UV and radiation degradation [4, p. 61].

The metallic coating provides the reflective properties for the sail which eventually allow for the solar thrust to be generated by reflecting photons. A light, thin coating with a high reflectivity is desired. Candidates for this purpose include aluminium, lithium and silver. Lithium has a relatively low melting point. Silver has a high density and is transparent in the UV spectrum, making aluminium the popular and preferred choice for coatings [4, p. 63]. Sails may also require an additional back coating to assist in the dissipation of heat and aid in maintaining thermal equilibrium in the sail membrane. The metallic coating is often applied in a vapour deposition process. The sail base substrate is generally approximately $2 \mu\text{m}$ thick and the coating $0.1 \mu\text{m}$. Table 2.1 provide some information on sail substrates and coatings. It can be seen that solar sails can easily have an areal mass density of 3.11 g/m^2 or less.

The metallised sail surface can develop imperfections in the form of bubbles when exposed to the high energy solar wind. This causes the sail surface to become uneven, which has a direct detrimental influence on the sails thrust performance by altering the optical properties of the membrane. Research is under way to develop coatings that alleviate this degradation [15].

Table 2.1: Sail Membrane Component Properties. Information gleaned from McInnes [4].

Material	Density [g/m ³]	Typical Thickness [μm]
Kapton	1.42	0.4-7.6
Mylar	1.38	
Lexan	1.2	
Aluminium	2.7	0.1-0.5
Lithium	0.53	
Silver	10.5	

2.3.4 Sail Folding

The method of folding used to stow and deploy the sail can have implications on the design of the deployment mechanism and the strategies of deployment used. The sail membrane needs to be folded in such a manner that it can easily be unfurled by the deployment of the booms but also that creasing, wear and tearing are minimised to the greatest extent possible. This has led to the development of several folding strategies and patterns. The pattern used is generally determined by the size of the sail and satellite, the deployment mechanism and deployment strategy used. An in-depth review of folding techniques is beyond the scope of this work but attention should be given to the potential options and the implications when considering the integration of satellite and deployment mechanism.

Examples of common folding patterns include tree leaf, Miura-ori, frog leg, spiral and modified spiral which are illustrated in Figure 2.5 [1].

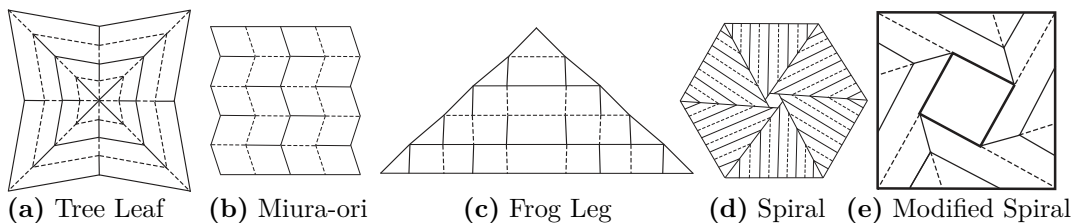


Figure 2.5: Sail Membrane Folding Patterns [1]

2.4 Solar Sailing Missions

Solar sailing has only recently fully moved from the realm of science fiction and into reality, predominantly in the form of technology demonstration missions. These, however, have not been without additional scientific purpose. These missions have laid the way for many subsequent projects, both in the form of direct successors and innovative new mission proposals. Some of these are here presented in some detail and more are listed in Table 2.2 on page 17.

2.4.1 IKAROS

Interplanetary Kite-craft Accelerated by Radiation Of the Sun (IKAROS) was the first ever solar sailing craft to be used in interplanetary space. It was developed and launched by Japan Aerospace Exploration Agency (JAXA) on 21 May 2010 as a secondary payload with AKATSUKI, the Venus Climate orbiter. It was dubbed by the Japan Aerospace Exploration Agency (JAXA) as the first Solar Power Sail (SPS) to fly, as in addition to using its sail to produce solar thrust it was also used to generate electrical power.

IKAROS used a spinning solar sail design with flexible booms which were deployed through centrifugal force produced by the spacecraft spin. The spin rate of the craft was controlled through the use of gas thrusters mounted to the satellite body, and this in turn was used to facilitate the various sail deployment stages. The sail consisted of 10 m flexible booms, as mentioned, with 500 g tip masses. The primary sail material used was polyimide with a thin aluminium coating on the sun-facing side to increase the reflectivity of the sail. The square sail had a length of 14 m per side [16].

Notable technology demonstrations of this sail were the thin film solar cells and steering devices built into the sail membrane. Approximately 5 % of the sail area was covered in thin film flexible solar cells to generate electrical power. These cells combined were capable

of generating almost 300 W of electrical power. This was intended as a technical validation for use on the successor to IKAROS, which will use a large array of sail mounted solar cells to generate electricity for a high impulse ion drive (discussed later). In order to control the attitude of the spacecraft the CoP to CoM of the craft was manipulated through altering the reflective properties of the sail membrane itself. Liquid crystal films were embedded on the outer edges of the sail. The manner in which the light was reflected off the sail was altered by the state of these liquid crystal films. By changing the on/off state thereof the light would either be reflected secularly or diffusely, thus changing the centre of pressure on the craft and generating control torques.

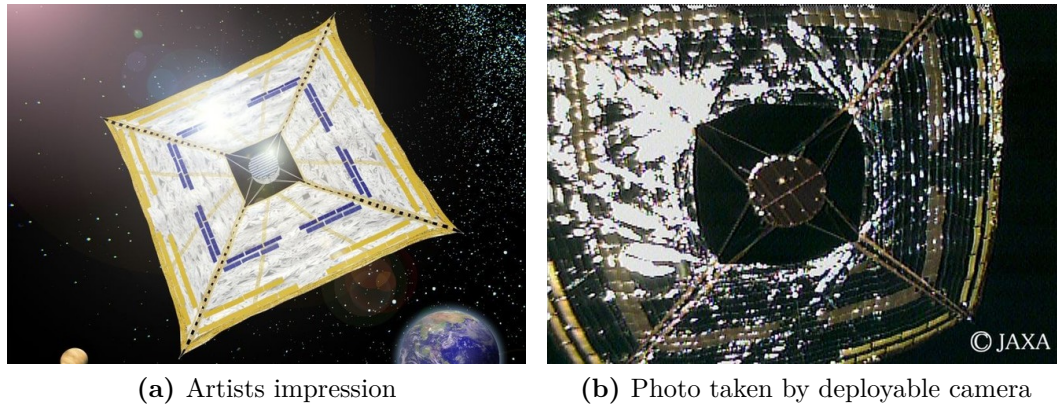


Figure 2.6: IKAROS Spacecraft [16]

Deployment of the sail was conducted in three stages. Firstly the craft's spin rate was decreased to 2 rpm, at which point the tip masses and a portion of the booms were released in a yo-yo de-spin like manner. Secondly, the spin rate was increased to 25 rpm in order to intensify the centrifugal force on the tip masses. The tip masses were pulled outwards by this force unwrapping the sail from the spacecraft body quasi-statically as the deployment rate was controlled by gradually releasing the sail membrane in-line with the booms. The majority of the sail was still constrained during boom deployment, once the booms were fully deployed the sail formed an 'X' shape. During this procedure the spin rate of the craft was decreased to 5 rpm. Lastly the remainder of the sail membrane is released and, due to the centrifugal force, takes on its deployed square shape.

Images of the booms and sail were captured both during and post deployment (see Figure 2.6b), the shape of which found to closely match that as predicted in simulation. JAXA has since updated its dynamic models of how the sail will deploy to very closely match that which was observed on IKAROS for use on future missions. [17; 16]

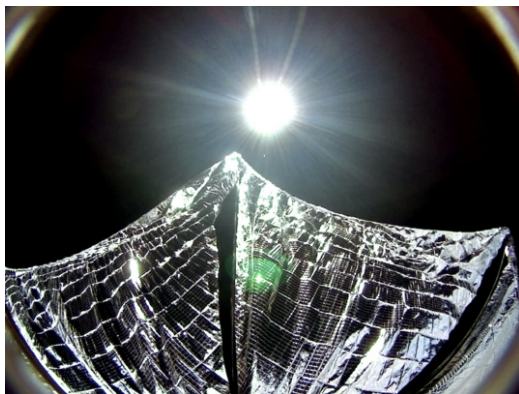
2.4.2 LightSail

In 2009 LightSail was commenced as a mission program by The Planetary Society in order to push development of solar sailing technologies [18]. The mission consists of two very similar CubeSat platforms: LightSail-1 and LightSail-2¹. Both spacecraft consist of 3U CubeSats which were funded using crowd sourcing. Within the volume of each satellite: 1U was assigned for the flight computer, avionics, Attitude Determination and Control System

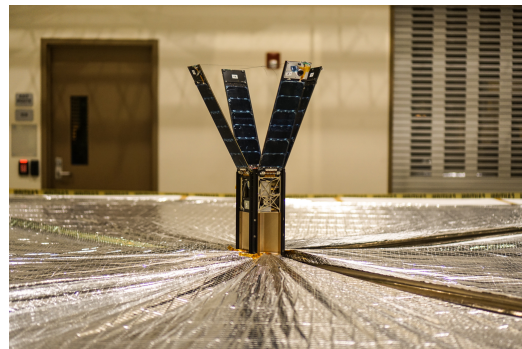
¹Some texts refer to the spacecraft as they were formally known: LightSail-A and LightSail-B respectively [1; 19].

(ADCS) etc., and 2U to the solar sail including the sail storage, deployment mechanism, actuating motor and gear train. Attitude control was achieved through three torque rods and a single momentum wheel. The craft were designed to be deployed from a Poly Picosatellite Orbital Deployer (P-POD). The four long sides of the spacecraft were fitted with dual sided deployable solar panels, which served to retain the sail within the spacecraft body pre-sail deployment and thus were not extended until sail deployment was to commence. On the tips of two opposing panels were cameras poised to capture images of the sail as in Figure 2.7a. This provided valuable insight into how the sail behaved during and after the deployment procedure.

The LightSail spacecraft were fitted with 32 m^2 sails and deployed with 4 m semi-rigid TRAC booms on a non-spinning platform. The extension of the booms was driven by a brushless DC motor and an accompanying worm gear drive reduction. This worm gear provided the necessary gearing reduction required to drive the deployment spindle. It also retained the booms in place when the motor was not energised, as the gearing could not be back-driven. This was important as the boom design used had significant stored strain energy when in the stowed position. The sails were folded and stowed in such a way that they were held in place by friction and during deployment the consecutive folds in the sail material were pulled out by the booms. LightSail-2 during a deployment test is pictured in Figure 2.7b. The sail-boom attachments were made with tension spring connections at the boom tips. These ensured that acceptable tension on the sail was maintained during thermal cycling. Biddy and Svitek [10] provide a detailed description on the design and qualification of the LightSail deployment mechanism.



(a) LightSail-1 with deployed sail taken from solar panel mounted camera [6]



(b) Deployment Test of LightSail-2. Credit: Justin Foley/Cal Pol/The Planetary Society

Figure 2.7: The LightSail Spacecraft

LightSail-1 was completed, tested and ready for flight in 2011 but due to the lack of an appropriate and viable launch opportunity the mission was temporarily shelved. In 2013 the mission was rejuvenated with altered objectives. LightSail-1 would validate the in-orbit deployment and functionality of the CubeSat platform and solar sail while LightSail-2 would demonstrate control and thrust using the solar sail in LEO by raising its orbit apogee. These changes in objectives allowed LightSail-1 to utilise more launch opportunities as it could fulfil its mission objectives at lower altitudes where drag effects outweighed those of solar thrust [6].

LightSail-1 was launched in May 2015 on an Atlas 5 rocket and deployed from a P-POD two hours after launch. Amidst several near terminal faults the mission was recovered to a point where sail deployment could be attempted. Deployment took place over the course of approximately two minutes and the image in Figure 2.7a was captured, visually confirming a successful deployment. An unrecoverable communications error three days after deployment effectively ended the mission for LightSail-1 but all objectives had been achieved and the mission deemed a success. LightSail-1 re-entered the atmosphere and burned up seven days after sail deployment. [6]

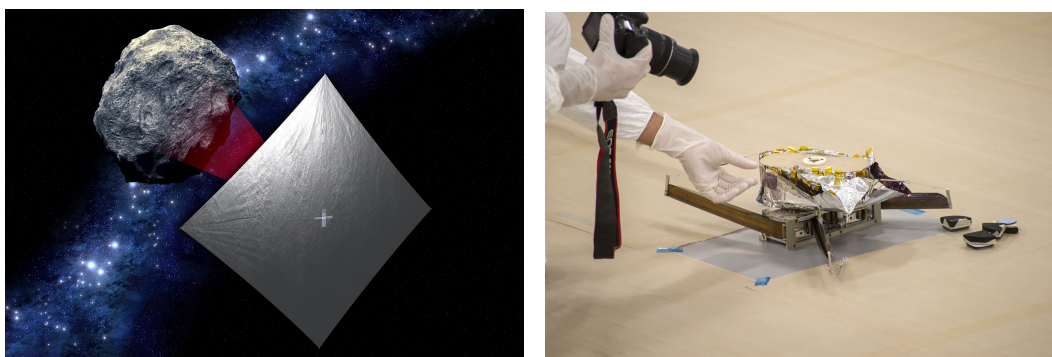
LightSail-2 will launch on the first commercial flight of the SpaceX Falcon Heavy Rocket along with Prox-1 as a secondary payload to the Space Test Program 2 mission. LightSail-2's primary mission is to demonstrate the controlled use of solar thrust to change its orbit. The spacecraft will be deployed from an integrated P-POD on board the Prox-1 micro-satellite. Prox-1 was designed to test proximity operations in relation to a CubeSat and LightSail-2 is the subject matter of the Prox-1 mission. After LightSail-2 is deployed Prox-1 will rendezvous with LightSail-2 and enter a trailing orbit approximately 200 m behind LightSail. It will then perform station keeping and circumnavigation procedures around LightSail. Deployment will be commenced and LightSail-2 will use its solar panel mounted cameras to capture images of the sail during and post deployment. Prox-1 will also be acquiring images during this 2.5 min event in both the visible and infra-red spectrum from a range of about 75 m. After sail deployment solar sailing will commence for a period of about 12 days. Every orbit period two 90° slew manoeuvres will be conducted in order to increase the orbit energy of the space craft and raise its apogee altitude by an estimated 500 m to 700 m per day. The perigee altitude will however degrade due to aerodynamic effects. [20]

2.4.3 NEA Scout

National Aeronautics and Space Administration (NASA) is developing a mission to conduct a reconnaissance expedition of one or multiple Near Earth Asteroids (NEAs) dubbed NEA Scout. The primary purpose of this mission is to expand on the current knowledge of NEAs and potentially gain enough information to assess the viability of manned missions to visit these asteroids as it may be technically feasible to attempt this in the near future [7]. The mission will form part of the secondary payload of the Exploration Mission 1 (EM-1) launch atop the first flight of the Space Launch System (SLS) rocket currently under construction and development. EM-1 will be performing a lunar flyby in order to test the new Orion Crew Capsule. The launch date is currently set for November 2019, dependent of the manufacture of the rocket and EM-1 mission components [21].

NEA Scout aims to conduct multiple flybys of NEAs at distances of less than 1 km in order to obtain information from in-situ visual observations [7], Figure 2.8a. NEA Scout will take the form factor of a 6U CubeSat. This is to demonstrate the capabilities of these small craft and what they can achieve at relatively low costs. Upon separation from the rocket upper stage, NEA Scout will use cold gas thrusters to enter an orbit for a lunar flyby. Once the spacecraft is stable and the lunar flyby complete the solar sail will be deployed and characterised. It will take the craft approximately 2.5 years to reach its first target using solely the thrust generated by the sail. By placing several constraints on possible target NEAs and using a mission duration limit of 10 years Piloni *et al.* [22] has found several trajectory paths that could visit up to five asteroids using the low thrust propulsion of a solar sail, a task that would require a significantly larger propulsion system and spacecraft using more traditional methods of achieving thrust. The ADCS consists of reaction wheels, star tracker, sun sensors and an active mass translator in addition to the sail.

The design of the solar sail and its deployment mechanism builds on the technology and methods used by previous demonstration missions such as LightSail-1 and NanoSail-D. The 6U CubeSat will have a final mass of <14 kg. As with the afore mentioned demonstration



(a) Artists Impression of NEA Scout [7]

(b) Deployment Mechanism During a Full Scale Deployment Test. Credit: NASA/MSFC/Emmit Given

Figure 2.8: The NEA Scout Spacecraft and Deployment Mechanism

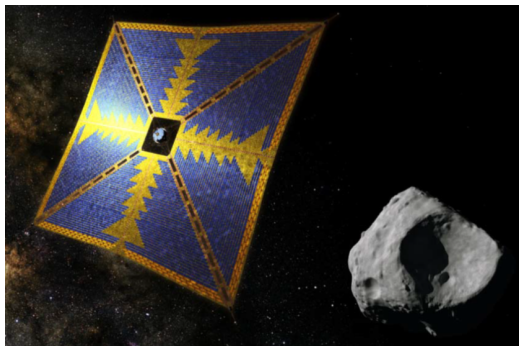
missions NEA Scout will have TRAC booms but a larger sail area of 86 m^2 on 7.2 m booms [23] which will take an estimated time of ~ 30 minutes to deploy [24]. The sail deployment will be actuated by a geared stepper motor; because of the stored strain energy within a stowed TRAC boom the motor will act more to retain the booms during deployment rather than driving them out, although it can serve both functions. Unlike its predecessors, NEA Scout's sail will be made of a single piece of $9.2 \text{ m} \times 9.3 \text{ m}$ sail material as opposed to the four separate triangular quadrants previously used. As the booms here are significantly longer, thermal deformation proved to be a serious issue. Simulation showed that a single boom without an attached sail could undergo a tip displacement of 1.48 m . It was determined that moving to a single piece sail design would shade the booms from direct heating, as well as have the added benefits of increasing sail flatness and decreasing the number of sail connection points required [24]. A photo taken at the commencement of a deployment test can be seen in Figure 2.8b.

NEA Scout serves as a very good example of the exceptional difficulties in the design, development and testing of a solar sail on the ground where air resistance and gravity are major hindrances. Deployment tests of NEA Scout proved highly challenging to conduct because of the interferences of gravity and the complications induced by the methods used to counteract this. One solution is to perform scaled tests of the deployment - while this potentially lessens the undesired effects of gravity and friction the results of these tests can be challenging to scale up, as was discovered by Few *et al.* [23]. While conducting deployment tests the prospect of how to offload the gravity effects was far more prominent than previous spacecraft with similar deployment means because of the greater size. Due to the long boom lengths, bucking of the booms during deployment tests proved to be a great issue. The added friction from the methods used to provide gravity offload as well as from friction between the sail membrane and the testing surface was the cause of this.

2.4.4 OKEANOS

The mission successor to IKAROS is Outsized Kitecraft for Exploration and AstroNautics in the Outer Solar system (OKEANOS), a mission under development by parties from both Japan and Europe. This mission will build on the technology demonstration that was IKAROS, and will include a multitude of scientific payloads. The primary mission is to rendezvous with a Jupiter Trojan asteroid, around the Sun-Jupiter Lagrange points [25; 26].

There will be two distinct science missions on-board OKEANOS: a cruising science mission en-route to the asteroid and a Trojan asteroid science mission. The cruising science mission will last about 13 years and will involve gravity assists from both Earth and Jupiter. Experiments such as the measurement of interplanetary dust, magnetic fields, detection of gamma-ray events as well as a telescope to map zodiacal lights will be active during this phase of the mission. Upon arriving at the Trojan asteroid remote measurements will be taken of the asteroid in order to determine properties such as shape, spin rate and gravity. A landing site will be determined for a lander payload which will be responsible for taking a number of surface measurements using an array of instruments, including several microscopy technologies and optical instruments such as cameras, laser range finders and surface and subsurface samplers. The mission is scheduled to launch in the mid 2020s. Under investigation at present is the possibility of expansions to the mission, including rendezvousing with an additional Trojan asteroid and conducting the remote measurements possible there before moving on to the primary target. This will add 6 to 10 years to the mission duration. Another aspect under investigation is a sample return from the asteroid. The feasibility of this is being considered and will be heavily dependent on the design of the re-entry capsule for the samples. This will extend the mission into the late 2050s. [25]



(a) OKEANOS Mission Artists Impression [26]



(b) 50 m Engineering Model Sail Quarter Segment [27]

Figure 2.9: OKEANOS Spacecraft

As with its predecessor, the spacecraft will be equipped with a SPS in order to provide thrust as well as generate electrical power. The use of a sail allows for an uncommonly large surface area for power generation which will be used to power an ion engine, making the craft a hybrid in terms of propulsion system. The system is intended to be capable of generating up to 5.6 kW at ~ 5.2 AU using only the SPS [27]. As with IKAROS, the sail will be partially covered in flexible solar cells, although a far greater portion of the sail area will be used and the outer edges of the sail will have the liquid crystal films in place for attitude control (seen in Figure 2.9b) [25; 26].

The main craft will have a wet mass of 1400 kg with the lander accounting for up to 100 kg of this mass. The great mass of the craft means that the acceleration due to SRP is not sufficient and actually has detrimental effects on the attitude control characteristic of the craft [27]. The sail will be made of an aluminised $10 \mu\text{m}$ thick [28] polyimide film. This thickness is due to the unprecedented size of the sail and the need for the substrate to support the solar cells and liquid crystal films. The reflective metallic coating will be kept as thin as possible to reduce the disturbance effects on the spacecraft and the high Isp ion engine will be used for thrust [27]. The SPS will be a square spinning sail with a nominal

spin rate of 0.1 rps and an area of 48.7 m x 48.7 m in size (see Figure 2.9b). The deployment strategy and mechanism remains very similar to that used by IKAROS but with adaptations to accommodate the larger sail and address the lessons learnt from IKAROS [28]. The mass of the sail with four 10 kg tip masses is 203 kg [27].

Table 2.2: Summary of Notable Sail Missions Past, Present and Future. Adapted, updated and extended from Jordaan [29] and Johnson *et al.* [30].

Launch Date	Mission	Mass [kg]	Sail Type	Sail Area [m ²]	Boom Type	a_0^* [$\mu\text{m}/\text{s}^2$]	Stabilisation	Status	Reference
1992	Znamya-2	6000	Disc	314	NA	0.478	Spin	Success	
1999	Znamya-2.5	6000	Disc	490	NA	0.746	Spin	Failed	
2005	Cosmos-1	100	Heliogyro	600	NA	54.816	Spin	Failed	
2008	NanoSail-D	3	Square	10	TRAC	30.453	3-axis passive	Launch failure	[31]
2010	IKAROS	315	Square	200	Wire	5.801	Spin	Success	[17; 16]
2010	NanoSail-D2	3	Square	10	TRAC	30.453	3-axis passive	Success	[32]
2015	LightSail-1	3	Square	32	TRAC	97.451	3-axis	Success	[6; 10]
2015	DeOrbitSail	3	Square	25	CTM	76.133	3-axis	Deployment failure	[33; 34]
2015	Sunjammer	36	Square	1200	Telescopic	304.53	Spin	Cancelled	[35]
2017	InflateSail	3	Square	10	Tape Spring	30.453	3-axis	Success	[36]
2018	Illinois CubeSail	3	Heliogyro	20	Rolled	60.907	3-axis	Awaiting launch	[37; 38]
2018	OrigamiSat-1	4	Square	1	STEM	36.544	3-axis	Awaiting launch	[39; 40]
2019	LightSail-2	3	Square	32	TRAC	97.451	3-axis	Awaiting launch	[6; 41]
2019	NEA Scout	14	Square	86	TRAC	56.121	Spin & 3-axis	In development	[7; 24; 23; 42]
2026	OKEANOS	1400	Square	2325	Wire	15.171	Spin	In development	[25; 26; 28; 27]
TBD	Gossamer-1	30	Square	25	CTM	7.613	3-axis	In development	[43]
TBD	Surrey CubeSail	3	Square	25	SHEARLESS	76.133	3-axis	In development	[44]
TBD	BMSTU-Sail	1.1	Heliogyro	0.4	Rolled	3.322	Spin	In development	[45]

*Characteristic acceleration calculated using $\eta = 1$.

2.5 Related Applications

Solar sails are a small subset of deployable space structures. The size requirements of objects in space vary greatly between missions but there is a growing desire to fit larger structures into smaller satellites which only achieve their final form once in orbit. This can be for several reasons, such as the deployed structure not being stable at 1G or simply a lack of available launch volume. These spacecraft with deploying features need to survive the deployment and obtain stability thereafter. The dynamics of these deployments can have effects on the orbit and attitude of the spacecraft - generally there would either be a significant increase in the inertia of the spacecraft which needs to be absorbed by the ADCS, or spin would need to be maintained in the case of spin stabilised craft. A chaotic change in the attitude of the satellite could also be induced, the rate of this deployment needs to be kept to a manageable magnitude where possible.

2.5.1 Drag Sails

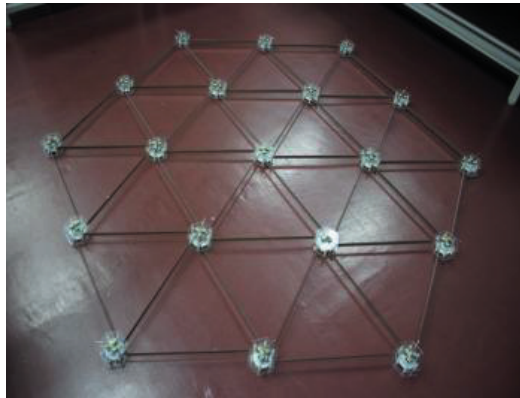
Debris in space and particularly in LEO is fast becoming one of the largest threats to long-term access to space, and as such significant pressure is being placed on satellite designers to ensure that satellites do not add to the problem. For craft in LEO this can be achieved by either pushing into a grave yard orbit or de-orbiting to burn up in the atmosphere. An effective means by which a craft can de-orbit from LEO is to increase the effects of atmospheric drag by increasing the craft's surface area [46]. A drag sail is a common and effective means of achieving this. A small sail is deployed from the craft at the end of its mission life. This sail may be very similar to a solar sail. It would require a deployment mechanism and sail stowage, although the deployment is simplified somewhat as there is no requirement for control of the spacecraft after deployment. This means that deployment does not require significant control and can be excessively chaotic without much regard for the effects on the spacecraft attitude. Deviations from the normal sail design include concepts such as balloons which inflate to increase drag and require no additional support.

Notable de-orbit missions are InflateSail [36] and RemoveDEBRIS [47]. InflateSail was launched in 2016 and consisted of a 10m² deployable sail mounted to a rigid inflatable mast. This satellite was novel in that it was able to test two different forms of deployable structures on a single satellite platform. RemoveDEBRIS was launched in 2017 to the ISS from where it was released into orbit. The objective of the mission is to test several methods of active debris removal in orbit, including net and harpoon capture, drag sails and both camera and LiDAR based navigation and tracking. The RemoveDEBRIS satellite will deploy two small CubeSats to act at targets for the different experiments.

2.5.2 Deployable Trusses

Deployable structures such as trusses which can be used to support additional elements in space can utilise similar technologies in the development of gossamer structures. A concept under development at the Nihon University in Japan uses a mechanism akin to that of a semi-rigid boom solar sail to deploy large multi-node structures, pictured in Figure 2.10a. Each node in the structure consists of biconvex shaped booms wound and stowed on a pulley [48]. The stored energy within the rolled booms is used to drive the deployment of the structure. A similar mechanism derived from this one was developed as a drag sail deployment mechanism [49] as seen in Figure 2.10. Rapidly un-spooling tape booms are at a high risk of undergoing blooming where the layers of wound tape diverge radially within the mechanism. This causes the deployment process to jam or cease as the strain energy within the booms are lost while the booms are still inside the mechanism. Reducing the speed of the boom extension can alleviate this; the mechanism used by Inoue *et al.* [48] and

Tada *et al.* [49] use rotary dampers to apply a torque counter to the pulley rotation achieve this reduction in speed to great success.



(a) Deployable Multi-node Structure [48].



(b) Drag Sail Design [49]

Figure 2.10: Tape Spring Deployable Structures With Rotary Dampers

2.5.3 Synthetic Aperture Radar

Synthetic Appature Radar (SAR) works on the principle that a radar, when mounted on a moving platform, is able to use this translation in space to simulate a larger antenna. This could be a useful application for deploying large orbiting antenna. The size of the satellite used for radar applications has traditionally been determined by the aperture of the antenna require, this is changing as deployable, CubeSat based radar antenna are being developed [50]. Notably the CIRES (CubeSat Imaging Radar for Earth Science) mission aims to equip a constellation of 27 6 U CubeSats with deployable membrane SAR antenna in order to measure geophysical spacial changes of earth [51]. The antenna consists of a 1.53 m^2 membrane which is plated and etched with an antenna array. This membrane is deployed by four STEM booms and the deployment mechanism and membrane fits within a 2 U volume [52]. This is very similar in both function and appearance to a solar or drag sail as can be seen in Figure 2.11.



Figure 2.11: CIRES Membrane Radar Antenna [52]

Notable previous experiments relating to the deployment of antenna in space include the 1996 inflatable antenna experiment [53]. This mission deployed an antenna 14 m in diameter on 28 m booms, both of which were inflatable. This proved to be a success and advanced understanding of how large deployable structures behave in space. Terrestrial tests were not sufficient in producing the information required as there was no suitable artificial environment which could provide both vacuum and microgravity to deploy such a large structure. Scaling laws for such structures were not known, making small scale tests infeasible. During and post deployment the spacecraft experienced significant unexpected behaviour and dynamics, notably an unexpected spin rate upon deployment completion.

2.5.4 Electric Sails

Electric Sails or E-Sails are an alternative to solar sails. They are well-suited for interplanetary missions and operate on the principle of a differing electric field between the "sail" and solar wind (not to be confused with SRP). This makes them another potential means of generating thrust that does not require propellant. An electron gun is required in order to maintain the electrostatic tether charge used to generate the thrust. An E-Sail consists of a number of long charged tethers which are arranged around a central hub on the spacecraft. There can be any number of tethers but systems typically are considered with 20 - 100 tethers which can be several kilometres in length [54]. An electric field is produced by the tethers, which interacts with the protons of the solar wind and generates thrust. In comparison to solar sails, the effective area over which the E-Sail interacts with the solar wind is very large, as each tether effects an area several meters across. As these spacecraft consist of long flexible tethers they are spin stabilised and the tethers can be deployed and kept taut through centrifugal force. This makes their deployment and dynamics extremely similar to a spin stabilised solar sail as the only large key difference in their deployments is the physical presence of a sail membrane. Much of the dynamics and deployment principles which apply to spinning solar sail booms also apply to E-Sail tethers. Fulton and Schaub [54] present some dynamics and deployment strategies for an E-Sail.

2.5.5 James Webb Space Telescope

The James Webb Space Telescope (JWST) is the pending replacement for the Hubble Telescope and is poised to reveal, in far more detail, the origins of the universe, the beginning and end of stars and galaxies and the origins of life. The 6.6 m cryogenic telescope is optimised for the infra-red wave band and has an operating temperature of about 50 K. This is an exceptionally notable craft as a deployable structure. The alignment of the mirrors and instruments are crucial for its operation, and because of its size these mirrors need to be deployed once in orbit so that the satellite can fit inside a rocket fairing. The primary mirror is divided into 18 hexagonal segments in three sections. Two of the sections fold back in order to reduce the total size of the spacecraft for launch, while each segment is fully articulated for calibration and alignment purposes. The secondary mirror is on masts in a forward position which folds back to be stowed. [55; 56; 57]

As the telescope requires very low temperatures to operate, it is crucial that it is properly shielded from solar radiation. A sun-shield has thus been incorporated as a key element of the design. This is made up of five layers of reflective membrane material measuring 12.2 m x 18 m. This material and its deployment is similar to that of a solar sail. This sun shield is expected to nominally operate at appropriately 85 °C on the hot sun facing side and -223 °C on the cold, shaded side where the scientific instruments will be located. The un-integrated sun shield can be seen after a deployment test in Figure 2.12b.

The JWST is currently undergoing testing and integration and is set to launch in 2021 [58].

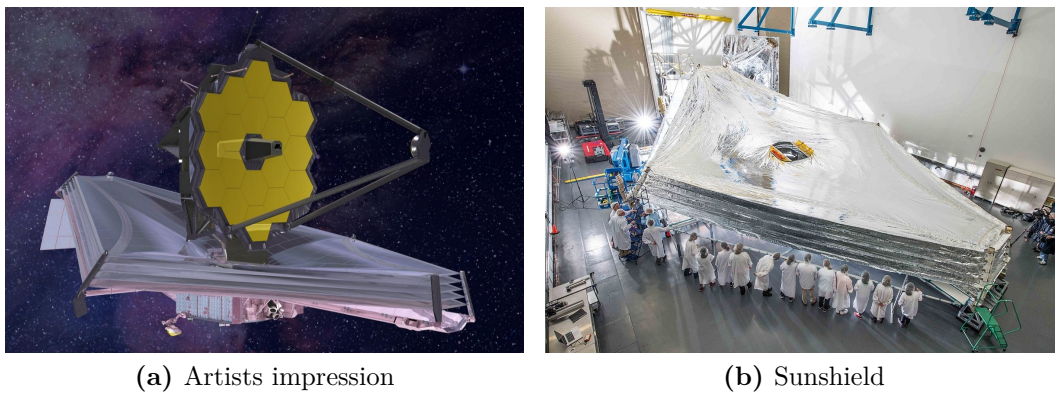


Figure 2.12: James Webb Space Telescope [58]

2.5.6 Breakthrough Starshot

A highly ambitious initiative aims to propel a swarm of hundreds small satellites on an interstellar journey to Proxima-b in the Alpha Centari star system using lasers [59; 60]. The Breakthrough Starshot Initiative proposes that hundreds of small satellites with masses of a few grams each be equipped with 4 m diameter sails [60] - high power lasers in the gigawatt range would then be used to accelerate these craft to a relativistic speed [59]. The craft would, within the space of a few minutes, accelerate to about $0.2c$ and reach the Proxima system for a flyby in approximately 20 years to return data and images. This will be a project of monumental proportions and many technical hurdles need to be overcome before the project can be brought closer to materialisation. The largest of these are developing the laser technology, which needs to be orders of magnitude greater than what is available today, achieving communication with small low power spacecraft 4.25 light years away, and solving several other challenges that are believed to be within the relatively short term grasp [61]. The sail of the spacecraft would also have to be incredibly efficient at harnessing the momentum of photons and would need to be almost perfectly reflective to not vaporise.

The risk of destroying the sail is a concern of any laser-assisted sail design and other proposed missions are also working on the problem [62]. The nature of this method of acceleration is an extremely high load for a very short period of time so any defects or irregularities in the sail would vastly and potentially irrecoverably sabotage the trajectory. For this reason spinning sails with a high spin rate are being considered as this will both provide the centrifugal force to maintain a smooth sail surface and act to mitigate any CoM to CoP offset disturbance torques [59].

While the project is regarded with scepticism for its ambitious nature [60] it is serving its purpose and incentivising research into related topics, such as the development of practical accelerometers that can be used at relativistic speeds [63], and of small single board satellites known as ChipSats [64; 65]. KickSat was a mission attempted in 2014 which aimed to deploy over 100 satellites consisting of a single 35 mm x 35 mm circuit board each [65]. The primary mission objective was to deploy and receive communications from the satellites but this unfortunately failed when the ChipSats could not deploy from the host craft [64].

2.6 Chapter Summary

A brief explanation of the working principle of solar sailing has been presented, along with descriptions of various components and design decisions which have to be made, with partic-

ular focus on the deployment mechanism. Notable solar sailing missions as well as projects which use related technologies and face similar design challenges have been presented and discussed.

The majority of solar sailing missions covered use semi-rigid booms and are three-axis stabilised. The use of semi-rigid deployable structures is a widely applicable and proven method of deploying a gossamer structure in space, and can thus be seen as the option with lower risk. The deployment process is simpler to control and the effects on the spacecraft better understood. It should be noted that a large spacecraft which requires ample sail surface area, or must traverse large distances at practical velocities, requires a large sail and thus long booms. Semi-rigid booms are fundamentally limited by their own properties, placing limits on the sizes of sails which can be constructed using this technology. In order to make use of the full potential of solar thrust large sails are required, where semi-rigid booms are not capable of spanning such large lengths, and stiff beam methods of support are not practical. Spin sails with flexible booms are thus the suitable choice when developing a large solar sail, as the centrifugal force generated acts to maintain the deployed state of the sail. Little practical development has been done on this technology. The deployment mechanisms and methods which can be used with spinning sailcraft are potentially also significantly simpler than the complex mechanisms required to deploy semi-rigid booms.

The dominant drawbacks of using a spin sail design are that the spacecraft requires the ability to manage the immense increase in the moment of inertia, as well as the ability to utilise observation payloads, for which a spinning platform is not suitable. A means of mitigating this is to use dual-spin spacecraft which may offer some of the benefits of both stabilised and spinning craft. The use of a dual- or tri-spin spacecraft does add additional complication, as there may be the need for signals to traverse a rotating joint. A means to avoid this complication would be to have a deployment process which could proceed without any direct external intervention and thus deploy passively. This would be of benefit to spacecraft with and without multiple spinning sections. Minimal inputs to the deployment process can reduce the process complexity and requirements on the system and power requirements.

Investigations into spinning solar sail deployment with flexible booms has the potential for wide applications. The findings may be applied to other, similar, topics such as deployable antenna, drag sails, scientific instruments as well as the deployment of tethers for E-sail applications.

Chapter 3

Modelling

The theoretical dynamics of a deploying spinning solar sail are to be investigated. This chapter provides a description of a solar sailing satellite conceptual model. The equations of motion of this model will be derived using Lagrangian mechanics, and a simplified motion model of the systems primary components is presented and built upon to arrive at a suitable representative model. Additional considerations which affect the deployment will be discussed and incorporated into the simulation regime. A number of deployment cases will be investigated. Finally consideration will be given to aspects of practical deployment which need consideration and may cause variations from nominal theoretical behaviour.

3.1 Conceptual Sail Model

To obtain a dynamic model of the sail deployment, the system needs to be defined. As only the deployment dynamics of the solar sail are of interest here the system to be investigated can be greatly simplified from that of an entire satellite. Aspects such as the exact make up of the ADCS, expected orbits and payloads can be ignored. The following key aspects of the system are defined such that a model can be derived.

3.1.1 Satellite Form

A fair degree of the dynamics will depend on the size and mass of the satellite body. A larger satellite would allow for a larger solar sail, however the focus will be a 3U CubeSat similar to that of the LightSail spacecraft. The sail is specified as a spin stabilised sail as this lends scalability to the design and provides further insight into this less frequently used means of deploying a sail. This presents several options on how the craft as a whole may be configured. The simplest approach is where the entire spacecraft and sail rotate as one. Other options include dual-spin craft, where the sail rotates relative to the satellite body, and the novel tri-spin method proposed by Jordaan [29], which allows a spinning sail structure relative to the satellite body and a momentum counter system with an opposed spin to that of the sail to maintain a low net angular momentum. These three configurations are illustrated in Figure 3.1. Trends in the deployment behaviour of all three cases will present similar results. The key difference between the configurations is how the deployment mechanism rotation rate is maintained, whether it spins with the satellite or not. Where the entire spacecraft spins some kind of momentum exchange device is required to ensure spin is maintained after deployment, or built up beforehand, and that a high enough spin rate is achievable to commence deployment - this could be large reaction wheels or thrusters. In the tri-spin, or a dual-spin, scenario there would need to be a motor driving the spin of the deployment mechanism relative to the spacecraft bus. Whichever configuration is used the actuator involved must be able to maintain the spin of the sail structure post-deployment as well as

accelerate spin to the rate required at deployment initiation. The use of the tri- or dual-spin configurations adds significant mechanical and electrical complication, as there either needs to be control and sensing abilities through a rotating joint, or the deployment needs to be purely passive. In the case of passive deployment, no feedback can be obtained from the rotating deployment mechanism besides that which can be extracted from the driving motor behaviour.

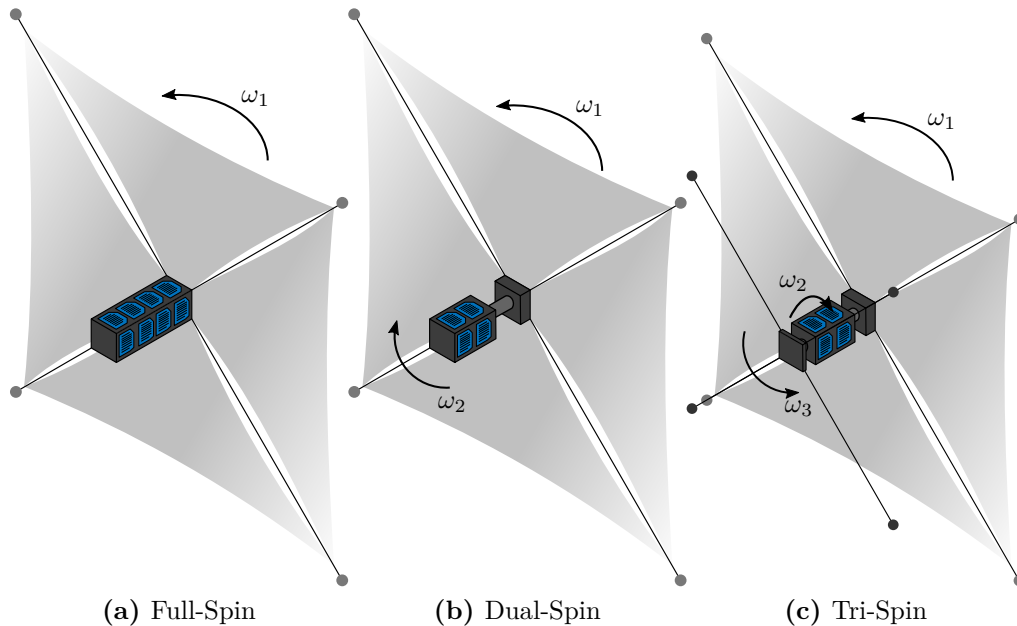


Figure 3.1: Spin Stabilised Sailcraft Configurations

For the purposes of this thesis the case of a fully-spin stabilised craft is used. This allows for some simplicity in the analysis as well as presenting a more practically achievable solution. When deployment is discussed the terms body and bus are used interchangeably to refer to the portion of the satellite housing and driving the deployment mechanism. Although a fully-spinning craft is investigated, the modelling, design and discussion will be tailored to apply to a passive deployment where possible. This allows the deployment mechanisms and dynamics developed to be applied to any spin configuration without the complication of sensing and control over rotating joints. The use of passive deployment offers advantages to any spin configuration of craft as it has the potential to reduce the complexity of the problem, the input power required, as well as the reliability of the deployment process as there are fewer failure points inherent in the design.

The deployment of the sail from the craft is of primary concern. For this reason the majority of the model will be simplified to a two dimensional problem focusing on the sail plane and the dynamics therein. Out-of-plane dynamics would be present but these are negligible when compared to those which occur in plane [66]. The out of plane dynamics are of more interest when attitude changes are present with a deployed or partially deployed sail as investigated by Jordaan [29].

3.1.2 Sail

LightSail had 1.5U assigned to stowage of its 32 m² sail and 0.5U to the deployment mechanism [10]. NanoSail-D had 2U assigned to both the deployment mechanism and 10 m² sail storage [31]. NEA Scout will fit a 86 m² sail in a 2U volume [24]. Based on these figures a sail packing density of roughly 20 m²/U to 40 m²/U can be assumed. The amount of sail material which can be stowed in a given volume is highly dependent on the means of stowage, folding methodology and means of retention used as well as any structural elements necessary. But this does suggest that an almost 50 m² sail could be fit in the form factor of a 3U CubeSat provided the deployment mechanism can be made small enough. A square sail of this size would require each boom to be 5 m long. In order to maintain parameters more compatible to past missions using a 3U CubeSat platform, a 30 m² sail with 4 m booms will be investigated.

Depending on the deployment strategy used the sail can be made to have a minimal effect on deployment. As there is no air resistance or gravity, the effects of the sail on the boom deployment is low, assuming that the sail is not tightly constrained when stowed. IKAROS had a sail 7.5 µm thick with a substrate constructed of two polyimide material resins [16]. While thin it was relatively thick compared to other sails as it needed to support the flexible solar cell and liquid crystal films. The sail, with the mentioned additions, had a mass of 13 kg or 65 g/m². The average mass of the un-aluminised sail without additions was 9.245 g/m². LightSail had a 4.6 µm thick Mylar Sail [20] while NanoSail-D had a 2 µm thick polyimide sail with a 1000 Å aluminium coating [31]. Based on the information for IKAROS and NanoSail-D an areal mass density of $\rho_a = 2.465 \text{ g/m}^2$ will be used.

The effect the sail has on deployment, as mentioned, depends upon the deployment strategy used. In the case of IKAROS deployment was conducted in a manner very similar to a yo-yo de-spin. The sail was connected at the boom tip and unrolled along with the boom. The sail would have added to the effective mass of the boom as well as increased the damping of any boom offsets relative to the satellite body. If the booms was stowed in a manner more akin to that of LightSail, then the boom too would experience an effective increase in damping and mass as well as a force counter-acting the deployment as the sail is pulled out of its stowage. This countering force can be roughly seen as a friction force as the sail was held in place by friction between folds of the sail. Were the sail on a spool, as with NEA Scout, the situation would be similar as the force pulling on the sail would need to overcome the internal friction of the spool.

The sail membrane mass can be simplified and combined with the boom tip masses. Accurately including the sail and its effects on the boom dynamics would involve an extensive finite element analysis. For the purposes of simplification the inertia of the sail around the body rotation axis can be equated to a point mass at the boom ends and combined with the tip mass. Determining the exact inertia of the sail at any time during deployment would be extremely complex as the shape and mass distribution of the deployed sail section at that point in time would need to be known. The sail inertia at its fully deployed state can easily be found as

$$I_s = \frac{1}{6}m_s A_s = \frac{1}{3}m_s \ell_f^2, \quad (3.1.1)$$

where m_s is the mass of the sail membrane and ℓ_f if the final length of the deployed boom. From this, assuming four booms, the equivalent sail mass, m_{se} , which would need to be added to each boom tip is

$$m_{se} = \frac{1}{12}m_s = \frac{1}{12}\rho_a A = \frac{1}{6}\rho_a \ell_f^2. \quad (3.1.2)$$

For a 30 m² sail this additional mass would equate to 6.16 g per boom tip. This is a crude assumption and over-estimates a solution, as in practice no equivalent mass m_{se} is contributed by the sail at the initiation of deployment, the mass contribution of the sail increases

with the amount of sail membrane pulled from the stowed position, and the simplification only fully applies upon completion of deployment. To better illustrate this Figure 3.2 is provided which is a visualisation produced from the simulation of the deployment process of the IKAROS solar sail. The knock-on effects of this assumption include the deployment rate, as the centrifugal force will be increased, and oscillations of the boom during and post deployment. This simplification is similar to that as was used by Jordaan [29].

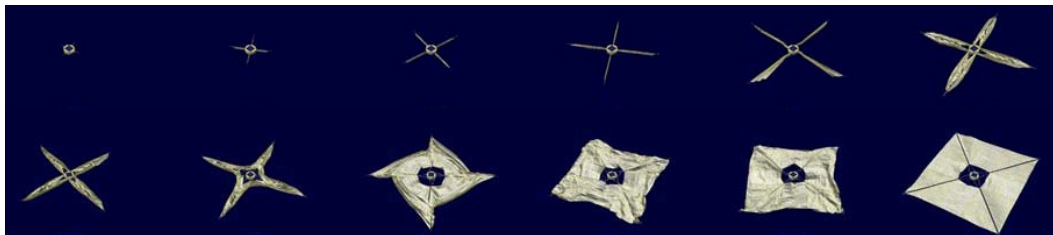


Figure 3.2: Illustration of the Changing Sail Shape During Deployment. Adapted from [16].

3.1.3 Booms

The use of a spin stabilised sailcraft negates the need for semi-rigid booms and flexible members may be used in place thereof. These members may take the form of cable, wire, cord or string depending on the forces involved in the deployment. Here the flexible boom members will be referred to as the booms or boom wires. The booms are attached to masses at the outer most points. The centrifugal force acting on these masses is the primary force driving and maintaining the deployment of the sail structure. The booms are wound around a pulley where they are stowed prior to deployment and exit the satellite body at the corners through followers.

The booms will have distinct properties depending on the size and choice of material used in practice. Here the boom wires will be assumed to be incompressible, massless and rigid elements. The wire is assumed to have damping properties and no spring characteristics. Almost any material used will, in practice, display some sort of damping characteristics, while not all will possess meaningful spring properties. There are limited sailcraft using wire booms for reference purposes. The DICE spacecraft deployed two instrument probes on wire booms, and these booms were found to have a wire damping coefficient of $b = 0.33647 \text{ mN} \cdot \text{m} \cdot \text{s}/\text{rad}$ [67]. This value is used as it is known to be representative of values which can be expected in practice from a thin wire. The damping of the boom offset angle will be compounded by the sail's presence. Ignoring this increase in damping, while a simplification, will present the worst case scenarios in terms of boom deflection angles.

3.1.4 Controlling Deployment

For booms of meaningful length at practical spin rates, free deployment is not possible - this is addressed in the following section. Some method of slowing the process needs to be implemented. IKAROS used the approach of a staged deployment where sections of the booms were released at appropriate spin rates in a manner similar to a yo-yo de-spin. This allows negative dynamic effects to be mitigated and allowed to settle between stages where spin rate can also be recovered. Practical information on the deployment of spinning solar sails with flexible wire booms is limited but there is a fair amount available on the deployment of wire mounted scientific instruments Morbhat [67]; Lai *et al.* [66]; Auslander

et al. [68] which presents similar dynamics. These cases, for the most part, apply some form of artificially induced deployment rate for the increasing boom length, such as a constant or stepped deployment rate, and thus do not fully derive equations of motion which include the full deployment dynamics. As forms of free and damped deployment are to be investigated these are necessary.

In order to slow the rate of deployment a damped pulley, around which the boom wire is spooled, will be considered. This pulley will have a rotational damping coefficient b_p . This provides a passive means of controlling the deployment rate in a reliable and predictable fashion, where the rate of deployment can be controlled via b_p and the rate at which the deployment commences determined by the static friction in the pulley's rotation.

Table 3.1: Centrifugal Force Maintained by Select Missions

Mission	Tip Mass [g]	Nominal Rate [rpm]	ℓ_f [m]	F_c [mN]	Reference
IKAROS	500	1	10	54.83	[16]
DICE	8.35	6	5	16.48	[69]

A minimum centrifugal force would need to be maintained on the booms at all times to ensure that no tangling or unwanted deformation of the booms or sail occurs. The centrifugal force maintained by missions with deployable wire booms are given in Table 3.1. IKAROS is the only solar sailing mission mentioned. The centrifugal force maintained by IKAROS is significantly greater than that of scientific instrumentation as higher tension is desired to maintain the shape of the sail and reduce billowing effects. The force maintained by IKAROS will be used as a minimum allowable force. This places lower bounds on the combinations of spin rate and tip mass. If 20 g tip masses are used, the minimum spin rate in the deployed state is 7.84 rpm.

3.2 Kinematic Problem

In order to model this highly coupled and non-linear system a more elegant approach than Newtonian mechanics is sought. While it is perfectly possible to model the dynamics of this system using a Newton-Euler approach, this would result in a highly complex derivation process and solution, as the system is highly non-linear, chaotic and involves multiple reference frames. Instead the problem is approached using Lagrangian mechanics, an energy-based approach well-suited to solving problems such as this.

3.2.1 System Layout

A deploying spinning solar sail is modelled in the two dimensional sail plane as a central bus or body with a rotation rate about its central axis, P , of $\dot{\beta}$. The satellite body as a mass m_b and a moment of inertia I_b . From this rotating body four equally-spaced booms of length ℓ_i are deployed. The booms exit the satellite body a distance r from the axis of rotation. The offset angle of these booms relative to their nominal position is θ_i . The oscillations in θ_i are subject to a damping of b_i . Each boom has a tip mass of m_i . The entire system is located in free space at position $\mathbf{P} = [P_x \ P_y]^T$. The system described is illustrated in Figure 3.3. The time dependant variables are P_x , P_y , β , θ_i and ℓ_i .

As mentioned the booms will be modelled as rigid members with no mass or physical properties themselves. This assumption greatly reduces the complexity and coupling in the derived equations. The subscript i is used to identify individual booms. In cases where only one

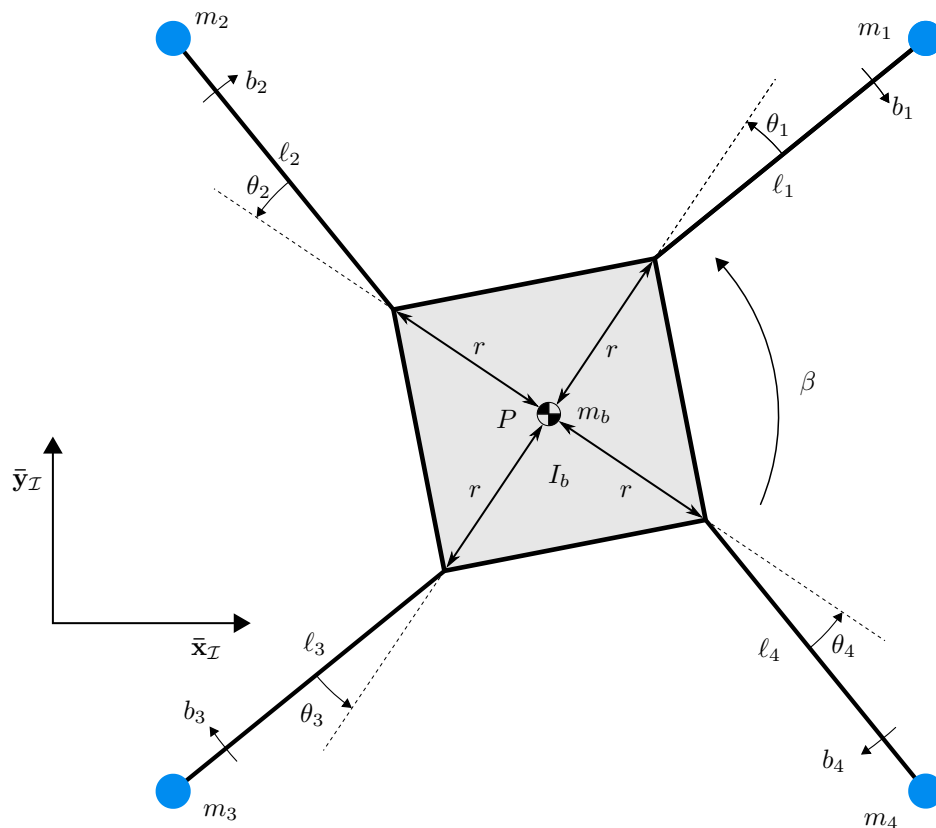


Figure 3.3: Bus and Four Booms

boom is considered the subscript may be omitted completely for clarity. The boom damping b may also be considered equal for all booms, unless individually stated; $b = b_i$.

3.3 Lagrangian Mechanics

Lagrangian mechanics is an energy based method and allows the description of dynamic motion to be found in a systematic manner. It is well-suited to complex systems with conservative forces. The method is energy-based and allows the selection of generalised coordinates based on preference and convenience. As the case under investigation involves multiple possible configurations, depending on the area of interest and rotating reference frames, using Lagrangian mechanics proves to be more suitable.

The derivation of a solution set of equations which describes a system's motion can be found using Lagrangian mechanics in a procedural manner. Initially all the degrees of freedom in the system are determined in the form of a variable vector,

$$\mathbf{p} = \begin{bmatrix} p_1 \\ p_2 \\ \vdots \\ p_n \end{bmatrix}, \quad (3.3.1)$$

which contains all the time dependant variables of interest in the system.

As the method is energy-based, the energies of all the system elements need to be calculated.

The total kinetic energy, which is the sum of all translating and rotating masses, is

$$T = \frac{1}{2} \sum_{i=1}^N m_i \|\mathbf{v}_i\|^2 + \frac{1}{2} \sum_{i=1}^N I_i \|\boldsymbol{\omega}_i\|^2 \quad (3.3.2)$$

where $\boldsymbol{\omega}_i$ is the angular rate of the element under consideration and \mathbf{v}_i is the velocity of the i^{th} object of N total objects. The total potential energy is V . In consideration of the deployable flexible booms there is assumed to be no means of storing potential energy due to the absence of gravity or springs in the system.

The Lagrange function or Lagrangian is the difference in the total kinetic energy and the total potential energy,

$$\mathcal{L} = T - V. \quad (3.3.3)$$

The Lagrangian accounts for all conservative forces in the system. In order to include non-conservative forces, such as damping, Rayleigh's dissipation function [70] is used. This accounts for forces which are dependent on particle velocity such as friction or damping. It is presented here in a form suitable for rotational motion:

$$R = -\frac{1}{2} \sum_{i=1}^N K_i \boldsymbol{\omega}_i^2, \quad (3.3.4)$$

the leading negative indicating that the energy is dissipated in a non-conservative manner, and K_i representing the coefficient driving the dissipation such as b_i in the case of damping.

The Euler-Lagrange equation is applied with the dissipation function and Lagrangian for each component of the variable vector,

$$\frac{d}{dt} \left(\frac{\partial \mathcal{L}}{\partial \dot{p}_k} \right) - \frac{\partial \mathcal{L}}{\partial p_k} = Q_k. \quad (3.3.5)$$

Here p_k refers to the individual independent components of the variable vector necessary to describe its motion at any point in time. The right hand side, Q_k , represents the resultant loading of, or energy lost to, the system. As the system is isolated and the only means by which energy can be lost is through the wire damping. The dissipation function, R , representing the resultant energy loss can be written as

$$Q_i = \frac{\partial R}{\partial \dot{p}_k}. \quad (3.3.6)$$

The Euler-Lagrange is solved for each component of the variable vector yielding a set of highly coupled equations of motion which describe the dynamics of the system. These equations are de-coupled as needed in order to obtain a final set of independent equations. A simplified case building towards the full dynamic model is derived using Lagrangian mechanics in the next section to illustrate the use and effectiveness of this method.

3.4 Double Pendulum Model

A single isolated boom in its deployed state can be seen as a double pendulum model. The distance from the centre of bus rotation to the boom exit point is representative of the first link and the boom itself as the second link. The mass and inertia of the satellite bus can be modelled as a mass at the end of the first link and the boom tip mass remains as it is at the end of the double pendulum. Both links of the pendulum are considered perfectly rigid and massless.

This model represents a simplified single boom. To expand this to a full sail model four of these double pendulums are arranged equally-spaced around the bus centre with a relative angle of 90° .

As mentioned, the classic double pendulum model is the basis on which the dynamics of a deploying wire boom satellite configuration will be constructed. To show the working method, the derivation of a damped double pendulum will be presented. The system as it is considered here is illustrated in Figure 3.4. In this representation, the angles are as presented earlier for the system layout, but applied to a double pendulum model where β and θ are the angles of the first link relative to the observers reference frame and the second link relative to the first respectively. The damping, b , affects the boom or second link angular rate of change. The two masses in the system are the tip mass, m , and the mass which represents the mass and inertia of the satellite body or deployment mechanism m_b . The derivation is presented in such a way that it is representative of the entire multiple boom system but applied to a simple double pendulum case which is analogous to a single boom of fixed length.

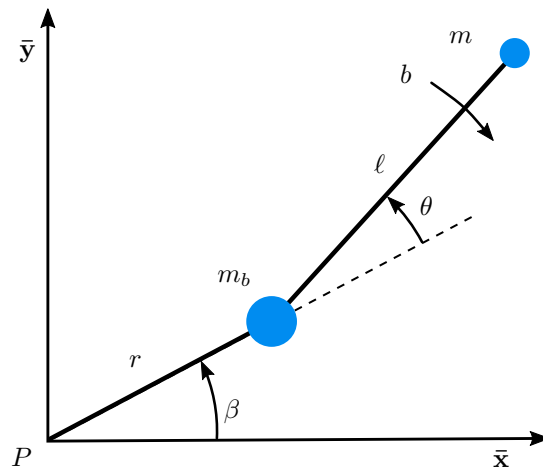


Figure 3.4: Rotating Double Pendulum

Following the process of deriving the equations of motion using Lagrangian mechanics the first step is to define a parameter vector containing the time dependent variables in the system. In this case, of a rotating double pendulum problem, the non-deploying scenario is considered, making the variable vector

$$\mathbf{p} = \begin{bmatrix} p_1 \\ p_2 \\ \vdots \\ p_n \end{bmatrix} = \begin{bmatrix} \beta \\ \theta \end{bmatrix}. \quad (3.4.1)$$

The position vectors of the elements in the system can now be defined. The centre of rotation of the satellite is about point P which is located in inertial space. In the simple double pendulum case we assume this as a fixed point of

$$\mathbf{P} = \begin{bmatrix} x \\ y \end{bmatrix} = \begin{bmatrix} P_x \\ P_y \end{bmatrix} = \begin{bmatrix} 0 \\ 0 \end{bmatrix}. \quad (3.4.2)$$

The first link of the double pendulum with the end mass m_b is rotating about this point with a time dependent angle of β .

The bus corner or boom exit point position at m_b is given by,

$$\mathbf{r}_{m_{b_i}} = \begin{bmatrix} x \\ y \end{bmatrix} = \begin{bmatrix} r \cos(\beta + \frac{2\pi}{n}(i-1)) \\ r \sin(\beta + \frac{2\pi}{n}(i-1)) \end{bmatrix}, \quad (3.4.3)$$

where n is the total number of booms in the system and i indicates the particular boom under consideration where $1 \leq i \leq n$.

The position of the tip mass is similarly found by

$$\mathbf{r}_{m_i} = \begin{bmatrix} x \\ y \end{bmatrix} = \begin{bmatrix} r \cos(\beta + \frac{2\pi}{n}(i-1)) + \ell_i \cos(\beta + \theta_i + \frac{2\pi}{n}(i-1)) \\ r \sin(\beta + \frac{2\pi}{n}(i-1)) + \ell_i \sin(\beta + \theta_i + \frac{2\pi}{n}(i-1)) \end{bmatrix}. \quad (3.4.4)$$

The element positions for the single pendulum case are easily seen in the above equations as both n and i are 1.

The time derivative of these elements yields their velocity vectors from which their scalar magnitude can be easily determined. For the first mass in this particular case,

$$\mathbf{v}_{m_b} = \dot{\mathbf{r}}_{m_b} = \begin{bmatrix} -\dot{\beta}r \sin \beta \\ \dot{\beta}r \cos \beta \end{bmatrix} \quad (3.4.5)$$

and

$$\begin{aligned} \|\mathbf{v}_{m_b}\| &= \sqrt{(-\dot{\beta}r \sin \beta)^2 + (\dot{\beta}r \cos \beta)^2} \\ &= \dot{\beta}r. \end{aligned} \quad (3.4.6)$$

For the boom tip mass:

$$\mathbf{v}_m = \dot{\mathbf{r}}_m = \begin{bmatrix} -\dot{\beta}r \sin \beta - (\dot{\beta} + \dot{\theta})\ell \sin(\beta + \theta) \\ \dot{\beta}r \cos \beta + (\dot{\beta} + \dot{\theta})\ell \cos(\beta + \theta) \end{bmatrix}, \quad (3.4.7)$$

and

$$\begin{aligned} \|\mathbf{v}_m\| &= \sqrt{(-\dot{\beta}r \sin \beta - (\dot{\beta} + \dot{\theta})\ell \sin(\beta + \theta))^2 + (\dot{\beta}r \cos \beta + (\dot{\beta} + \dot{\theta})\ell \cos(\beta + \theta))^2} \\ &= \sqrt{\dot{\beta}^2 \ell^2 + \dot{\beta}^2 r^2 + \ell^2 \dot{\theta}^2 + 2\dot{\beta} \ell^2 \dot{\theta} + 2\dot{\beta}^2 \ell r \cos(\theta) + 2\dot{\beta} \ell r \dot{\theta} \cos(\theta)}. \end{aligned} \quad (3.4.8)$$

The total energy in the system can now be computed as the sum of the energies of all the moving elements with mass as per Equation 3.3.2,

$$\begin{aligned} T &= T_P + T_{m_b} + T_m \\ &= \frac{1}{2} m_b \|\dot{\mathbf{P}}\|^2 + \frac{1}{2} I_b \|\dot{\beta}\|^2 + \frac{1}{2} m \|\mathbf{v}_m\|^2 \\ &= 0 + \frac{1}{2} (\dot{\beta}^2 \ell^2 m + \dot{\beta}^2 m r^2 + \dot{\beta}^2 m_b r^2 + \ell^2 m \dot{\theta}^2) + \dot{\beta} \ell^2 m \dot{\theta} + \dot{\beta}^2 \ell m r \cos(\theta) + \dot{\beta} \ell m r \dot{\theta} \cos(\theta), \end{aligned} \quad (3.4.9)$$

where the bus or first link inertia is taken as $I_b = m_b r^2$. There are no sources for potential energy in the system such as gravity or springs and thus $V = 0$. The Lagrangian is therefore simply $\mathcal{L} = T$.

The work done in the system by damping in the boom, b , is represented by the Rayleigh dissipation function as

$$R = -\frac{1}{2} \sum_i^n b_i \dot{\theta}_i^2 = -\frac{1}{2} b \dot{\theta}^2. \quad (3.4.10)$$

Now we apply Equation 3.3.5 for each element in the variable vector in order to determine the equations of motion which describe this system. The individual terms of the Euler-Lagrange equation are now solved for each element of the variable vector:

$$p_1 = \beta \begin{cases} \frac{\partial \mathcal{L}}{\partial \beta} = \dot{\beta} m r^2 + \ell^2 m \dot{\theta} + m_b \dot{\beta} r^2 + \dot{\beta} \ell^2 m + 2 \dot{\beta} \ell m r \cos(\theta) + \ell m r \dot{\theta} \cos(\theta) \\ \frac{d}{dt} \left(\frac{\partial \mathcal{L}}{\partial \dot{\beta}} \right) = \ddot{\theta} (\ell^2 m + \ell m r \cos(\theta)) - \dot{\theta} (\ell m r \dot{\theta} \sin(\theta) + 2 \dot{\beta} \ell m r \sin(\theta)) + \\ \ddot{\beta} (m_b r^2 + \ell^2 m + m r^2 + 2 \ell m r \cos(\theta)) \\ \frac{\partial \mathcal{L}}{\partial \dot{\beta}} = 0 \\ \frac{\partial R}{\partial \dot{\beta}} = 0 \end{cases} \quad (3.4.11)$$

$$p_2 = \theta \begin{cases} \frac{\partial \mathcal{L}}{\partial \theta} = \ell^2 m \dot{\theta} + \dot{\beta} \ell^2 m + \dot{\beta} \ell m r \cos(\theta) \\ \frac{d}{dt} \left(\frac{\partial \mathcal{L}}{\partial \dot{\theta}} \right) = \ddot{\beta} (\ell^2 m + \ell m r \cos(\theta)) + \ell^2 m \ddot{\theta} - \dot{\beta} \ell m r \dot{\theta} \sin(\theta) \\ \frac{\partial \mathcal{L}}{\partial \dot{\theta}} = -\dot{\beta}^2 \ell m r \sin(\theta) - \dot{\beta} \ell m r \dot{\theta} \sin(\theta) \\ \frac{\partial R}{\partial \dot{\theta}} = -b \dot{\theta} \end{cases} \quad (3.4.12)$$

Substituting these derivations into the Euler-Lagrange equation yields two second order equations which describe the system's dynamics,

$$\ddot{\beta} (m_b r^2 + \ell^2 m + m r^2 + 2 \ell m r \cos(\theta)) + \ell m \ddot{\theta} (\ell + r \cos(\theta)) - \ell m r \dot{\theta} \sin(\theta) (2 \dot{\beta} + \dot{\theta}) = 0 \quad (3.4.13)$$

and

$$\ddot{\beta} (\ell^2 m + \ell m r \cos(\theta)) + \ell^2 m \ddot{\theta} + \dot{\beta}^2 \ell m r \sin(\theta) = -b \dot{\theta}. \quad (3.4.14)$$

These equations are coupled to each other. The larger the variable vector becomes the more coupled and complex these equations become. Uncoupling these equations from one another yields the solution for the angular acceleration of the satellite body link as

$$\ddot{\beta} = \frac{b \ell \dot{\theta} + b r \dot{\theta} \cos(\theta) + \dot{\beta}^2 \ell^2 m r \sin(\theta) + \ell^2 m r \dot{\theta}^2 \sin(\theta) + \dot{\beta}^2 \ell m r^2 \cos(\theta) \sin(\theta) + 2 \dot{\beta} \ell^2 m r \dot{\theta} \sin(\theta)}{\ell r^2 (m_b + m - m \cos(\theta)^2)} \quad (3.4.15)$$

and that of the second link or boom as

$$\ddot{\theta} = \frac{-2(m_b b r^2 \dot{\theta} + b \ell^2 m \dot{\theta} + b m r^2 \dot{\theta} + \dot{\beta}^2 \ell m^2 r^3 \sin(\theta) + \dot{\beta}^2 \ell^3 m^2 r \sin(\theta) + \ell^3 m^2 r \dot{\theta}^2 \sin(\theta) + \dot{\beta}^2 \ell^2 m^2 r^2 \sin(2\theta) + \frac{1}{2} (\ell^2 m^2 r^2 \dot{\theta}^2 \sin(2\theta)) + m_b \dot{\beta}^2 \ell m r^3 \sin(\theta) + 2 \dot{\beta} \ell^3 m^2 r \dot{\theta} \sin(\theta) + 2 b \ell m r \dot{\theta} \cos(\theta) + \dot{\beta} \ell^2 m^2 r^2 \dot{\theta} \sin(2\theta))}{\ell^2 m r^2 (2 m_b + m - m \cos(2\theta))} \quad (3.4.16)$$

which presents them in a state suitable for simulation and investigation through the use of numerical integration. These equations match those as are widely available in literature whether derived using Lagrangian, Newtonian or other methods and are similar to those of the classical double pendulum barring the negation of gravity effects.

This simplified case of a simple non-deploying damped double pendulum provides good initial insight into the dynamics that can be expected. Applying the equations of motion presented in Equations 3.4.15 and 3.4.16 with the constants $b = 6.7294 \text{ mN} \cdot \text{m} \cdot \text{s}/\text{rad}$, $r = 0.1 \text{ m}$, $m_b = 1 \text{ kg}$, $m = 0.5 \text{ kg}$ and $\ell = 0.5 \text{ m}$ and initial conditions $\dot{\beta}_0 = 0.5 \text{ rps}$ and $\theta_0 = -10^\circ$ yields the responses seen in Figure 3.5. Although this is not a practical configuration it is used here to convey the trends in the dynamics.

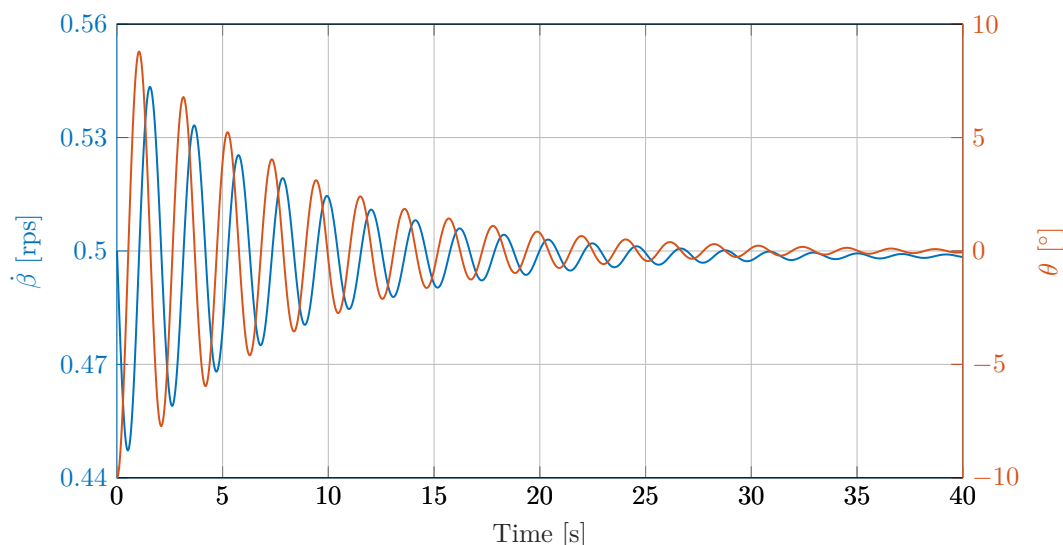


Figure 3.5: Response of Simple Damped Double Pendulum Model

This case considers the first pendulum link, analogous to the bus, to have a initial spin rate and a lagging second link, analogous to the boom, with no instantaneous velocity relative to the bus. The first effect of this is that the bus rate is quickly retarded as the energy is transferred to accelerating the boom to catch up with the bus. The boom then, having gained a positive non-zero angular velocity $\dot{\theta}$ overshoots its zero position and begins to lose speed as it is restrained by the bus. The bus rate is in turn increased in response as the boom "pulls" it forward until it again overtakes the boom. This cyclic oscillation between the bus and the boom continues until it is dissipated by the internal damping of the boom wire. The final angular rate of the bus is marginally lower than the initial rate in this closed system as the energy was expended in recovering the θ angle and in the boom damping. Had the initial condition been that the boom was leading the bus the situation would be reversed and the final steady state bus rate would be higher. The value for the damping used here is greatly exaggerated for explanatory purposes and the time scale required to fully damp out this oscillation can be significantly large. This provides insight into why understanding the dynamics of flexible boom solar sails during- and post-deployment is important. The consequences of a chaotic deployment can have extended effects on the operation of the spacecraft and particularly for the design of its ADCS systems.

The process of deriving these equations for larger systems grows rapidly in complexity with the size of the variable vector. The use of a software package which supports symbolic computation, such as Matlab's symbolic toolbox or the Python library Sympy, allows the derivation of these equations with precision and speed. A script was written to derive the equations of motion of the spinning solar sail model based on an input of the number of booms, reference frame and whether the booms are deploying or not. The script derived these equations, formatted them in such a way that they could be used in simulation and

wrote them as executable functions files. The pseudocode algorithm used for this process can be seen in Appendix A. The final decoupled equations of motion derived by this method, which were used to investigate the cases to follow, can be found in Appendix B.

3.5 Extended Model Deployment

For the case of a deploying solar sail model there are some other factors to consider. To gain an understanding of the in-plane boom behaviour when undergoing deployment, a single boom is modelled. Multiple booms will be incorporated into the simulation in Section 3.8 when some of the practical effects on a deployment will be investigated. In addition to the expansion of the variable vector to include ℓ as a component, the means by which the boom will be prevented from free and uncontrolled deployment need to be considered as well as the effects of winding large lengths of boom wire on a circular pulley hub.

3.5.1 Deploying Double Pendulum Model

The case of the double pendulum previously presented neglects the deploying aspect of the boom. In order to account for this the variable vector is expanded to

$$\mathbf{p} = \begin{bmatrix} \beta \\ \theta \\ \ell \end{bmatrix} \quad (3.5.1)$$

as ℓ becomes a time-varying component. The remainder of the derivation process follows that as was previously conducted, but with the effects of the now included time derivatives of ℓ as $\dot{\ell}$ and $\ddot{\ell}$ representing the velocity and acceleration, respectively, of the boom in line with the boom wire. The equations derived and used to conduct the following simulated cases can be found in Appendix B.1.3.

When free deployment is investigated all the equations need to be decoupled from one another to obtain the true natural dynamics of the system. However, when deployment is restrained or controlled in some fashion and not allowed to proceed naturally, such as by the use of a rotational damper, $\ddot{\ell}$ cannot be decoupled from the other dynamic equation as information is lost in the process of decoupling, simplifying and consequently driving $\ddot{\ell}$ by external means. This is clearly seen in the simplicity of the fully decoupled equations (Appendix B.1.2) as opposed to those where $\ddot{\ell}$ has been left coupled (Appendix B.1.3).

3.5.2 Free Deployment

The deployment of the booms is driven by centrifugal force. Unconstrained this will lead to a rapid increase in ℓ , opening cases to several possible modes of failure. The satellite moment of inertia rapidly increases with the unchecked increase of the boom length. This causes the bus spin rate to drop in a drastic fashion. The boom tip mass has its own inertia which causes it to lag behind the bus, leading to the growth of the in-plane boom offset angle. This large value in θ is indicative of boom wrapping, where the boom can coil around the satellite body either during or upon completion of deployment. If deployment reaches its end the θ angle will need to recover causing chaotic behaviour of the bus and sail. During this ordeal the ADCS could saturate, boom wrapping could occur or the sail could be torn or unevenly deployed. Oscillations of such magnitude could take significant time to dampen out, having negative effects on the dynamics of the satellite and effectiveness of the sail itself for a time lasting far longer than was taken for the deployment of the sail itself.

To demonstrate this effect a simulated case of the deployment with a 20 g tip mass is allowed to deploy without restraint from a 3U CubeSat. The results for several initial bus rates can be seen in Figure 3.6 where the trends discussed can be seen. These are the trends as

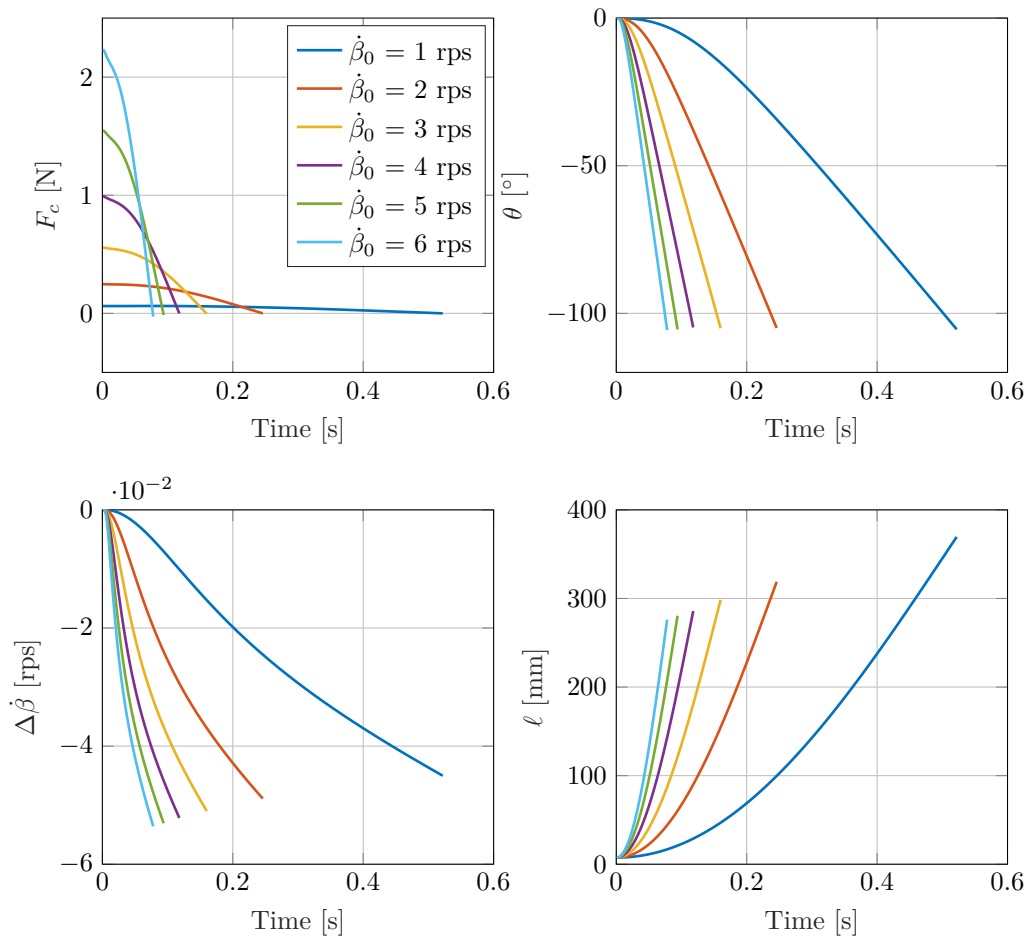


Figure 3.6: Effects of Free Deployment

described by the equations of motion in Appendix B.1.2. Stopping criteria for the simulated cases is the loss of tension in the booms at $F_c = 0$. In practice there would be a positive minimum allowable boom tension. This method of deployment would only work if such chaotic behaviour could be tolerated and the booms were impractically small, although recovering a steady spin rate would prove challenging after the oscillations caused by the recovery of the large θ angle. Note that in the case where $\dot{\beta}_0 = 1$ rps the boom angle θ reaches -100° in about 0.5s at which point almost 0.4m of boom has been extended. Recovery from this kind of behaviour is almost unimaginable.

3.5.3 Damped Pulley

It has readily been shown in the preceding section that unconstrained centrifugal deployment of a solar sail with flexible wire booms is not practically possible. The booms deploy rapidly and wrap themselves around the spacecraft bus. This is very similar to the yo-yo de-spin method of reducing a craft's angular rate, whereas in this case the masses and booms are generally jettisoned from the craft. The deployment rate of the booms thus not only has to be restrained, but this needs to be done in such a manner that it is safe and without unacceptable negative effects such as the booms wrapping or the boom offset angle reaching such a point where a steady state can not be readily regained.

The conceptual satellite under investigation uses a passive method of restraining deployment in the form of a rotary damper. This rotary damper acts on the pulley, around which the boom wires are wound, contrary to the pulleys rotation. As the wire booms are deployed by the rotation of this pulley the rotary damper acts to slow the linear deployment rate. The spinning satellite bus generates a centrifugal force on the boom tip masses pulling them outwards away from the bus driving the deployment. The friction in the deployment mechanism and the effects of the damper counteract this centrifugal force. Thus if the magnitude of the centrifugal force can overcome the static friction in the deployment mechanism and damper, then deployment will occur where the driving factor becomes the damping coefficient selected. This concept is illustrated in Figure 3.7.

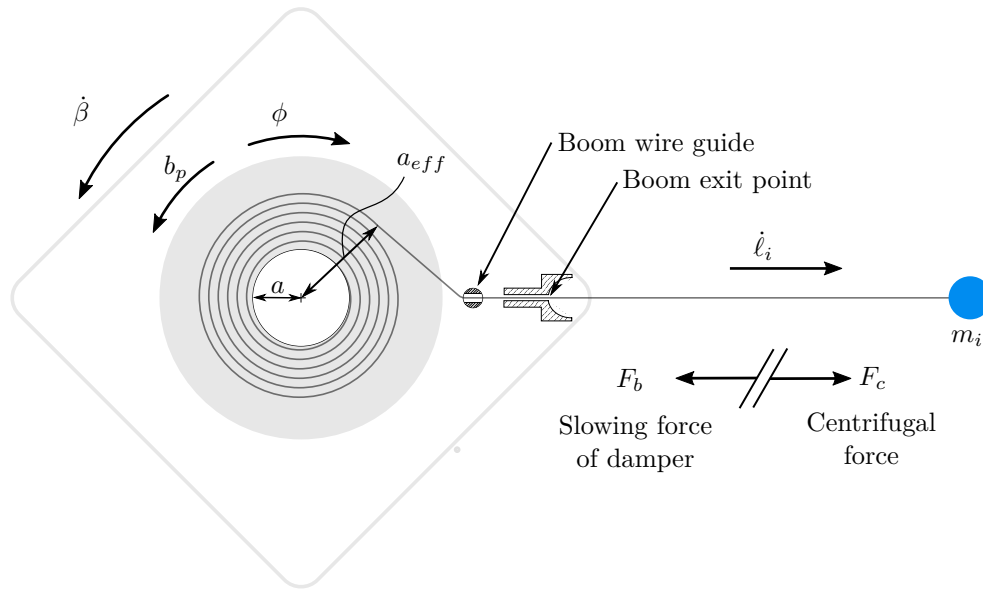


Figure 3.7: Pulley Mechanism

The centrifugal force acting on the tip masses and generated by the spinning satellite bus, assuming a small boom offset angle for θ_i , is given by

$$F_c = \sum_{i=1}^n m_i \dot{\beta}^2 (r + \ell_i). \quad (3.5.2)$$

The deployment, however, can easily develop a significant θ angle, making this an easily overcome oversimplification. Removing the small angle approximation to obtain a more accurate result for large angles of θ can be obtained by using the tip mass position in polar coordinates:

$$F_c = \sum_{i=1}^n m_i (\dot{\beta} + \dot{\theta}_i)^2 \sqrt{\ell_i^2 + 2 \cos(\theta_i) \ell_i r + r^2}. \quad (3.5.3)$$

More elegantly, because in the case of a deploying boom ℓ_i is a function of time, a fundamental approach can be taken using Newton's second law of motion $\vec{F} = m\vec{a}$, to obtain

$$F_c = \sum_{i=1}^n m_i \ddot{\ell}_i, \quad (3.5.4)$$

which yields very similar results to Equation 3.5.3. Equation 3.5.4 provides a more accurate result for the purposes of calculating the torque applied to the pulley, as this force is in line with the boom while the result produced by Equation 3.5.3 is orientated through the bus centre of rotation. The error induced by using Equation 3.5.3 over Equation 3.5.4 is, however, negligible for reasonable θ angles.

In order to drive the deployment rate using this centrifugal force it must be translated into a pulley torque. The torques acting on the pulley are those which are inflicted by the centrifugal force with the effective pulley radius, a_{eff} , acting as a lever arm, the opposing torque of the damper as well as any friction which may be present in the system. The sum of the torques acting on the pulley is

$$\begin{aligned} \sum T_p &= T_c - T_d - T_{fk} \\ &= F_c a_{eff} - b_p \dot{\phi} - F_{fk} = I_p \ddot{\phi}, \end{aligned} \quad (3.5.5)$$

where ϕ represents the time dependent rotation of the pulley within the deployment mechanism and F_{fk} the kinetic friction. Rotation of the pulley will only, however, occur if the torque applied to the pulley by centrifugal force is greater than the static friction F_{fs} . The static friction in the mechanism therefore determines the spin rate at which deployment will initiate. The pulley acceleration is thus given by:

$$\ddot{\phi} = \begin{cases} \frac{F_c a_{eff} - b_p \dot{\phi} - F_{fk}}{I_p} & , \text{ if } F_c a_{eff} > F_{fs} \text{ or } \dot{\phi} > 0 \\ 0 & , \text{ otherwise.} \end{cases} \quad (3.5.6)$$

The acceleration of the pulley, $\ddot{\phi}$, then directly drives the acceleration of the boom deployment $\ddot{\ell}_i$, depending on the radius of the pulley hub from which the boom unwinds and limited by the rotational damping. It is numerically possible for $\dot{\phi} < 0$ but not practically, as this would indicate the boom winding itself back in. The distinction is made that all booms are wound around a singular pulley hub and are constrained by the same pulley rotation and damping. The deployment acceleration of the booms can thus be calculated by

$$\ddot{\ell}_i = \ddot{\phi} a_{eff}. \quad (3.5.7)$$

3.5.4 Boom Winding

Large sailcraft can have sails orders of magnitude larger than the spacecraft body necessitating the use of exceedingly long booms. When stowed on a pulley in a coil these great lengths of boom wire will be required to coil over themselves several times, increasing the pulley radius to a_{eff} , and making this radius dependent on, not only the pulley hub radius, but on the usable volume of the pulley, the total boom length and the length of boom deployed thus far.

If the problem of calculating the effective pulley radius is phrased slightly differently, and the assumption that the boom wire packs perfectly is made then several solutions to the problem become apparent. If perfect packing is assumed then it is implied that the pulley winds such that each layer of winding lies exactly in line and above the preceding one, and the same perfect alignment applies along the width of the pulley as is illustrated in Figure 3.8. This assumption insinuates that the wire has a square cross section equal to

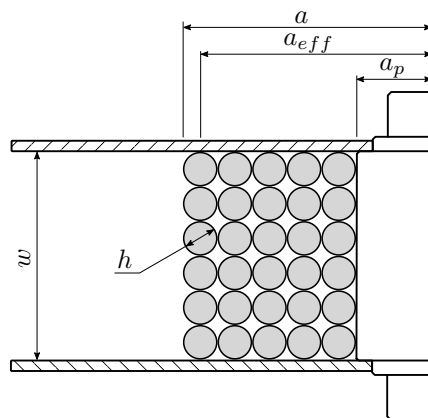


Figure 3.8: Perfect Boom Winding on Pulley

its diameter and this description of the assumption can greatly simplify the derivation of answers to the proposed question of what a_{eff} is for a given length of wound wire.

The simplest approach to the problem is to equate the volume of the pulley to that of the volume of the wire itself to find the solution,

$$\begin{aligned}
 V_{wire} &= V_{pulley} \\
 \ell_p h^2 &= \pi(a^2 - a_p^2)w \\
 \ell_p &= \frac{\pi w}{h^2}(a^2 - a_p^2).
 \end{aligned}
 \tag{3.5.8}$$

The effective distance which applies the deploying torque to the pulley is $a_{eff} = a - \frac{h}{2}$. Solving for the effective radius yields:

$$a_{eff} = \sqrt{\frac{h^2}{\pi w} \ell_p k + a_p^2} - \frac{h}{2}.
 \tag{3.5.9}$$

The length wound on the pulley is the final length of the boom less the already deployed length, $\ell_p = \ell_f - \ell$. A winding factor k , which will be a value less than 1, has been introduced into the equation to compensate somewhat for the perfect winding assumption - it is the ratio between the theoretically coiled length and that seen in practice. The winding factor unfortunately cannot be determined theoretically, it is dependent on the winding method employed, wire material and diameter and thus is difficult to determine and must be found by empirical tests. It is particularly sensitive to the wire diameter as a smaller wire diameter will coil less uniformly and with greater unpredictably. For simulated cases a perfect winding factor of $k = 1$ will be assumed.

If a single coil is considered, as would be the case if the pulley width was equal to the boom wire diameter, $w = h$, then the resultant winding would form a spiral. The arc length of an Archimedean spiral could then be used to calculate the length of the wire in a single spiral layer and multiplied by the number of these layers which would sit within the width of the pulley. A simplification of this approach is to consider the winding layers as many nested concentric circles. This leads to a far simpler solution as it is merely computing the sum of several circumferences. This pattern of concentric circles is assumed to continue along the width of the pulley as many times as the wire diameter will divide into the pulley width. First the number of circles, or windings, to sum needs to be determined,

$$N = \frac{a - a_p}{h}, \quad N \in \mathbb{Z} \text{ and } N > 0.
 \tag{3.5.10}$$

The total length is then the sum of circumferences multiplied by the number of windings in the width of the pulley,

$$\ell_p = \frac{w}{h} \sum_{n=0}^{N-1} 2\pi(a_p + hn). \quad (3.5.11)$$

If this is rearranged slightly and expanded one obtains the equation

$$\ell_p = \frac{w}{h} (2\pi a_p + 2\pi(a_p + h) + 2\pi(a_p + 2h) + \dots + 2\pi(a_p + h(N-1))) \quad (3.5.12)$$

$$= \frac{w}{h} (2\pi(Na_p + h(1 + 2 + \dots + (N-1))))), \quad (3.5.13)$$

in which Gauss' equation can be seen which states that the sum of integers from 1 to n is $\frac{n(n+1)}{2}$. In this case $n = N - 1$. Using this, the total length of wire wrapped on the pulley is

$$\ell_p = \frac{w}{h} \pi N (2a_p + h(N-1)), \quad (3.5.14)$$

where the length remaining on the pulley is the final boom length less that which has already been deployed, $\ell_p = \ell_f - \ell$. Using the quadratic equation to solve the polynomial for the positive number of turns and substituting in Equation 3.5.10 yields

$$a_{eff} = a_p + \frac{1}{2} \left(h - 2a_p + \sqrt{(2a_p - h)^2 - \frac{4h^2 \ell_p k}{\pi w}} \right). \quad (3.5.15)$$

An alternative but similar method of approaching the problem is to consider the winding along the width of the pulley. Each layer of winding can be considered to have the same winding radius and form a helical coil, with a pitch equal to h , along the width of the pulley. The helical arc length of a winding layer coupled with the assumption of concentric circles yields a wire length of

$$\ell_p = \frac{w}{h} \sum_{n=0}^{N-1} \sqrt{h^2 + 4\pi^2(a_p + hn)^2}, \quad (3.5.16)$$

a more complex expression than before which cannot be easily manipulated into a form to which a simplification such as Gauss can be applied. The summation may be computed as an integral of the form

$$\ell_p = \frac{w}{h} \int_0^{N-1} \sqrt{h^2 + 4\pi^2(a_p + hn)^2} dn \quad (3.5.17)$$

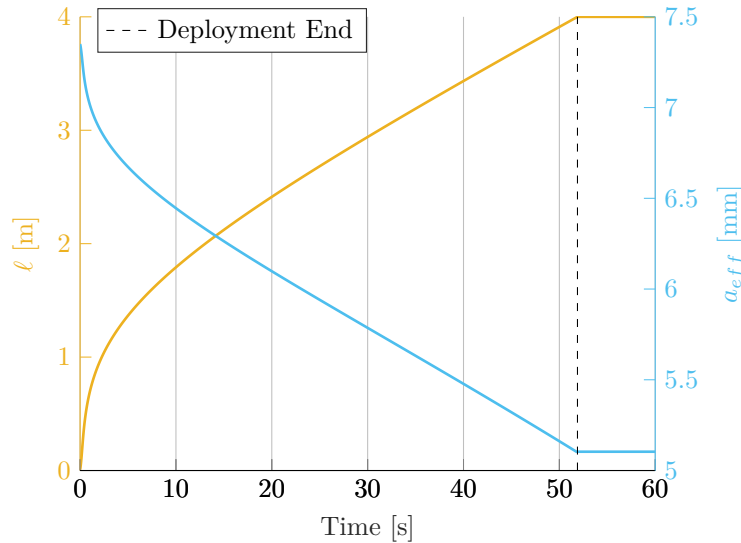
which cannot be solved for an explicit solution to a . An iterative approach would thus have to be taken, making this more computationally intensive than those mentioned before.

A practical spool with physical dimensions $a_p = 19.25$ mm and $w = 34$ mm was wound with cable 3.1 mm in diameter. Four layers of cable were wound as perfectly as possible onto the spool. The outer radius of the spool was measured to be 30.9 mm once wound. Note that this diameter is less than the theoretical outer radius with perfect winding of 31.65 mm. This is caused by the reality that the layer do not easily coil one above the previous but rather in a staggered fashion.

Table 3.2 presents the results of this experiment and how the theoretical methods compare. It can readily be seen that the method of concentric helices offers the closest solution to practice. The method of simple concentric circles however produced almost the same result at significantly less computational load. This is the method which will be used for simulation purposes. Figure 3.9 illustrates how the pulley radius decreases as the boom unwinds from the pulley. The results are those as used in Section 3.6.1 where a 4 m boom is deployed from a pulley with a base radius of $a = 5$ mm. The profile of the decreasing effective pulley radius is presented with the deployed boom length in Figure 3.9.

Table 3.2: Methods of Calculating the Length of Wire Wound on a Pulley

Method	Equation	ℓ_p [m]	k
Actual		6.608	1
Volumetric	3.5.8	6.477	0.980
Concentric Circles	3.5.14	6.588	0.997
Concentric Helices	3.5.17	6.590	0.997

**Figure 3.9:** Changing Effective Pulley Radius

3.6 Passive Deployment

In order to understand and draw comparisons between different deployment strategies several cases are simulated. The physical setup of the satellite is constrained, as mentioned, to a 3U, 3 kg satellite with 4 m booms. Other key nominal simulation parameters concerning the spacecraft configuration are provided in Table 3.3. Cases deviating from this standard configuration will be discussed on a case by case basis, to demonstrate the differing deployment behaviours that may be observed.

Passive control of the boom deployment is easily conducted through the use of rotational damping of the pulley. The rate of the deployment as well as the magnitude of the induced dynamics are determined predominately by the selection of the pulley damping coefficient, the tip mass and the initial bus spin rate. The tip mass used is subject to constraints such as the allowable volume and contribution towards the satellite mass budget. It is thus useful to select the tip mass to ensure sufficient centrifugal force is generated at the post-deployment steady state nominal spin rate, and tune the pulley damping to achieve the desired deployment rate. The primary variables that can easily be managed to determine the deployment rate are the initial spacecraft spin rate, the pulley damping, tip masses and pulley radius.

In order to improve the clarity of the results and reduce computational load only a quarter of the full sail model will be simulated as per the equations of motion in Appendix B.1.3. This does not affect the results obtained as the booms would behave identically for a given set of

physical parameters and initial conditions. The effects on the system when this assumption does not hold true will be discussed in Section 3.8.3. This needs to be considered as some aspects of the system are dependent on the nett effect of all the booms, such as those relating to the torques on the pulley, and need to be scaled accordingly.

Table 3.3: Simulation Parameters

Parameter	Value	Units
r	70.7	mm
m_b	3	kg
I_b	15	$\text{g} \cdot \text{m}^2$
m_i	20	g
b	0.33647	$\text{mN} \cdot \text{m} \cdot \text{s}/\text{rad}$
ℓ_f	4	m
ℓ_0	7.5	mm
F_{min}	54.83	$\text{mN} \cdot \text{m}$
a_p	5	mm
I_p	5.209	$\text{mg} \cdot \text{m}^2$
b_p	3	$\text{mN} \cdot \text{m} \cdot \text{s}/\text{rad}$
w	1.9	mm
h	0.2	mm

As the rate of deployment is governed by the centrifugal force, the simplest means by which the deployment rate can be controlled is to vary the spin rate of the spacecraft. There are several governing strategies by which the spin rate of the craft can be controlled. The simplest means is to ensure that the body rate is sufficient to initiate deployment and ensure that the final rate will be acceptable, while maintaining the sail stability and the required minimum centrifugal force F_{min} . This, however, may be problematic for large sails where the sail inertia is comparable to the spacecraft body, requiring a high initial spin rate. The maintained centrifugal force on the boom tips can minimise the undesired dynamic effects, which could cause harm to the spacecraft. The deployment rate can be passively controlled through the use of a rotationally damped pulley, as mentioned or actively by some form of actuator, be it a motor or electronic break of some form.

3.6.1 Case 1: Free Damped Pulley Deployment

To freely deploy the full length of the booms without any additional inputs or control, the satellite needs to have a spin rate large enough that the minimum centrifugal force can still be maintained at deployment completion. The total spacecraft moment of inertia increases by a factor of 44.46 from deployment start to completion - a decrease in angular rate is caused by this increase in inertia. At a steady state bus spin rate of $\dot{\beta}_{ss} = 0.13$ rps the minimum centrifugal force can be maintained on the boom tips, in the deployed state. Achieving this steady state spin rate without additional input to the system requires an initial spin rate of 11.3 rps. This is a high rate of rotation for a spacecraft and may be challenging for a small satellite to stably achieve and maintain. This scenario is presented here as the first case under consideration as it presents the dynamics of a natural and unforced free damped deployment.

Satellites with means of achieving stable spin at high rate would best make use of this method. This means of deployment requires neither controlling inputs nor any information on the state of deployment, such as the amount of boom wire deployed, during deployment.

This process can also be conducted in stages where only a portion of the boom is allowed to deploy at a time and the bus spin rate can be recovered between.

The standard model, as was presented in Table 3.3, was simulated as case one; with an initial spin rate of $\dot{\beta}_0 = 11.378$ rps. Deployment and its effects on the system as a whole were allowed to proceed uninfluenced. The results of this are presented in Figure 3.10 (the changing boom length is as was previously seen in Figure 3.9). The vertical black dashed line in the figures represents the time at which deployment was completed.

As deployment commences at $t = 0$, the bus rate (Figure 3.10d) immediately begins to drop steeply from the increasing inertia. This in turn causes the centrifugal force (Figure 3.10a) to drop. A lower centrifugal force on the boom tips masses applies a smaller torque to the pulley and slows the deployment rate (Figure 3.10b).

Figure 3.10e shows the in-plane boom offset angle θ . Within the first second after deployment θ grows to 25.06° from nominal, lagging the bus. While this is a large offset angle, the displacement of the boom tip is quite small as ℓ at this point is still reasonably small at 211.7 mm. This initial spike in θ promotes making the boom length longer than necessary for a given sail area. Incorporating additional length in the boom, beyond the sail corner, would allow the effects of this large offset angle on the sail membrane to be minimised. The possibility of an uneven deployment or damage to the sail membrane by the potentially large tug inflicted by this angle growth and its recovery would be reduced.

As the bus rate slows the boom offset angle is given an opportunity to recover somewhat. As the boom is still deploying however θ cannot recover completely because of the increasing length. These causes a time varying mean offset angle around which oscillations are induced in the boom angle as it progresses through the remainder of the deployment process. These oscillations induced while deployment is still under way are akin to those seen upon deployment completion but rather around the equivalent equilibrium point at the given length and deployment rate at that point in time.

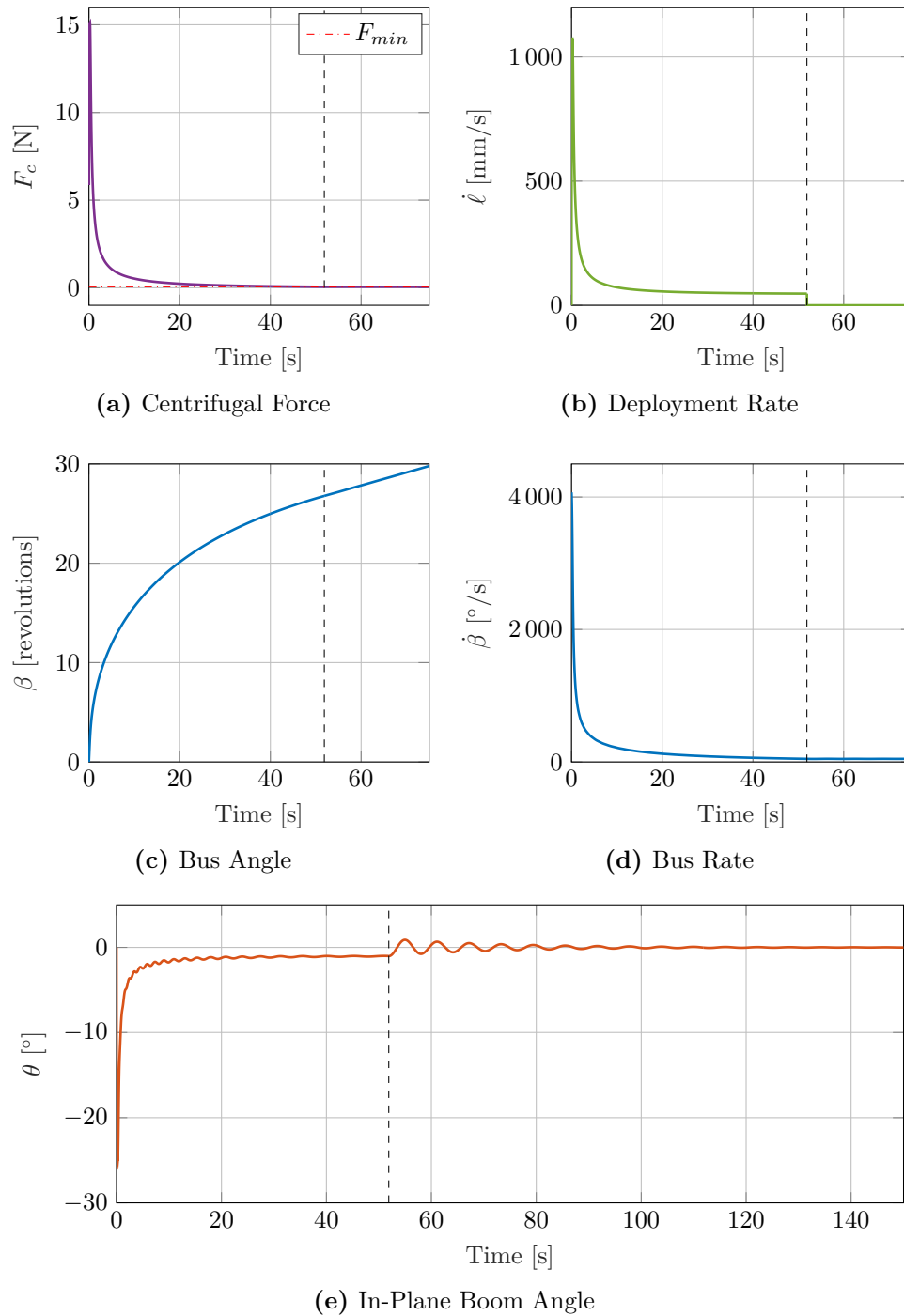
Upon completion of deployment, at $t = 51.89$ s, the centrifugal force F_c and bus rate $\dot{\beta}$ become constant. As the bus rate is no longer decreasing and $\dot{\ell} = 0$ the in-plane boom angle can fully recover. The behaviour now is the same as that of a spinning classical double pendulum with an initial offset angle of the second link, as was discussed in Section 3.4. The angle θ oscillates around the nominal angle until the damping in the wire causes it to settle. In this case the boom oscillations are gentle and the resultant oscillations in the bus rate almost imperceptible as the energy of the satellite bus is far greater than that of the tip masses.

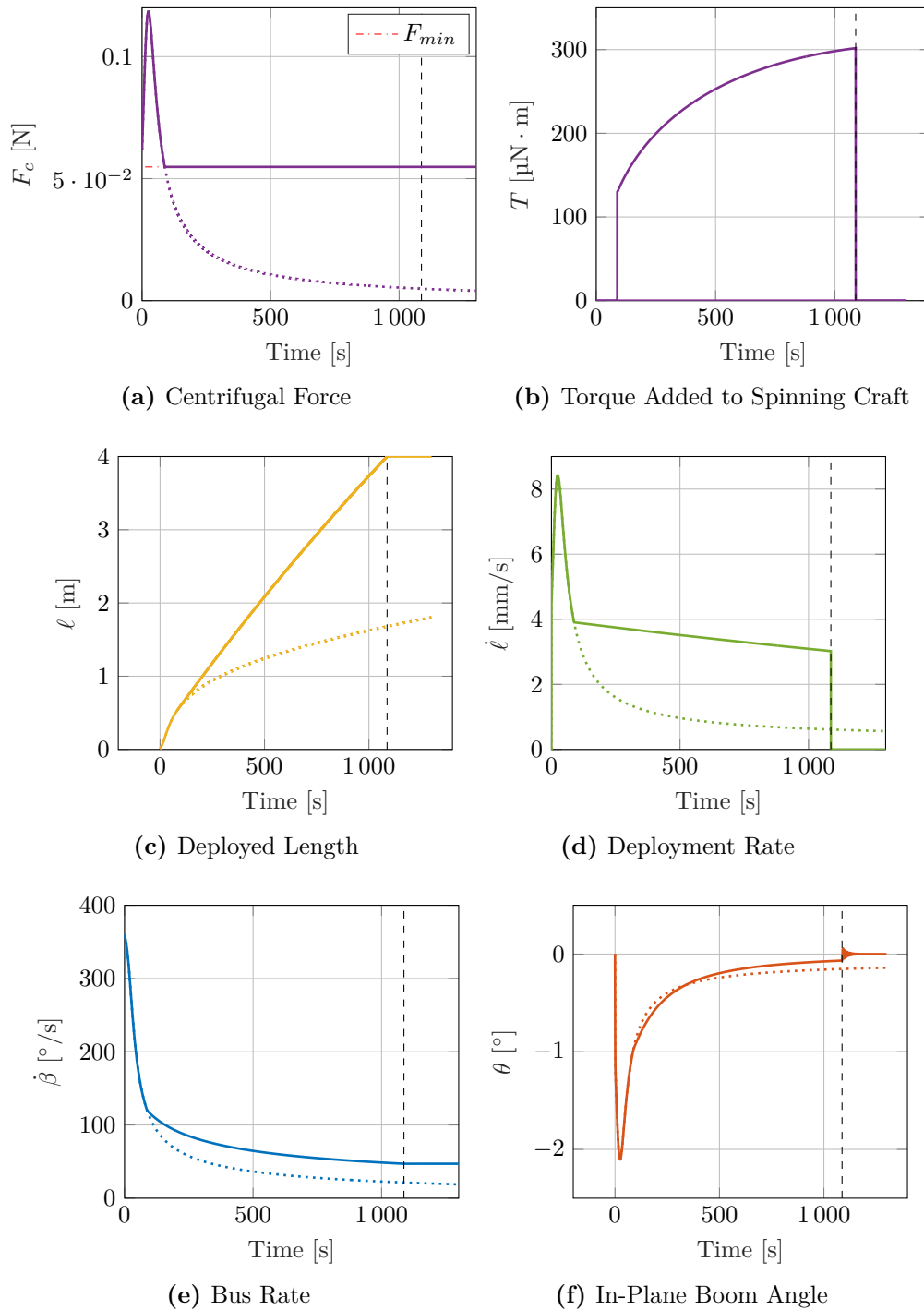
As mentioned, achieving such a high initial bus rate would prove technically difficult, particularly for smaller satellites which do not have budgets for thrusters or other high impulse means of spinning up. A solution would be to lower the initial rotation rate requirement and conduct deployment over a longer period of time while adding energy to the system as deployment progresses to ensure the minimum centrifugal force requirement is met.

3.6.2 Case 2: Ensured Centrifugal Force Deployment

This second case was simulated and the results are presented in Figure 3.11. The deployment was allowed to naturally continue to the point where the centrifugal force dropped to F_{min} . A controller is then activated to maintain $F_c \geq F_{min}$. The resulting graphs show the controlled dynamics as a solid line and the dynamics if control was absent as a dotted line. The point at which the control takes over is clear from where the two lines diverge at $t = 88$ s. The point at which deployment completes for the controlled case is again shown by the vertical dashed black line.

The controlling actuator is assumed ideal in that it can readily respond and no limits were in place for the torque deliverable or response time thereof. The centrifugal force and torque

**Figure 3.10:** Case 1: Free Damped Pulley Deployment

**Figure 3.11:** Case 2: Ensured Centrifugal Force Deployment

applied can be seen in Figure 3.11a and Figure 3.11b respectively. As F_c reaches the minimum threshold the controller activates and induces a torque on the spacecraft body to counteract the effect of the increasing inertia, decreasing the rate at which the satellite spin rate slows as seen in Figure 3.11e.

The lower initial spin rate leads to a significantly more gentle start to deployment, and the in-plane boom offset angle reaches a maximum of only $\theta = -2.1^\circ$. This has a smoother recovery as the bus rate does not slow as dramatically as in the previous case and the boom tips are not able to acquire as much energy. For this same reason there is little oscillation of θ as it recovers. The magnitude of the oscillation at the time of deployment completion is also smaller. The rate of boom deployment becomes almost linear from the time that F_c becomes maintained, as the force acting on the pulley is now constant.

This method of control presents significantly more docile dynamics than the previous case but control is required during the deployment process.

3.6.3 Case 3: Centrifugal Force Management

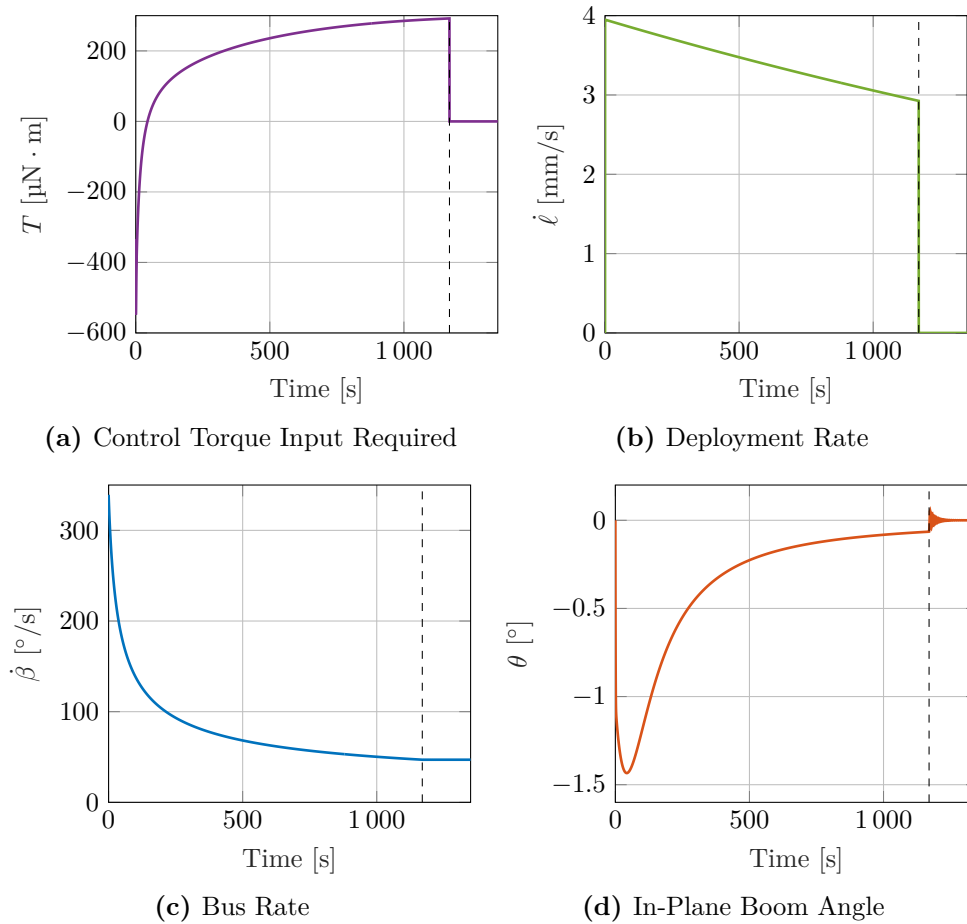
The deployment process can also be controlled using the centrifugal force generated as the determining factor driving the bus spin rate. This may be desirable, in some form, so as to not surpass the physical limits of the materials and components used. While not of paramount concern for small sails, this needs to be taken into consideration for large sails where the long boom lengths can generate significant forces in the boom. Without monitoring or management of this increasing force, booms could snap and would need to be designed to withstand the higher forces during the deployment process. This method does however require a sufficient actuator to induce the required body torques as well as knowledge of the already deployed length of boom wire.

This was investigated as case three, where the bus rate was driven to satisfy a set centrifugal force. The target centrifugal force was set at $F_c = F_{min}$ to ensure that the minimum centrifugal force was matched at all times during deployment. The bus rate during the deployment process is then governed by Equation 3.5.3 rearranged such that $\dot{\beta}$ is the subject. The results of using this method of control are presented in Figure 3.12.

The boom deployment rate is immediately apparent. It is linearly decreasing from the start, to the end of deployment at $t = 1169.8$ s. As the centrifugal force applied to the pulley is maintained at a constant value, the force applied to the pulley, by the booms, is constant. The diminishing deployment rate is a result of the decreasing pulley radius a_{eff} as the boom unwinds. The reduction in the effective pulley radius decreases the torque applied to the pulley and the deployment rate thus slows. The shorter the booms or the larger the pulley base radius is, the smaller this effect will be. Had the changing effective pulley radius not been considered the deployment rate would have remained constant. The future need for large sails will require long boom lengths to be stowed in highly constrained volumes suggesting that this changing radius effect cannot be ignored when modelling the general problem. The mean deployment rate for this case was 3.413 mm/s.

As the starting bus rate was as low as permissible by the minimum centrifugal force requirement this would be the lowest energy solution considered. This results in the smallest boom deflection angle of $\theta = -1.44^\circ$.

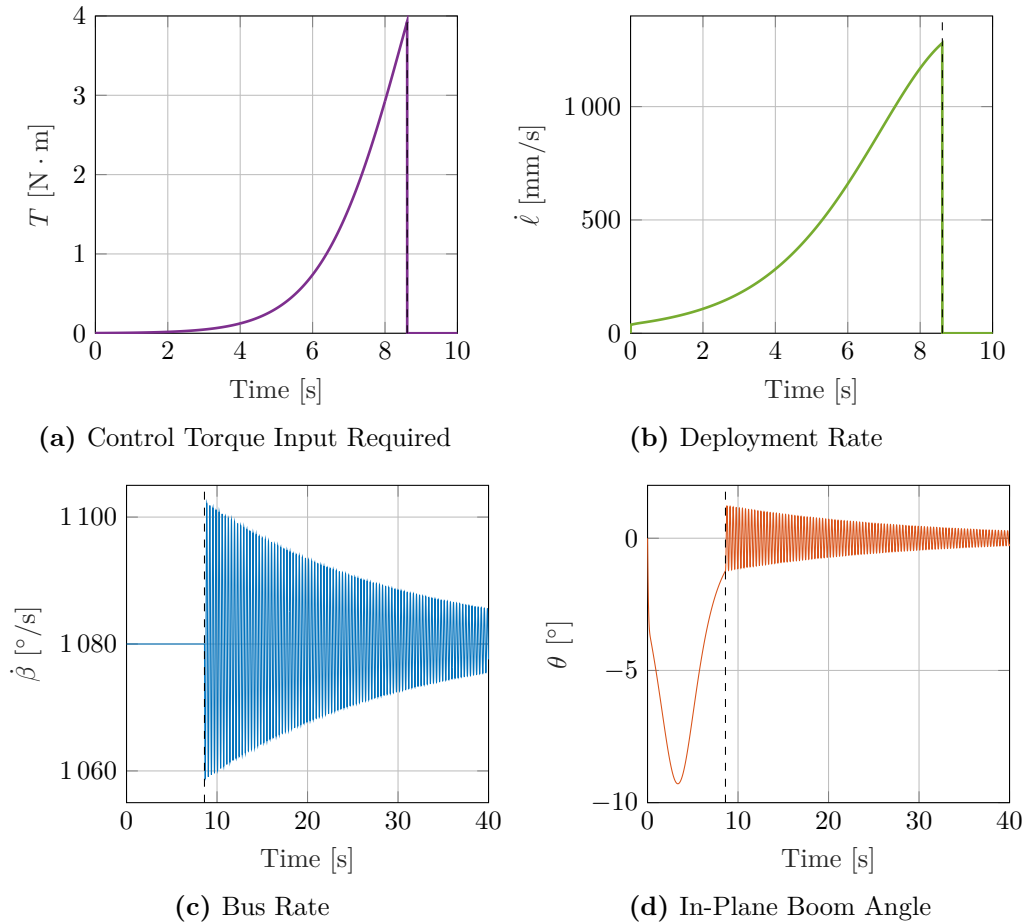
A body torque was applied in order to manage $\dot{\beta}$ such that the constant centrifugal force was maintained as seen in Figure 3.12a. This application of torque combined with the increased total inertia slows the bus spin rate reasonably rapidly at first, and more gently as deployment progresses. The deployment commenced at a bus spin rate of $339.22^\circ/\text{s}$ and decreased to $47.02^\circ/\text{s}$ by completion (Figure 3.12c).

**Figure 3.12:** Case 3: Centrifugal Force Governed Deployment

3.6.4 Case 4: Bus Rate Controlled Deployment

Assuming a suitable actuator is in place, deployment can be conducted by maintaining a constant bus rate. As the bus rate and tip mass remains constant the centrifugal force becomes dependent on ℓ and $\dot{\theta}$. In this case the bus rate is maintained at a constant $\dot{\beta} = 3$ rps throughout the deployment process and allowed to freely change once deployment is complete. The results are depicted in Figure 3.13. This strategy of conducting deployment is not especially practical as it requires significant externally applied torque relative to those previously discussed (Figure 3.13a). It does however offer insight into the behaviour of deployment when the extending boom has a smaller effect on the bus, such as when the moment of inertia increase of the craft is not particularly large. This also provides information to which ground test results can more easily be compared to, as the effects of gravity and atmospheric interference may be overcome and negated by maintaining a constant rotational rate and exaggerating the dynamics. Merely to overcome the increased moment of inertia of the spinning system a peak of $4 \text{ N} \cdot \text{m}$ of input torque is required to maintain spin.

If the simplified approach is taken to calculate the centrifugal force and thus determine the deployment rate, as in Equation 3.5.2, one would see a more linear increase in $\dot{\ell}$. However, the in-plane offset angle of the boom affects this, a large θ angle effectively reduces the centrifugal

**Figure 3.13:** Case 4: Constant Bus Rate Control

force acting on the boom tip by increasing its proximity to the centre of system rotation. The decreasing effective pulley radius also has an effect in decreasing the deployment rate as has been seen. This yields the distinctly non-linear deployment rate seen in Figure 3.13b.

A distinct effect of maintaining a constant bus rate is that the system has significantly more energy by deployment completion than previously discussed cases. This leads to a more prominent θ angle and more chaotic recovery. Deployment proceeds incredibly quickly, and by the late deployment stage, the boom tip has amassed a significant portion of the systems energy. This energy must all be dissipated in the boom wire or transferred back to the satellite bus before equilibrium can be reached.

Even though the boom offset angle is small by deployment completion, $\theta_{t=t_{deployed}} = -1.231^\circ$, the rate of boom deployment is high at $\dot{\ell} = 1.28$ m/s. This causes a large impulse in $\ddot{\ell}$ as the deployment is suddenly brought to a halt and a large force is applied to the satellite bus. Oscillations in the bus rate ensue. In a completely passive deployment where no information is known about the state of deployment, this oscillation of the bus rate can provide information on $\dot{\ell}$ and θ at the point of deployment completion and be used to detect that deployment has halted. The bus rotation rate at the end of deployment is $1080^\circ/\text{s}$ as was maintained throughout the process. As control over the bus rate is released at this time, energy is allowed to easily transfer between the boom tip mass and the satellite body. For this reason some energy from the body is dissipated in the wire damping and the steady

state bus rate is lower at $\dot{\beta}_{ss} = 1077.29^\circ/\text{s}$ once all oscillations have dissipated.

3.6.5 Passive Deployment Cases Summary

A summary of the results from the four passively deployed cases discussed is given in Table 3.4. Case one through three all have final steady state bus rates of $\dot{\beta}_{ss} = 47.02^\circ/\text{s}$ as a result of maintaining F_{min} . It is also apparent from the results that the maximum magnitude experienced by θ is most influenced by the initial rotation rate $\dot{\beta}_0$. As expected, the slower the booms are deployed the more subtle the negative influences on the dynamics are.

Table 3.4: Passive Damped Pulley Deployment Case Results

Variable	Case 1	Case 2	Case 3	Case 4	Unit
Control strategy	None	$F_c \geq F_{min}$	$F_c = F_{min}$	$\ddot{\beta} = 0$	
$t_{deployed}$	51.87	1086.92	1169.85	8.6122	s
$\dot{\ell}$	76.97	3.673	3.413	463.57	mm/s
$\dot{\beta}_0$	4069.11	360.00	340.24	1080.00	$^\circ/\text{s}$
$\dot{\beta}_{ss}$	47.02	47.02	47.02	1077.29	$^\circ/\text{s}$
$\theta_{t=t_{deployed}}$	-1.022	-0.067	-0.046	-1.231	$^\circ$
θ_{max}	-25.03	-2.104	-1.434	-9.286	$^\circ$

All the passive deployment cases investigated proceeded with no input other than the control of the bus spin rate. The boom deployment rate was not directly managed in any way and in Cases 1 and 4 no information regarding the deployment state was required or used. This shows the validity of passive deployment where rotational damping applied to the pulley is used to retard the rate of deployment. It also shows how the deployment time and the magnitude of the dynamics experienced can vary greatly based on the deployment control strategy used.

3.7 Active Deployment

The use of an active deployment strategy is investigated here. This may be more preferable to some missions as it offers greater control over the process as a whole. However as a consequence of this, the deployment mechanism needs to be far more complex and involve additional sensors and actuators to monitor and drive deployment. While active deployment of a spinning solar sail with wire booms has not yet been conducted, the deployment of wire boom mounted scientific instrumentation and similar devices is commonly done in this manner [54; 66; 67; 68; 69; 71].

Here the same satellite model is used for simulation but the effects of damping on the pulley around which the booms are stowed is eliminated and $\dot{\ell}$ is directly controlled. The initial bus rate was set to $\dot{\beta} = 4069.11^\circ/\text{s}$, as in case one of the passive scenarios, in order to eliminate any effects induced by the requirement to maintain F_{min} . The deployment rate of the booms was fixed at $\dot{\ell} = 10\text{ mm/s}$ for the entire deployment process. The effects on the bus rate and in-plane offset angle are given in Figure 3.14. The profile of $\dot{\beta}$ is similar to that of the passive free deployment case presented earlier, albeit more gentle in decline as this is a function of the increasing system inertia. As there is no spike followed by slowing of the deployment rate the boom offset angle remains constant until deployment completion. As θ does not change throughout deployment it remains small and with low energy. Recovery of the angle is thus gentle and has little effect on the bus.

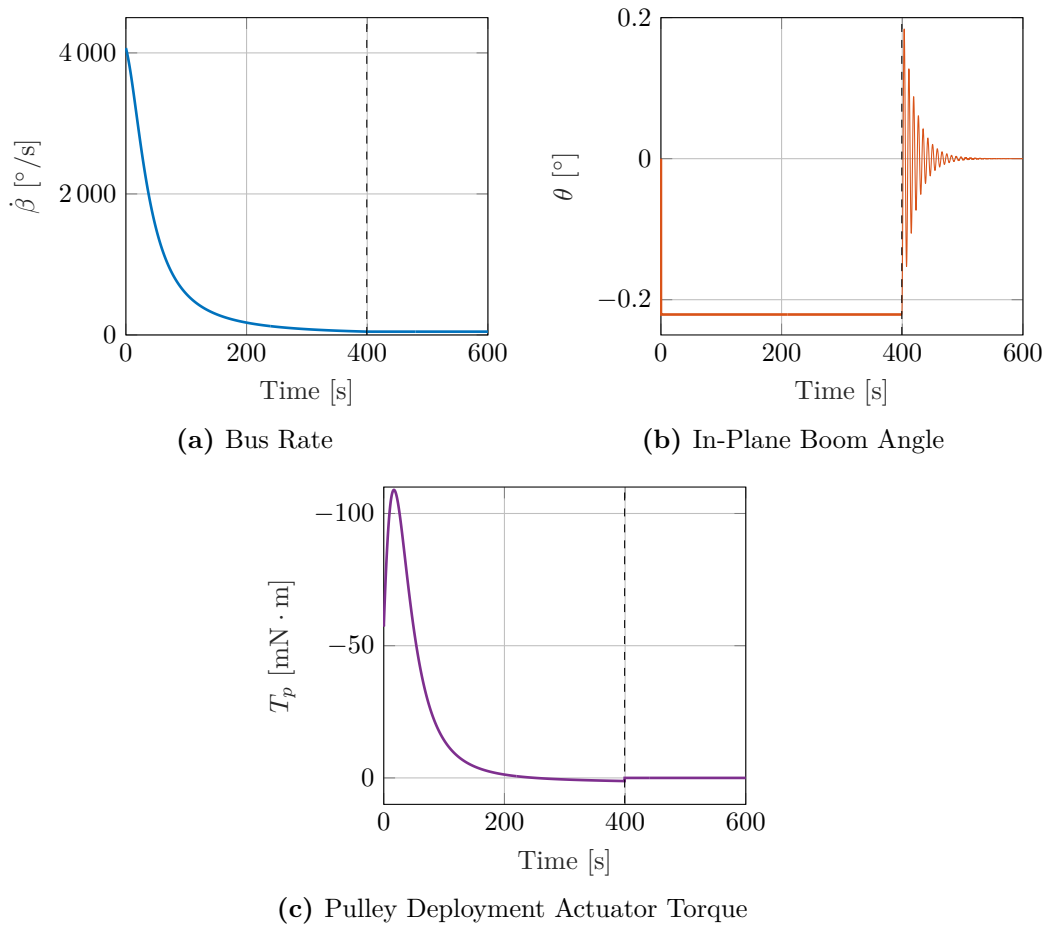


Figure 3.14: Active Deployment Rate Control

It should be noted that for the purposes of this method of deployment the actuating motor of the pulley will be required to withhold the boom deployment more than drive it onwards as the centrifugal force increases. The torque which needs to be applied to the pulley to maintain this deployment rate is given in Figure 3.14c. This reaches a peak of $108.9 \text{ mN} \cdot \text{m}$ counter to the direction to pulley rotation. This is modelled with no kinetic friction in the pulley or actuator and is thus a worst case. The use of a highly geared motor to increase dynamic friction and/or a gearbox which cannot be back driven would prove advantageous to decreasing this torque requirement. In the final seconds of deployment a positive pulley torque is applied in order to maintain the constant boom deployment rate. This is caused by the low bus rate and resultant low centrifugal force pulling on the booms, had the initial bus spin rate been slightly higher, or a positive torque been applied to the bus spin rate, this could be avoided and there would be no need to any positive torque to be applied to the pulley at any time during the deployment.

The constant bus offset angle is determined by the bus spin rate and the deployment rates used. Figure 3.15 presents a comparison of how changes in these parameters affect the in-plane offset angle and, consequently, the effect that recovery of this angle will have on the system. The rate of boom deployment has an almost linear effect on the in-plane offset angle experienced, where larger deployment rates cause larger offset angles for a given initial bus

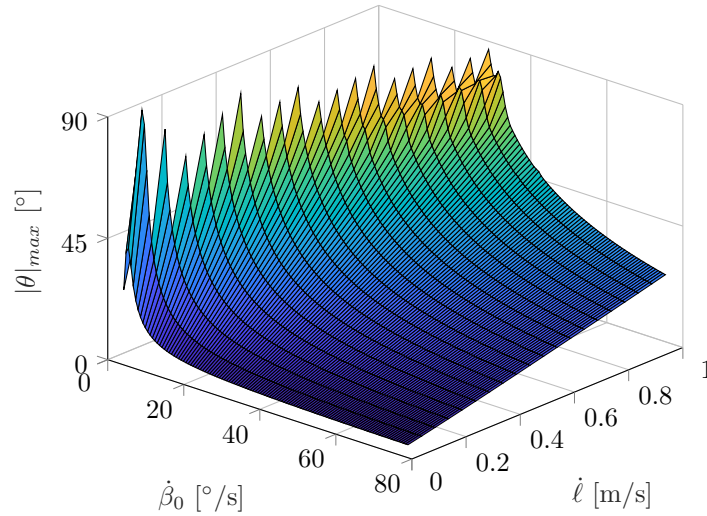


Figure 3.15: Effects of Deployment and Initial Bus Rate on In-Plane Boom Offset

spin rate.

To demonstrate the effects of differing initial bus rates on the in-plane offset angle of the boom the minimum centrifugal force requirement was removed. In Figure 3.15 it is seen that the lower the initial bus rate the further from the nominal the boom angle extends as the correcting centrifugal force is lower. The angle increases sharply for low rates under $\sim 25^\circ/\text{s}$. A cut off was placed at $\theta > 90^\circ$ for simulation purposes. An angle this high would not be practically maintainable as a high risk would be posed to the sail. With even such a tolerant threshold there are still many combinations of low bus spin and high deployment rates where deployment fails quickly from the high offset angle. This is seen in Figure 3.15 where β_0 is small and $\dot{\ell}$ is large resulting in high boom offset angles and the potential for boom wrapping to occur. Deployment is not possible using these inputs and there is thus no data therefore in this region of Figure 3.15. Note that no limit was placed on the minimum allowable centrifugal force in this instance. The region of deployment failure due to the growth of θ demonstrates why a minimum tolerable centrifugal force needs to be specified to avoid scenarios such as this.

3.8 Practical Deployment

The simulated scenarios discussed have several simplifying elements to them, including the modelling of the booms as rigid members when in reality they are flexible, reducing the system model to a single boom and assuming all booms are identical, and constricting the satellite from moving in inertial space. A number of the simplifications are addressed and discussed here as well what the effects may be without the introduction of these reductions in the system complexity.

3.8.1 Boom Node Elements

The boom was modelled as consisting of only a single node at the boom tip. This is, as far as modelling aspects go, one of the single largest simplifications made in an effort to reduce the complexity of the derived dynamics and equations of motion. The dynamics of a double pendulum are significantly more complex to derive and analyse than that of a single degree of freedom pendulum, and the addition of more degrees of freedom would quickly cause the

derivation of the equations of motion to become excessively large and unwieldy. A diagram illustrating how the boom would be modelled with multiple nodes and degrees of freedom is shown in Figure 3.16.

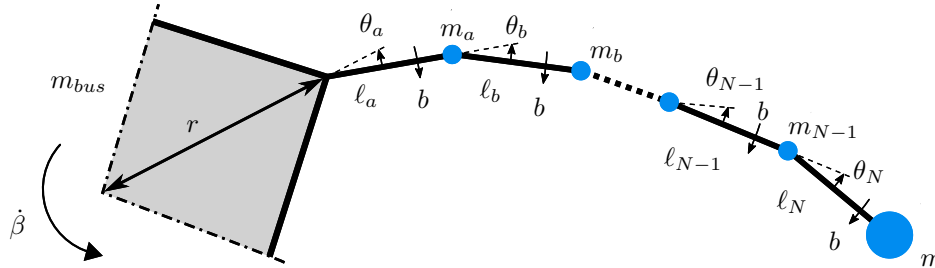


Figure 3.16: Multi-Node Boom

When considering the physical parameters of the individual boom nodes it is apparent that the equivalent mass of a central node is orders of magnitude smaller than that of the tip mass, leading to them contributing a smaller effect to the overall energy of the system. The offset angle between nodes would provide an indication of the curvature of the boom as deployment progresses, and the damping in individual node segments would remain equal as this property is independent of the distance between nodes.

The use of a multi-node boom model was investigated by Jordaan [29] and it was found that at low centrifugal forces the offset angles between nodes varied, indicating a boom curvature, but as the centrifugal force increased the angular offset between nodes would tend to zero and the overall boom offset angle would be dominated by that of the first node. Based on those findings and the fact that there is already a constraint placed on the minimum centrifugal force allowed, the internal boom nodes can safely be eliminated from simulation when investigating the general trends of the deployment process. However, if the sail construction required that the sail membrane be attached at regular points along the wire boom then the approach of a multi-node boom would need to be used as the sail membrane would have a significant effect on the observed dynamics.

3.8.2 Booms as Euler Beams

Euler-Bernoulli beam theory is most often used in structural or mechanical engineering analysis and is applied to long, thin, stiff members. The theory allows the formulation of equations describing the continuous shape of the beam along its length. The shape effects of dynamic loads on beams can also be derived using Euler-Bernoulli beam theory together with Lagrangian mechanics to obtain a continuous time dependent solution.

Deriving continuous solutions for the deployment of a spinning solar sail boom would prove highly complex as it would involve the use of multiple reference frames, and the form of the equations would have to change throughout simulation to account for the increasing length of the booms as they deploy. The use of purely energy-based Lagrangian mechanics allows for a discrete solution to be easily and procedurally derived for the system, which is more readily adaptable in that simulation conditions can be easily altered and the model can be easily expanded. The Euler-Bernoulli approach provides a polynomial curve solution representing the deflection shape of the beam.

3.8.3 Unbalanced Deployment

The assumption made that all booms of the solar sail are equal in dynamic behaviour can easily be rendered false in practice. The practical world is not ideal and any unbalanced features on the satellite will have effects on the deployment, and the craft as a whole. The highly non-linear and chaotic equations of motion are sensitive to the initial conditions and physical parameters. In practice, differences between booms can be present, such as variation between tip masses, differences in initial boom lengths and errors in assembly of the deployment mechanism.

The behaviour of the unbalanced dynamics is developed for non-ideal cases, where discrepancies may be present between booms on the satellite. As imbalances in the deployment will induce movement of the spacecraft body around the centre of mass in inertial space the problem is approached from this perspective. The equations of motion were derived using Lagrangian mechanics, and the derivation script previously discussed, to obtain a description of a multiple boom system in inertial space. The variable vector for a system with four booms, as per Figure 3.3 on page 28, takes the form

$$\mathbf{p} = [P_x \ P_y \ \beta \ \theta_1 \ \theta_2 \ \theta_3 \ \theta_4 \ \ell_1 \ \ell_2 \ \ell_3 \ \ell_4]^T, \quad (3.8.1)$$

which is significantly larger than that of the simplified single boom case.

The deployment of a simple unbalanced case is to be investigated and for this reason it is unnecessary to model each boom as a unique member. A slightly simplified approach is to model the system with a single unique boom and the remaining three as identical booms such that $\theta_2 = \theta_3 = \theta_4$ and $\ell_2 = \ell_3 = \ell_4$. This reduces the variable vector from 11 components to 7, greatly reducing the computational complexity of the derivation and simulation of the problem. Provided that booms two through four are presented with identical physical parameters and initial conditions, and the relevant aspects of the spacecraft are scaled correctly this simplification hold true. The simplified two boom system can be seen in Figure 3.17. The derived equations of motion for this case are too large to practically present in this document and are thus omitted. The orbital motion energies of the satellite are disregarded for simplicity and the spacecraft as a whole is seen as an initially inertially stationary two dimensional object floating in space. The problem is again investigated as a two dimensional system in the sail plane.

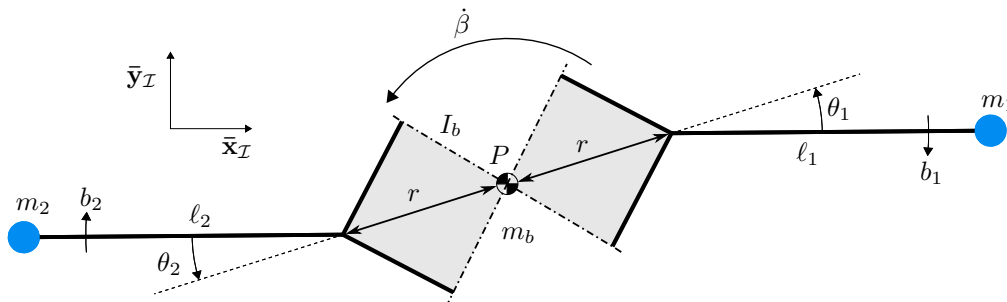


Figure 3.17: Two Boom System

The unbalanced deployment will cause the sail and its deployment to exert resultant forces on the satellite in the sail plane. These resultant forces will induce torques on the satellite body around the centre of mass causing angular oscillations or "wobbling" of the satellite in possibly multiple axes. The resultant force which the sail exerts on the satellite body,

here denoted by F , and the torque which it may induce is illustrated in Figure 3.18. Out of sail plane oscillations may be induced by these unbalanced deployment oscillations although these out of sail plane effects are not here investigated.

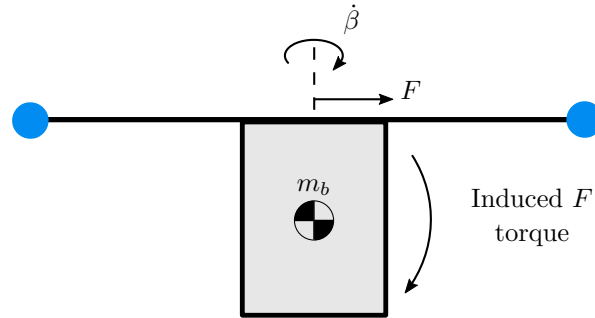


Figure 3.18: Induced Body Torque Illustration

3.8.3.1 Varying Tip Masses

There is a likelihood that the sail will not deploy evenly if not properly stowed. Due to uneven packing, folding or friction one segment may be released to a greater or smaller extent than another. This will result in imbalances in the centrifugal forces acting on the booms and satellite body. The effects of this on the deployment and spacecraft as a whole are to be investigated and understood.

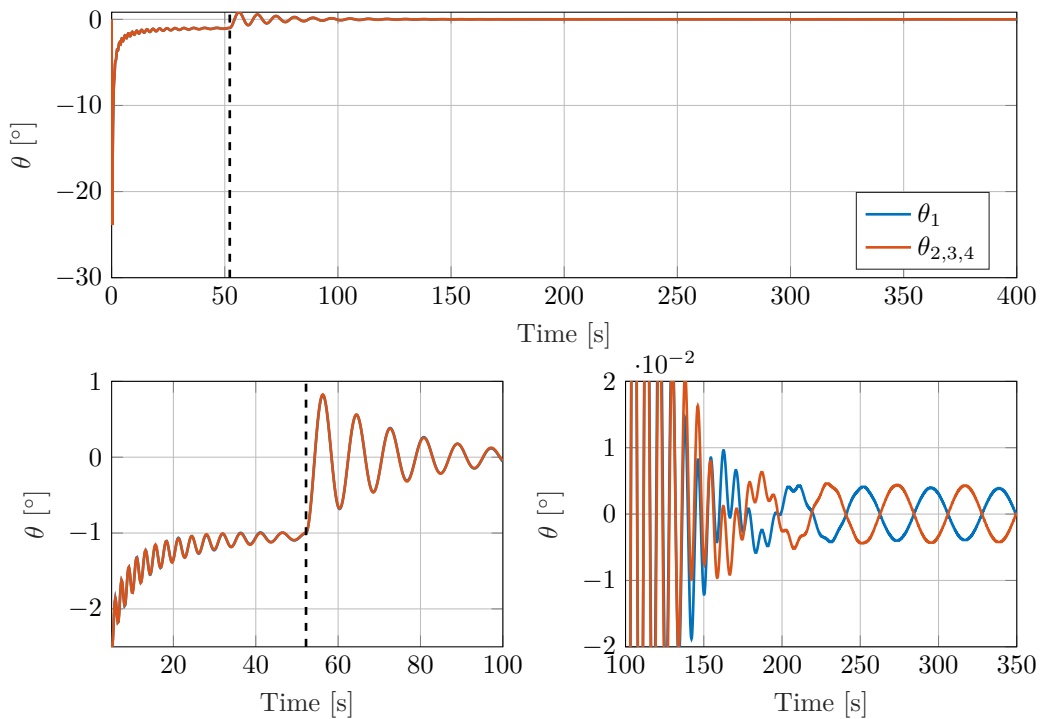


Figure 3.19: In-Plane Boom Offset with Unbalanced Tip Masses

As mentioned in Section 3.1.2, the equivalent tip mass of a deployed quarter sail is $m_{se} = 6.16$ g. Approximately a third of m_{se} , or 2 g, will be added to boom one and not boom two to induce the desired imbalance. It should be noted that this is a improbable practical scenario as it would require a third of a quarter sail segment to be dislodged from its stowed position at deployment initiation. The trends observed however remain true and this exaggerated value is used to convey them with enhanced clarity.

Using matching simulation conditions as in Case 1 of the damped pulley deployment with the addition of the increased boom one tip mass, simulation produced the following presented insights. Figure 3.19 presents the in-plane boom offset experienced by the booms during and post deployment. The general trend witnessed over the entire simulated time frame matches that as in Section 3.6.1 with slightly more prominent oscillations during deployment. The booms are in phase for the entirety of deployment and a short time thereafter, it is as the major oscillatory motion starts to die out that a significantly different trend emerges. There comes a point at approximately $t = 172$ s where the two booms go from a matching phase to out of phase in their oscillations.

An imbalance in a spinning object causes nutation of the object around its centre of mass. The force driving this nutation of the satellite is presented in Figure 3.20 where the forces in the sail plane and how these forces change with time during the deployment process are shown. The magnitude of this force increases as the imbalance increases with the increasing boom length. The rotational angular body oscillations are induced from these forces inducing torques around the satellite centre of mass. The magnitude of the force is influenced not only by the mass imbalance but also by the unbalanced in-plane boom angles resulting from the unbalanced mass. This results in larger forces in the initial moments of deployment when there are high θ angles present. , After deployment has completed, and the boom angles have been damped out and assumed their nominal positions the steady state wobble seen is a result of the unbalanced mass only and not other unbalanced dynamics.

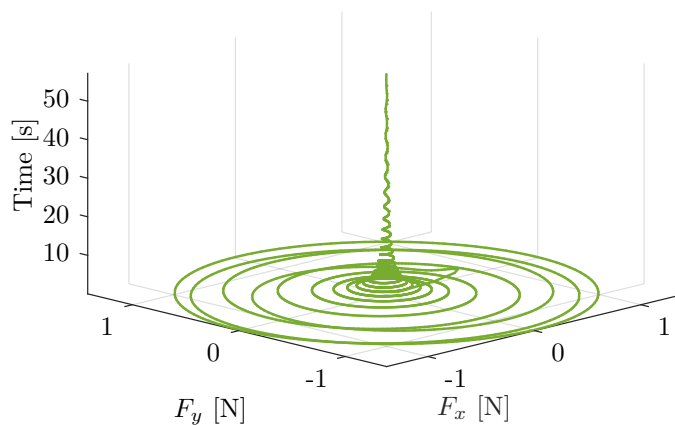


Figure 3.20: Resultant Sail-Plane Force from Unbalanced Tip Masses

3.8.3.2 Initial Boom Offset Discrepancies

It has been previously seen that, in the first moments of deployment, the in-plane boom offset angle can quickly grow. If the booms are not of perfectly matching length or one boom begins deployment with a slight initial extension, this boom may possess an offset angle while the rest do not. Case 1 of the passive deployment discussion will again be used for simulation with an initial non-zero boom offset angle on boom one.

In Case 1 of the passive deployment scenarios discussed in Section 3.6.1, the boom offset angle reached a magnitude of -12.3° when deployed 20 mm after 28 ms into the deployment procedure. This illustrates the initial rapid growth of the θ angle as the tip masses become unrestrained from their stowed position. Here an initial condition of $\theta_1 = -12.3^\circ$ will be induced while all others are to remain as they were.

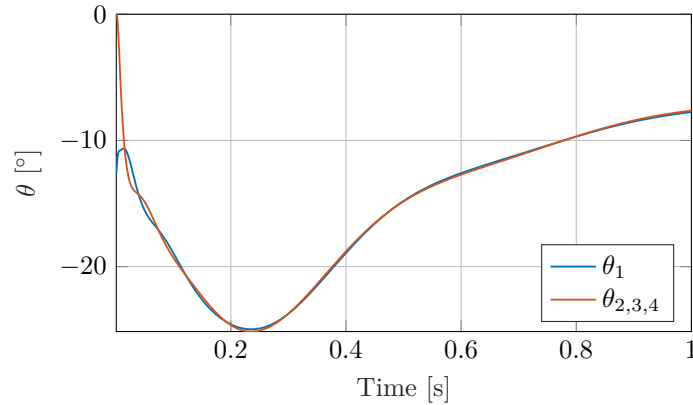


Figure 3.21: Initial Unbalanced In-Plane Boom Offset Angle: In-Plane Boom Angle

The general behaviour of the in-plane offset angle remains as has been previously seen with one exception; where the boom angles matched in both phase and, almost perfectly, in magnitude during deployment before, they now are initialised out of phase as seen in Figure 3.21. This recovers over a few oscillatory periods where the phase difference decreases while the magnitude differs more than has been previously witnessed. Once deployment has been completed the trend matches that discussed in the previous section with unequal tip masses.

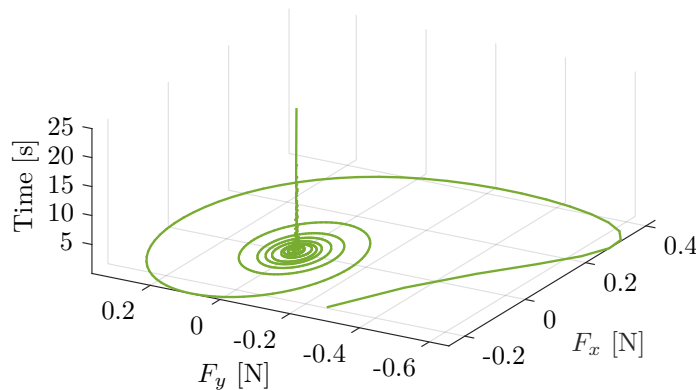


Figure 3.22: Initial Unbalanced In-Plane Boom Offset Angle: Resultant Sail-Plane Forces

The resultant force exerted on the satellite body is shown in Figure 3.22. It is of a smaller magnitude as in the previously discussed case. The recovery of the initial in-plane boom offset angle exerts a relatively large force in the sail-plane; once this angle has recovered to more closely match that of the other boom the imbalance is small and is quickly damped

out by the boom wire damping. It is thus shown that in-plane boom angle discrepancies can induce out-of-plane angular oscillations of the spacecraft body.

3.8.3.3 Boom Winding Inconsistencies

The potential issues and challenges of achieving perfect winding of the booms on the pulley have been touched upon. When winding thin, yet long lengths of wire around a pulley, perfect winding will not occur and each length of boom will not lie identically within the discrete windings. The effective pulley radius, arrangement of the coiled layers or the spacing or tension of the windings may vary between booms. This can cause one boom to be deployed at a different length to another at a moment in time causing imbalances in the spacecraft.

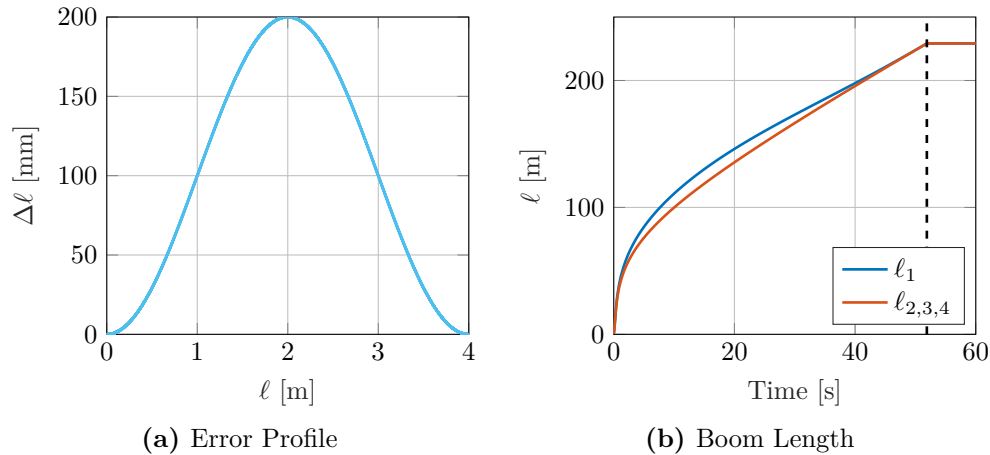


Figure 3.23: Boom Length with Error Profile

To reveal what may happen under conditions of irregular winding, an error in the length of boom one of $\Delta\ell$ is induced during the deployment procedure. It is assumed that the booms are all the same length, and that their initial and deployed lengths are equal. Instances may occur where the initial and/or final boom lengths differ but this is unlikely and can be easily detected before launch. A maximum error of 5% of the final boom length, is applied over the course of deployment based on the already deployed boom length as per the error profile in Figure 3.23a. This adds zero error to ℓ_1 at the start and end of deployment and a maximum of 200 mm when deployment is half way complete at 2 m. The effect that this has on the boom lengths during the course of deployment is seen in Figure 3.23b.

This induces some interesting behaviour. As there is no imbalance at the commencement of deployment there is no initial sudden state change leading to a angular rotational oscillation of the the body around the spacecraft centre of mass. However as the error initially grows the effect becomes more pronounced. Conversely as the error diminishes during the later portion of deployment, so does the magnitude thereof as can be seen in Figure 3.24. These forces in the sail plane induce torques on the satellite body.

The in-plane boom offset angle, presented in Figure 3.25, shows behaviour different to any trend as seen before. Initially θ grows as per the norm however the more rapidly increasing length of boom one allows θ_1 to grow to a greater degree. While deployment is under-way the boom angles begin to recover. The combined influence of the changing boom length and additional centrifugal force induced by the spacecraft body angular oscillatory motion allows θ_1 to lead the bus with a positive offset angle, a rather unintuitive resultant behaviour

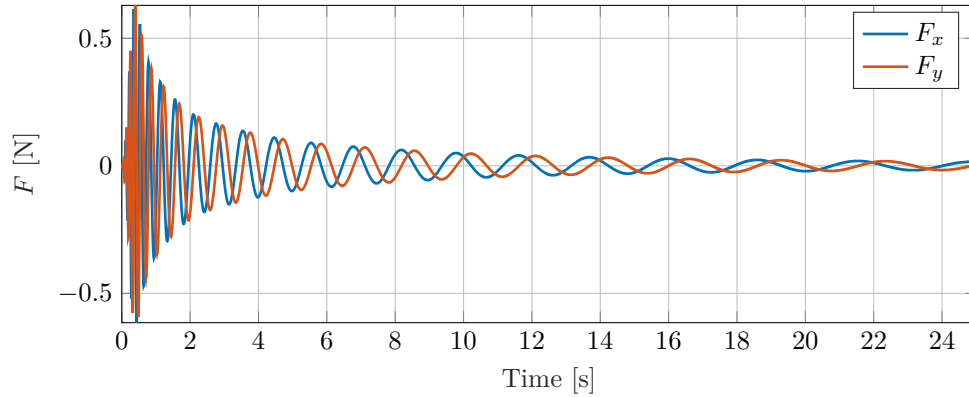


Figure 3.24: Inconsistent Boom Winding Effects: Resultant Sail-Plane Forces

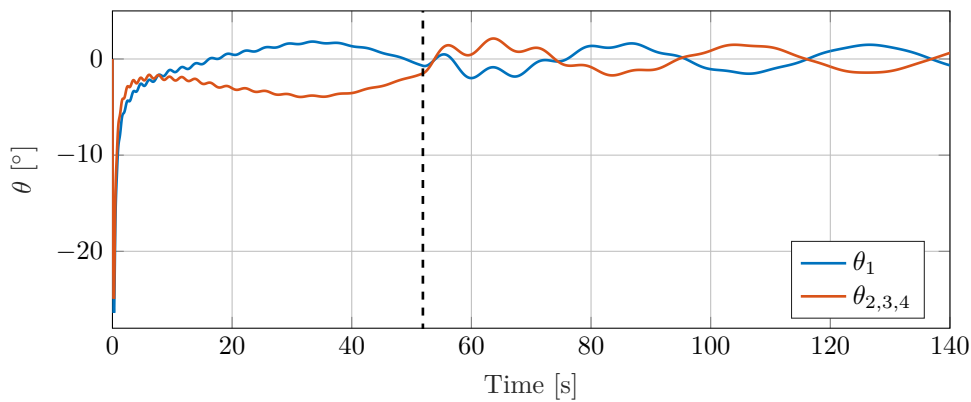


Figure 3.25: Inconsistent Boom Winding Effects: In-Plane Boom Angle

while not unsurprising. As the booms are already counter acting one another's energies, the oscillations experienced at deployment completion are significantly calmer, with almost none of the major deviations seen in previous cases. The onset of the steady, out of phase oscillations occurs sooner after deployment completion and are induced by the satellites gyrating motion in space.

3.9 Influences of Pulley Design

Under passive boom deployment, the deployment is driven by the application of torque to the pulley by centrifugal force. This torque is then counteracted by the rotational pulley damping which determines the rate at which deployment takes place. Negating control over the bus spin rate, the primary means by which the deployment rate and thus deployment dynamics may be determined at a hardware level, are by the pulley hub base radius, a_p , and the rotational damping of the pulley, b_p .

Altering either of these values in the design has significant effects on the deployment dynamics as the pulley torque which defines the deployment, Equation 3.5.5, is dependent on these physical parameters. Changes in the pulley radius would also affect the moment of inertia of the pulley, but this effect is negated in order to focus primarily on the radius, and to avoid introducing additional variables.

To examine how these crucial design choices influence how deployment proceeds, a simulation regime was undertaken. The dynamics of deployment are chaotic and highly sensitive to system parameters and initial conditions, and thus some fixed variables must be enforced. The system parameters that were previously used for the simulation of the passive deployment cases will be used under the control strategy of case 4, where the bus spin rate was maintained constant at $\dot{\beta} = 3$ rps. This eliminates the undesired and not easily predictable influences of the other deployment control strategies investigated, which may not be constantly in force.

The range of pulley radii to be tested was determined by the physical constraints of a CubeSat. Within the 100 mm width of a CubeSat a pulley diameter of greater than 80 mm is unlikely. Pulley radii in the range of 5 mm to 40 mm were this investigated. Pulley damping is more challenging to place an upper limit on, and it is known that no damping will result in unsuccessful deployment. A pulley damping range of 1 mN · m · s/rad to 250 mN · m · s/rad was investigated in order to demonstrate the trend.

The influences of selecting different pulley radii and rotational damping values on key parameters are presented. The effects on the maximum in-plane boom angle, Figure 3.26a, and the deployment time, Figure 3.26b, are provided. As would be expected, a larger pulley radius results in more rapid deployment, as a greater torque is exerted on the pulley for the same centrifugal force. This in turn results in a larger in-plane boom offset angle, up to the point where the angle grows to an unacceptable degree and deployment fails; this is represented by the lack of data points in the resulting plots. A decrease in the pulley hub radius has a parabolic increasing effect on the deployment time of the booms, while an increased pulley damping has a more linear effect on the deployment time. In the design of a deployment mechanism it may be likely that the pulley hub radius chosen would depend on not the deployment dynamics desired, but rather on physical size constraints of components; the damping would thus be the main means by which the deployment rate and other dynamics of the system would be controlled.

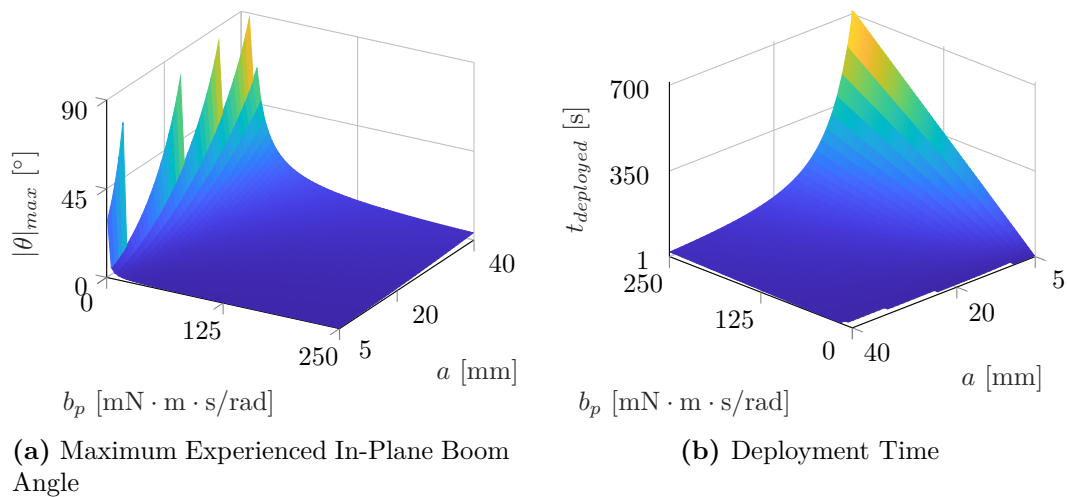


Figure 3.26: Effects of Pulley Design Decisions

3.10 Chapter Summary

A conceptual model of a satellite equipped with a solar sail has been defined. The means by which this sailcraft may deploy its sail have been investigated by the development of dynamic models which describe the behaviour of the satellite during- and post-deployment. It was readily shown that the free deployment of a spinning solar sail is not feasible and that some means of controlling the deployment, be it active or passive, is required. A number of deployment strategies were then investigated through simulation and the results thereof discussed.

At the commencement of boom deployment there is a rapid growth in the boom in-plane offset angle, which is strongly dependent on the deployment rate. This boom offset angle can grow to be significant and result in large displacements of the boom tip mass at large boom lengths. This results in a significant fraction of the total system energy being contained within the deploying boom element, rather than the spacecraft body. At deployment completion, the recovery to an equilibrium state results in potentially chaotic oscillations of not only the boom offset angle but also the bus spin rate. This poses a risk to the satellite bus and the stability of the solar sail.

In the passive deployment cases investigated the deployment rate was not constant throughout the deployment process, resulting in changes and oscillations in the boom angle. It was shown that these oscillations may not only occur at the end of the deployment process but during it as well. The effects thereof may cause instability and uncertainty in the state of the sail. The initial rapid growth of the boom in-plane offset angle promotes the use of boom lengths which are greater than required to support the sail surface area. The additional boom length can allow these more extreme dynamics, in the initial moments of deployment, to be absorbed by the boom itself and not pose a threat to the sail membrane. The additional length may also assist in the sail deployment as a greater centrifugal force can be produced before the sail is pulled from a stowed state.

Emphasis was placed on how the winding of the booms upon the pulley may influence the deployment dynamics. As the booms unwind from the pulley the effective radius of the pulley, and thus the torque applied to the pulley by the centrifugal force, will decrease. This has a noticeable effect on the deployment rate. The arguments that can be made based on the simulation results show that the effects of stowing large lengths of boom wire on small pulleys cannot be ignored, especially as the size of sails increase, in the modelling of these and similar problems.

In the case of active deployment, where the deployment rate is directly controlled, the torque which needs to be applied to ensure stable boom deployment on a spin stabilised spacecraft is counter to the positive pulley rotation. The actuator used for deployment needs to be capable of restraining the deployment of the booms rather than driving it onwards.

While the general trends and dynamics of an ideal deployment can be easily investigated by modelling a single sail boom, any practical effects of a non-ideal deployment require the modelling of multiple booms. Several possible unbalanced deployment cases were investigated and it was shown that an unbalanced sail deployment may effect the stability of the spacecraft by inducing angular oscillations of the spacecraft around the centre of mass in multiple axes, which may need to be corrected for. The magnitude and effect they may have on the satellite differs per instance and would be highly unpredictable in practice. These additional induced out-of-plane dynamics would too have effects on the behaviour and performance of the sail and its deployment.

Chapter 4

Experimental Deployment Design

An experimental deployment mechanism needs to be developed in order to test and confirm some of the behaviours seen in simulation. This process also begins the design path to a flight-worthy deployment mechanism. In this chapter the design of the various components of such an experiment are discussed along with the decisions and compromises which had to be made. The experimental layout, procedure and strategy are also discussed.

4.1 Specifications and Requirements

An experimental test platform needed to be designed and constructed such that it could be used to test design theories and decisions, as well as validate the mathematical models devised. This model was designed specifically with experimentation purposes in mind, and thus alterations and compromises were made to the design in order to facilitate this; these would not necessarily be applicable to the more flight-focused design. The test platform was made to test the passive deployment case exclusively and use rotary dampers to retard the deployment rate of the booms.

The experimental platform was required to fulfil the following criteria:

1. Be controlled through the use of a Direct Current (DC) motor and simple serial commands.
2. Allow adaptability of the damping force applied to the boom deployment.
3. Adhere to the dimensional constraints of a CubeSat as far as reasonably possible; excluding sensing and mounting hardware.
4. Be mechanically simple to facilitate ease of manufacture.
5. Be as lightweight as reasonably possible.
6. Include as many design features of a flight-focused model as feasible, provided that no unjustifiable compromises are made on other design criteria.
7. Gather data on:
 - The bus rotation angle and rate.
 - Deployed boom length.
 - Spin controller state and behaviour.
 - Driving motor power draw.

The broad aim was to maintain simplicity wherever possible in the design. This was intended to allow greater ease of manufacture as well as provide room for adjustment if the need arose. The most notable aspects of the experiment design will be discussed here.

4.2 Experimental Architecture

The experiment and accompanying hardware was required to fulfil the requirement specified. The initial and most apparent design constraint of this is that there is both a mechanical as well as informational rotary connection in the system. There are aspects which needed to be spinning and other which are not. This presents some design complication as far as the mechanics and sensing is concerned.

The major components of the system are thus divided into two distinct criteria: a spinning and a stationary platform. The spinning portion of the experiment will be the focus as far as the actual deployment is concerned. This section will mainly comprise of the main mechanical assembly of the deployment mechanism as well as any sensing hardware required on that platform. The experimental deployment mechanism comprises of the spinning assembly which contains the booms, the pulley around which they are stowed, the rotary dampers which retard the deployment rate, and any other supporting components which may be required. The stationary components would involve the securing point for the experiment, the base station to issue and receive commands, and the spin driving actuator as well as its accompanying electrical and mechanical hardware. This separation is illustrated in Figure 4.1.

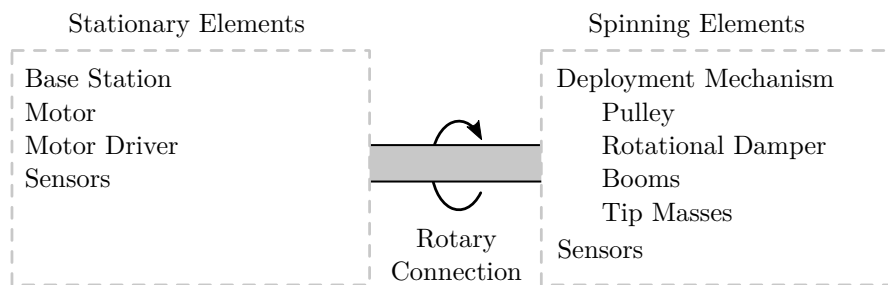


Figure 4.1: Separation of Spinning and Stationary Experimental Aspects.

4.3 Sensors and Data Acquisition

In order to gather the information required for measuring the system's behaviour, a suite of sensors was required for Data Acquisition (DAQ) purposes. Information is to be gathered from both the point of view of the spinning and non-spinning platforms; two distinct sensory packages are required where from the information gathered can be combined for post-processing. The design and implementation of these DAQ units are discussed here.

4.3.1 Spinning Sensors

The spinning sensor suite not only required the ability to record data, but also to transmit this data across a rotating joint. The sensing and data transmission design aspects of the spinning DAQ unit with possible solutions as well as the final decisions therefore are separately addressed.

4.3.1.1 Data Transfer

A degree of additional complication is added to the design of the spinning DAQ unit as the experimental platform is rotating, necessitating some means of circumventing the dynamic connection. Several options exist to achieve this; the primary three considered were a slip ring, wireless communication and direct to memory logging from which the information could later be retrieved. All three of these methods have advantages and disadvantages.

A slip ring was initially seen as a very attractive option as it would allow the information to be gathered and transferred in real time, potentially eliminate the need for a second micro-controller, and allow power to be provided to the spinning sensors without the need for an on-board battery. However, it quickly became apparent that a slip-ring would not meet the requirements of the experiment, a major factor being that a slip ring with a sufficient number of channels proved challenging to procure in addition to being a physically very large component. This caused it to become a dominating feature of the mechanical design, and the additional mass, complexity and rotational friction which would have been introduced by using this method was undesirable. There was also concern that the slip rings may induce signal noise and data loss, another undesired trait.

Wireless communication would have proved to be the most convenient option. This would provide the same benefits as the slip-ring in terms of real time telemetry downloads and was the path initially selected. Hardware development boards were investigated which offered the options of both Bluetooth Low Energy (BLE) and Wi-Fi communication. The supported BLE communication protocol proved overly bloated in complexity for this purpose and was discarded as an option. Communication of the sensor data over Wi-Fi was achieved but the transfer speed of the communication proved to be a bottleneck. In addition the power requirements of the development board when transmitting data proved inconvenient as a large battery would be required adding significant mass to the spinning platform.

The final option considered and the one used for DAQ was an on-board memory card to store the data gathered, from which it would be retrieved upon completion of an experiment. This did have the distinct disadvantage of not allowing in-situ access to the gathered information, but was the simplest solution of the three considered. Additional benefits of this method included that the solution required a small amount of power and so smaller battery could be utilised, and the logging of the data to an on-memory device provides greater data security in that it vastly reduces the risk of lost telemetry.

4.3.1.2 Sensing

Two rotary encoders are required on the spinning platform: one for the mechanisms rotation and one for the pulley rotation within the mechanism.

To capture the rotation of the pulley a magnetic rotary encoder, specifically AS5040 from Austria Micro Systems [72], was used. A magnetic encoder allowed a minimum of interference with the pulley's rotations and assured no additional friction was induced. The encoder itself was mounted to the DAQ stack while the magnet was mounted to an extension of the pulley shaft which protruded out of the deployment mechanism. The component layout of the spinning electronic hardware is illustrated in Figure 4.2.

An encoder to measure the mechanism rotation was included on both the spinning and stationary DAQ units. The spin side encoder consisted of a quadrature optical slit disc encoder with A and B outputs. Only a single output was used however and was directly connected as an external clock input to record pulses output by the encoder channel. This effectively quartered the resolution and resulted in a loss of direction information. These decisions, coupled with the fact that an already very low resolution slit disc was used, led to a very low resultant encoder sensing resolution. This encoder however was not used to gather data on the deployment, but rather only to synchronise the information from the two

distinct DAQ units, as the time at which spin commenced could be easily detected and the time offset calculated during post-processing analysis of the data. A high resolution encoder here would not have justifiably benefited the experiment as only the first few readings are required and the rest not.

A simple button is used to start and end the data capture for each experiment and lights indicate the recording and deploying status during tests.

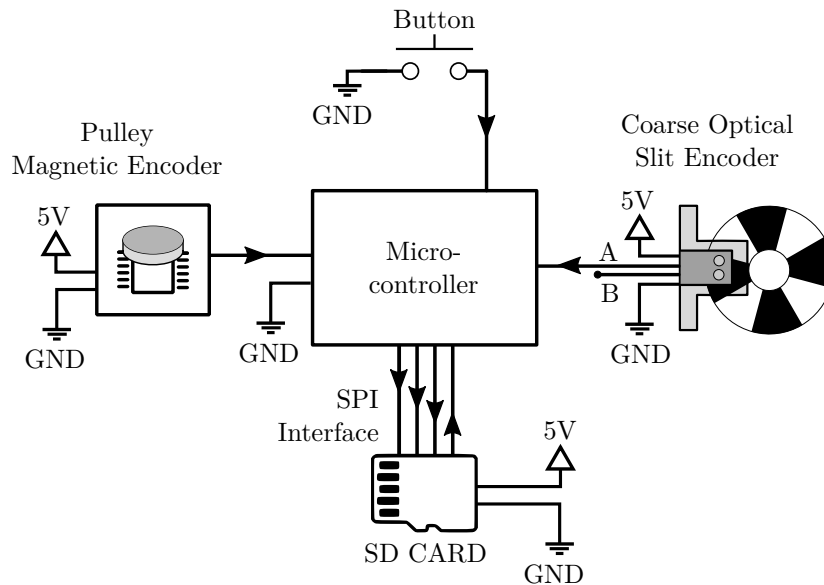


Figure 4.2: Spinning Sensing Hardware

Methods of actively measuring the boom in-plane offset angle were investigated. Methods considered included camera based measurement, strain gauges and direct measurement through an encoder or potentiometer. Unfortunately all these methods were deemed too impractical, or too intrusive to the dynamics, and would, at best, affect the results and, at worst, eliminate the in-plane boom offset angle. The decision was thus made to forgo this aspect of measurement for the purposes of this experiment.

4.3.2 Stationary Sensors and Drivers

The stationary package of sensors and drivers is focused around tracking the angle of rotation of the deployment mechanism, controlling the rate of spin based on input commands, and relaying the captured information to the base station computer through a USB serial connection. A layout diagram of the various components of the stationary DAQ is provided in Figure 4.3.

Here again a quadrature optical slit disc encoder with A and B outputs was used to measure the bus rotation. This encoder had a high resolution and was the primary one used for the data analysis. The encoder output was again coupled as an external clock input, however, a loss of accuracy on this encoder was not acceptable. Had the same method been used as on the spinning DAQ stack, the encoder resolution would have been a quarter of what the slit disc supported. The resolution is halved once by the use of only one output signal and halved again by the detection of only rising edges. To counteract this the A and B outputs of the encoder are passed through an XOR logic gate to effectively combine the signals and

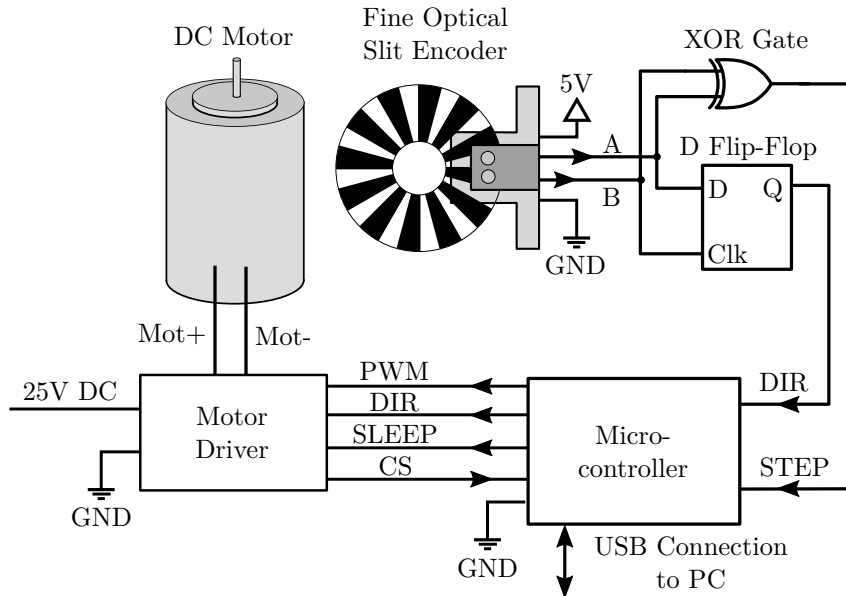


Figure 4.3: Stationary Sensing and Control Hardware

recover the resolution lost by only being able to use only a single input signal on the micro-controller. To regain the ability to detect the direction of the spinning bus the A and B signals are also passed through a D flip-flop gate. This changes state depending on the phase difference of the two output signals, with the one signal used as a clock input to the flip-flop and the other as the latching input. Practically, no changes in the direction of rotation would be experienced during experimentation, but the ability to detect it was incorporated for completeness. The output signals of the encoder and how they were conditioned by the logic gates is demonstrated in Figure 4.4.

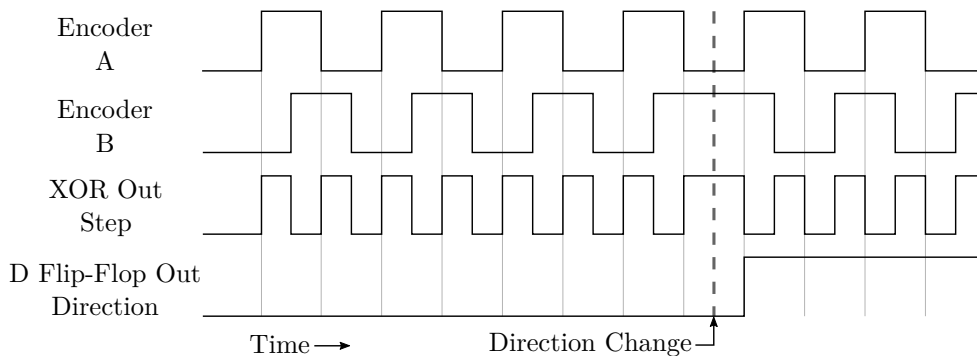


Figure 4.4: Encoder Output Logic Signal Conditioning

In order to drive the spin of the deployment mechanism a DC motor and driver was used. As the deployment experiments may be subjected to a constant spin rate for the duration of the deployment process, the motor was required to maintain this spin in spite of the great increase in the inertia of the driven load. A high current motor driver [73] was used to ensure sufficient power delivery. The motor driver used had a built in current sensing circuit, and thus the current consumed by the motor could be recorded. A simple DC motor

without gearing was used - had a motor with gearing been used, sufficient torque to achieve the required spin rates throughout deployment would have been more easily maintained. The additional friction and damping within the gearbox would, however, have suppressed the oscillations in the angular rate which may occur, and some of the dynamics would have been lost.

The micro-controller on the stationary DAQ unit serves to receive the data gathered by the stationary sensors as well as to control the driving motor. Information is sent over a USB connection to the base station computer where it is recorded. Commands to start and stop recording, and to set spin rates are received and acted upon. The micro-controller hosts the spin controller which manages the spin rate of the spinning mechanism based on the input commands received. The spin controller consists of a simple Proportional, Integral, Derivative (PID) controller which outputs a Pulse Width Modulation (PWM) signal to the motor driver based on a set-point spin rate input and the measured bus spin rate obtained by numerically differentiating the angular change measured by the encoder. The spin controller does not enforce adherence to decreases in spin rate set-point. Due to the high system moment of inertia this would cause significant current reversals in the motor which can cause damage to components and produce significant boom oscillations. The system is instead allowed to slow down freely under the influences of friction and atmospheric damping.

The stationary DAQ unit was connected to a base station computer which performed the functions of both receiving and recording the experimental data at a rate of 100 Hz, and issuing commands to the motor controller at a rate of 10 Hz.

4.4 Experimental Deployment Mechanism Design

The mechanical aspect of the experimental deployment mechanism was designed to meet the specifications set out to achieve a passive deployment of the booms. A mechanism which could easily be manufactured, and was capable of deploying four booms passively by the use of a rotationally damped pulley was to be designed. Aspects of the experimental deployment mechanism are here discussed and the design presented in Figure 4.5.

4.4.1 Pulley Rotational Damping

The use of rotary dampers (Figure 4.6) to retard the rate of deployment was used as the starting point around which the mechanism would be designed. As the damping needed to be applied to the rotation of the pulley, the torque needed to be transferred from the damper to the pulley. This was to be achieved through the use of a gearing system. A large gear was fitted to the central pulley and provision was made for four dampers to surround the pulley. Each damper could be fitted with a pinion gear meshing with the central gear to transfer torques. In order to allow for varied experimentation parameters the rotational damping of the pulley was to be adjustable. To achieve this the dampers were mounted on slotted connections allowing the radial position of the dampers to be adjusted and differing gear ratios to be fitted by changing the damper pinion gear. This allowed a variety of gear combinations and damping forces to be applied.

These dampers operate on the principle of viscous damping as they contain an inert fluid that acts against the movement of surfaces within the damper body. They are available as Commercial Off The Shelf (COTS) components in a variety of configurations and sizes, and can be made to offer damping in only one specific direction, or both directions of rotation [74, p. 215]. These rotary dampers are similar to the ones used by Tada *et al.* [49] in the deployment of a drag sail with semi-rigid booms. The resilience of these dampers when subjected to the conditions in space remains to be fully tested. Of primary concern is the fluid bearing cavity within the damper under vacuum and how temperature fluctuations will affect the damping properties. Rotary dampers which use friction, instead of fluid, damping

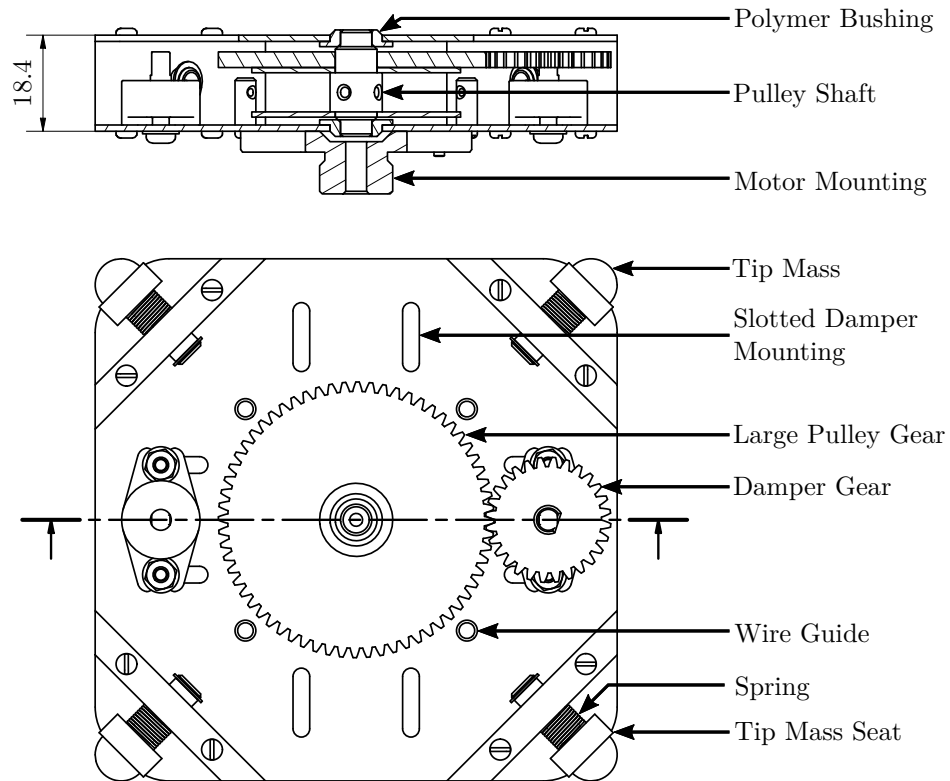


Figure 4.5: Experimental Deployment Mechanism

are available [74, p. 223] which may prove more hardy and provide better tolerance to temperature fluctuations.

It was desirable that the experimental deployment take place over a long period of time and thus a damper was chosen according to this. The FRT-C2-201 damper from ACE [74, p. 222] was used, which can provide approximately $0.5 \text{ N} \cdot \text{cm}$ of damping torque at low rotational rates. The slow deployment which could be offered by this damper provided additional time to gather information on the deployment as well as to test deployment controllers and detection methods.



Figure 4.6: Rotary Dampers, [74, p. 215, 222].

4.4.2 Pulley

The pulley around which the booms were wound when stowed was designed in as simple a manner as possible for speed and ease of manufacture. The pulley consisted of a central shaft, two flanges and a gear.

The volume within which the booms were to wind was constrained by two thin sheet metal flanges. The compromise was made, in the name of manufacturability, to have a single section of the pulley around which all four booms would wind. This greatly reduced the complexity of the design as only two flanges were required instead of five. A compromise was made in that the winding of the booms was more prone to inconsistencies and errors, further discussed in Section 6.1. As mentioned, a gear was mounted to the shaft, through which the damping force would be transferred to the pulley. Finally, the shaft was supported on either side by polymer bushings to facilitate smooth rotation within the mechanism.

A threaded hole in the upper end of the shaft allowed a small magnet to be seated on a pedestal and adjusted in height, for the purpose of measuring the angular rotation of the pulley within the deployment mechanism, using a magnetic encoder. The magnet and its mounting protrudes from the top of the deployment mechanism where it can easily be accessed, and in such a way that it was not necessary to distort the deployment mechanism in shape or size to accommodate it.

4.4.3 Boom Wire Path and Tip Mass Seating

The boom is secured to the pulley through holes drilled radially through the shaft. The boom path then proceeds through a small wire guide that acts to ensure winding proceeds as evenly as possible, whereafter it passes through the corner tip mass seating assembly and finally attaches to the 20 g tip mass.

The corner assembly consists of three primary parts. An aluminium block acts to provide structural support to the mechanism as a whole by securing and properly spacing the top and bottom plates of the assembly. The tip mass seat is inserted through this block with a loose sliding fit. The tip mass seat has a spherically concave depression which securely seats it when stowed. The boom passes through the centre of this piece which is made of a low friction polymer to allow free sliding motion within the aluminium corner mounting block and of the boom wire. The use of a soft polymer prevents any damage to the boom wire from sharp edges or burrs which may be present on a metal equivalent. The seat is spring loaded such that any small discrepancies, up to about 4 mm, in the length or winding of the booms can be absorbed and booms do not begin deployment unsecured. The spring used is weak and serves only to adsorb the length discrepancies and not provide a pre-load for boom deployment.

For the boom wire itself, braided PET¹ line² was used. This offers a very thin boom wire with high tensile strength and minimal to no longitudinal deformation under load. The specific line used had a diameter of only 0.2 mm and load capacity of 9.1 kg. This strength is sufficient to allow a rotation rate of 10.6 rps at a deployed length of 1 m. This is more than sufficient to meet the needs of the experiment. The use of this thin, lightweight material for the boom wire allows it to more closely represent the theoretical assumptions made of a rigid, massless boom without any spring properties.

¹Polyethylene terephthalate; a polyester thermoplastic polymer used in the manufacture of containers and fibres, trade names include Terylene, Lavsan and Dacron.

²Commonly available and known as braided fishing line.

4.4.4 Experimental Deployment Specifications

The specifications of the designed deployment mechanism and its subcomponents are provided in Table 4.1. These are the necessary values required for analysis of the system behaviour and for comparisons to future design revisions.

Table 4.1: Experimental Deployment Mechanism Specifications

Parameter	Symbol	Value	Unit
Mechanism mass	m_b	165.25	g
Mechanism inertia	I_b	281.16	$\text{mg} \cdot \text{m}^2$
Spinning DAQ stack mass		87.53	g
DC motor rotor inertia		5.22	$\text{mg} \cdot \text{m}^2$
Total spinning mass		252.78	g
Total spinning inertia		311.55	$\text{mg} \cdot \text{m}^2$
Mechanism dimensions	LxWxH	100x100x18.4	mm
Damping gear ratio		32/64	
Tip mass	m	20	g
Tip mass diameter		15	mm
Boom length	ℓ_f	1.016	m
Boom exit radius	r	58.86	mm
Pulley mass	m_p	15	g
Pulley inertia	I_p	3.42	$\text{mg} \cdot \text{m}^2$
Pulley base radius	a_p	5.0	mm
Pulley fully wound radius	a_{eff}	6.7	mm
Pulley width	w	7.5	mm
Boom wire diameter	h	0.2	mm
Coarse encoder resolution		360	step/rev
Fine encoder resolution		4320	step/rev
Pulley encoder resolution		1024	step/rev
Sample rate		100	Hz

It can be seen that the spinning DAQ stack contributes a third of the spinning mass. This increased mass increases the moment of inertia of the spinning mechanism and may lead to more subdued effects on the angular bus rate than would otherwise have been present. The mechanism conforms to the size requirements of the CubeSat standard by having a length and width of 100 mm and a height of 18.7 mm excluding the sensor and mounting hardware. The mechanism is thus $\sim 0.2U$ in size. The height of the mechanism was most strongly influenced by the size of the rotary dampers as well as, to a lesser extent, by the size of the tip masses.

The size of the boom stowage volume on the pulley was made as wide as the mechanism's height would allow. This allowed greater ease of assembly and boom attachment. The experiment was limited to booms of 1 m in length. The boom length is limited by what is achievable under the conditions of gravity and atmospheric influences such as aerodynamic drag. While the detrimental effects of an atmosphere on the experiment could be circumvented by the use of a vacuum chamber, even the deployment of relatively short boom lengths would require an uncommonly large vacuum chamber. The effects of gravity cannot be practically circumvented during terrestrial tests as no gravity-free environment exists, and parabolic flights do not offer the volume nor time durations required. Common methods of gravity offloading, as used with semi-rigid boom deployment tests, cannot be used due

to the flexible and spinning nature of wire boom solar sail deployment mechanisms. These reasons also apply, with greater prominence, to any possible inclusion of a sail membrane in a spinning deployment test.

4.5 Experimental Layout

The designed and manufactured parts of the experiment are combined into the experimental component stack, as in Figure 4.7, which forms the central hardware aspect of the experiments. The base stand is securely fastened to an elevated and weighted platform. The elevation is necessary to allow lower angular rates to be achieved without the booms colliding with the surface upon which the experiment takes place due gravity, while the added weight dampens out any small vibrations which may be induced by imbalances in the spinning system.

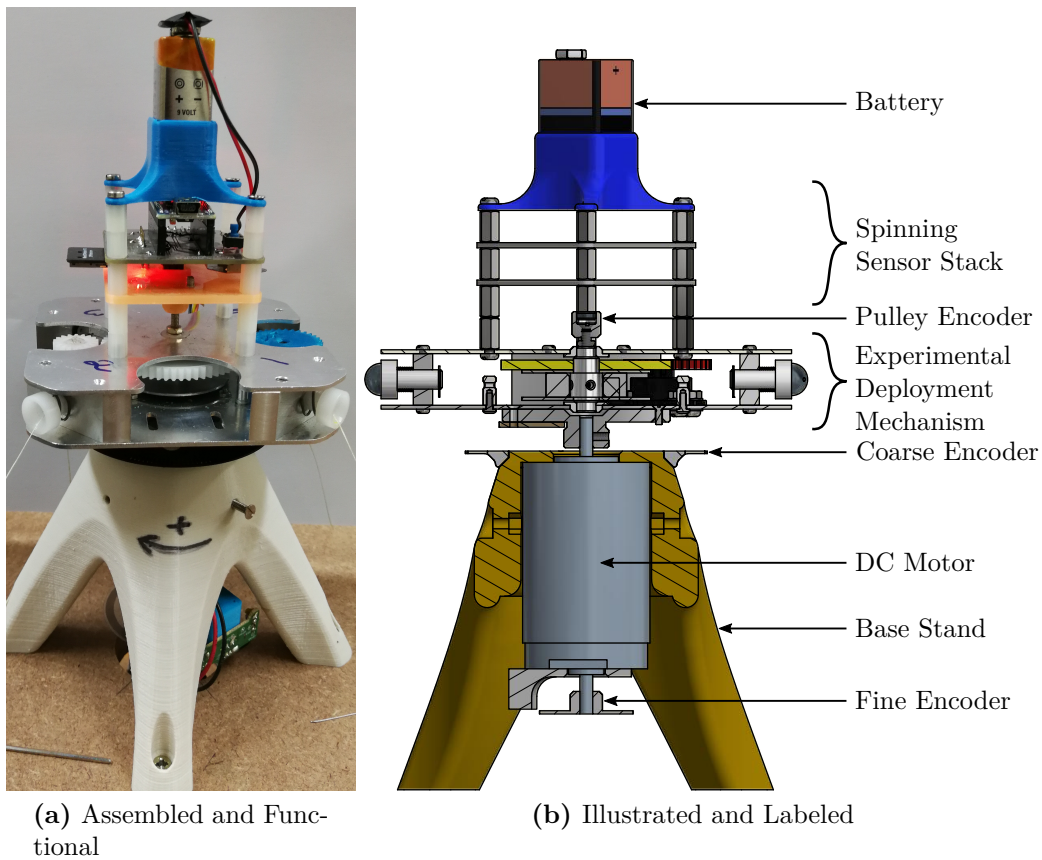


Figure 4.7: Experimental Component Stack

The driving motor is secured to the base stand and the experimental deployment mechanism is rigidly coupled directly to the motor shaft. The coarse optical slit encoder ring is incorporated into the base stand. The spinning DAQ stack is fixed to the deployment mechanism with its mass centred over the axis of rotation.

The experimental component stack, on the elevated base, is placed in the centre of a large table. The DC motor driver is connected to a 25 V, 6 A power supply and the stationary DAQ to a base station computer through a USB serial connection.

4.6 Experimental Procedure

The procedure to conduct the experiments proceeds as follows:

1. The booms are wound up into the mechanism.
2. Power is supplied to the motor driver and spinning DAQ stack.
3. The experiment is begun by initiating data capture on the spinning DAQ through pressing the button and on the base station by sending a start command.
4. A series of commands are then sent to the motor controller indicating the spin rate of the mechanism.
5. The spin rate is controlled according to the conditions to be tested, be it constant speed, manual control or an automatic controller.
6. The mechanism is allowed to continue steady spinning after deployment completion to allow any potential oscillations to settle if time allows.
7. Control of the mechanism spin is ceased and recording is terminated once the system has come to a standstill.

4.6.1 Boom Winding

The resetting of the booms during experimentation proved to be a challenge as the inconsistencies in windings were more prominent than anticipated. This is discussed in more detail in Section 6.1 but in short, it was found that a repeatable and consistent method of boom winding was needed. A simplistic method was thus developed to wind the booms at as constant a tension and speed as feasible. This procedure is illustrated in Figure 4.8.

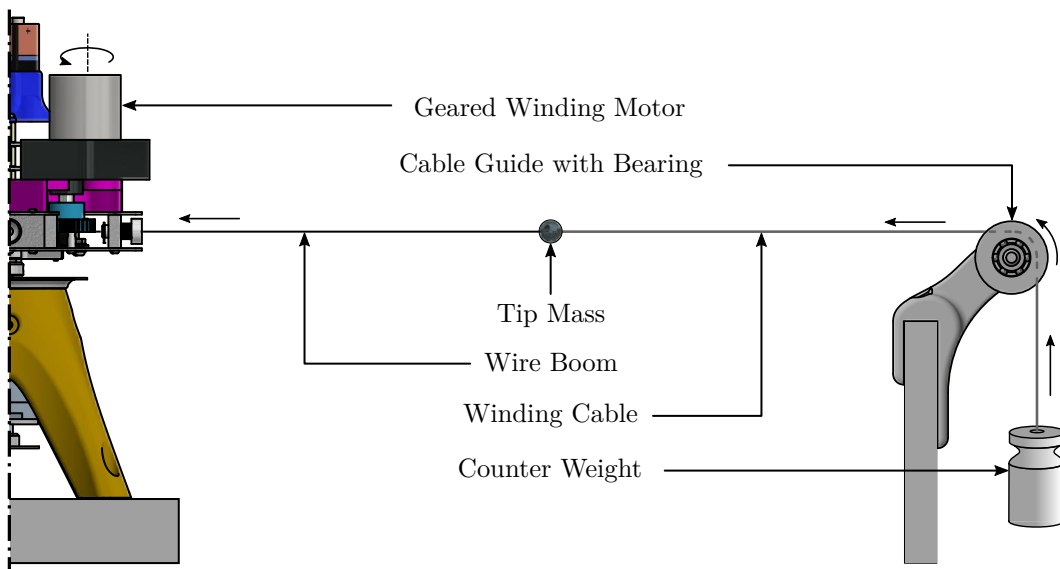


Figure 4.8: Winding Procedure Layout

In order to maintain a constant tension on the booms masses of 400 g were attached to each boom and allowed to hang freely. The cord attaching the boom to the mass was passed over

a bearing to minimise friction. To ensure that a constant rate of winding was maintained a geared DC motor operating at a constant voltage was connected to the pulley gear which would retract the booms at an average rate of 8.25 mm/s. The damper and gearing was left engaged during winding to further smooth out the pulley rotational rate and thus the winding rate. This winding procedure proved effective in consistently winding the booms in a controlled manner.

4.7 Chapter Summary

An experimental deployment mechanism was designed which is driven by a brushed DC motor and is capable of performing a passively damped boom deployment. The experimental mechanism is equipped with two distinct DAQ units. These units capture information, using a number of encoders, on the rotation of the mechanisms spin as well as the deployment of the booms. The hardware designed for experimental purposes comprises of several compromises and additions in order to make it suitable for testing purposes. These features would be omitted in a more flight-focused design.

The spin of the mechanism is controlled by a PWM driven DC motor and high current motor driver. The spin controller is a simple PID controller which accepts a set-point spin rate as an input. A simple yet reliable means by which the booms could be wound was devised to overcome the issues experienced regarding inconsistent winding. While not an ideal means of achieving even winding for large boom lengths, this satisfies the requirements of the experimental platform.

The multiple compromises and scale of the design of this experiment shows that the terrestrial testing and validation of large deployable space structures is extremely challenging. This especially applies to flexible structures and those that are spinning. If physical space is not limited, the negative effects of atmospheric resistance cannot easily be overcome. Even if experiments are conducted in a large vacuum chamber the effects of gravity then become the limiting factor and cannot be escaped. A full functional test of a large spinning solar sail with flexible booms is thus impossible on earth and in-orbit testing is the only realistic solution. Testing is thus limited to small scales with short booms and simplified deployment mechanisms, and simulation.

As the experimental mechanism, sensing and control methods and procedures have now been presented; the following chapter will address the conduction, results and analysis of the performance and behaviour of this system.

Chapter 5

Experimental Deployment Findings

As per the discussion in Chapter 4, experimentation was conducted on the deployment behaviour of the designed experimental deployment mechanism. Of the experiments conducted will be presented and discussed, including deployment with manually controlled bus rate and the conceptualisation of an algorithm to automatically detect and control the deployment process. Comment and analysis is provided which may be used to further develop deployment strategies.

5.1 Manual Control

Initial deployment experiments were conducted through manual control of the mechanism spin rate set-point. The spin rate was adjusted based on visual observations in order to gain insight into the behaviour of the physical device. This allowed some of the specifications, such as the static friction, to be determined as well as providing insight into how individual parameters, such as the spin controller output, change during the course of the deployment.

5.1.1 Pulley Static Friction

To find the static friction of the pulley, and thus the spin rate at which deployment would commence, a mass could simply have been attached to a boom end and allowed to freely hang. Mass could have been added until the pulley began to rotate. This method of finding the static friction in the mechanism would have been simple and effective but required a specific set up and additional hardware. Instead the spin rate to initiate deployment was found in-situ during tests with manual spin rate control. The spin rate of the bus was incrementally increased until the initiation of deployment was observed. The initial deployment rate of the booms is very low for the first few centimetres of boom as the radius driving the centrifugal force is small. As this radius increases so does the deployment rate. To ensure that the initial spin rate required for deployment was not overestimated, the process of finding the appropriate spin was conducted gradually to allow time for the deployment to become apparent to visual observation.

One such test can be seen in Figure 5.1 which shows the incremental, stepped increases in the spin rate set-point with an initial ramp input. The spin rate was increased by 0.1 rps every 120 s until deployment was observed. The spin rate determined through visual observation was confirmed when the spinning sensor data was incorporated in post-processing of the gathered data. In Figure 5.1 the start and end of deployment is indicated by the vertical black dashed lines. The spin rate required to initiate deployment was found to be 2.6 rps which equates to a friction force on the linear boom deployment of 1.61 N or a pulley friction torque of 10.78 mN · m. These figures account for boom winding inconsistencies and the increased effective pulley radius. The static friction found is high enough such that the

booms will not extend under the influence of gravity on the tip masses but it is low enough to show that a locking pin is indeed required.

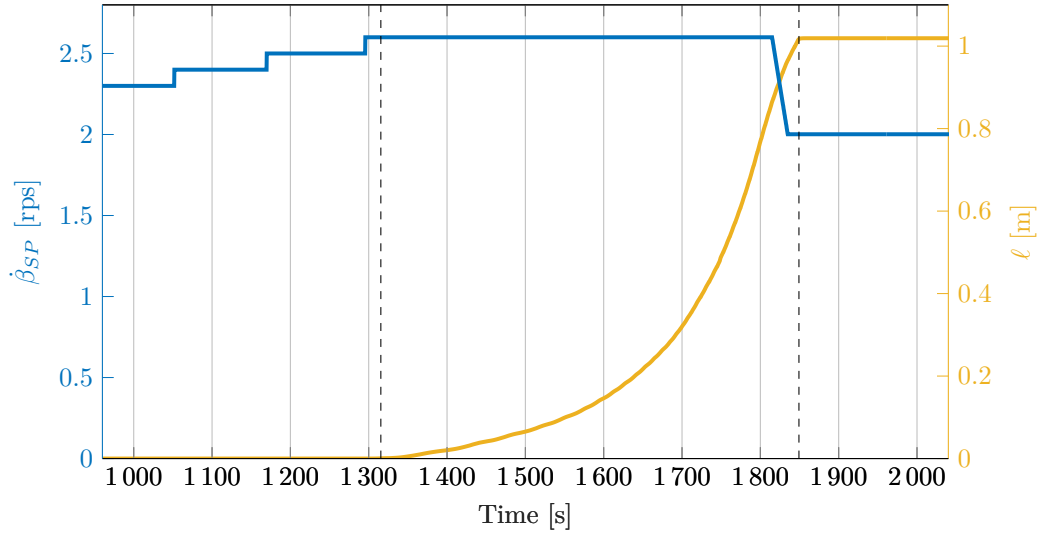


Figure 5.1: Determination of Pulley Static Friction

During the experimental regime there were several instances where the deployment mechanism required disassembly and re-assembly. It was found that the bus spin rate, and thus centrifugal force, required to initiate deployment was sensitive to this. The spin rate was seen to vary between 2.4 rps and as high as 3.1 rps in one case. This has been mostly attributed to friction between the gears, as well as deformation of the top and bottom plates which form the main structural components of the experimental deployment mechanism. The plates are supported at the corners only and made of thin aluminium sheeting; the polymer shaft bushings fit into the centre of these plates. Deformation of the plates varies the axial clamping force on the pulley shaft, which changes the static friction present in the system. This was mitigated by careful reassembly of the mechanism and manual correctional adjustment when necessary. The spin rate required to initiate deployment was maintained at approximately 2.6 rps as far as practically possible.

5.1.2 Pulley Constants

Using this same data set the pulley rotational damping and friction can be estimated using a least squares estimation line fit. The data points during the deployment phase where the bus rate remained constant were used. Using the calculation for the sum of the pulley torques, as derived in Equation 3.5.6 on page 37, in the form

$$F_c a_{eff} - I_p \ddot{\phi} = b_p \dot{\phi} + T_{fk} \quad (5.1.1)$$

allows the pulley rotational damping and friction to be estimated with a straight line fit. This fit can be seen in Figure 5.2. The pulley friction torque is estimated as $11.3 \text{ mN} \cdot \text{m}$ and the rotational pulley damping is $92.5 \text{ mN} \cdot \text{m} \cdot \text{s/rad}$. The periodic variations which can be seen in the scatter plot data of Figure 5.2 are due to the non-ideal off-centre mounting of the pulley encoder relative to the magnet.

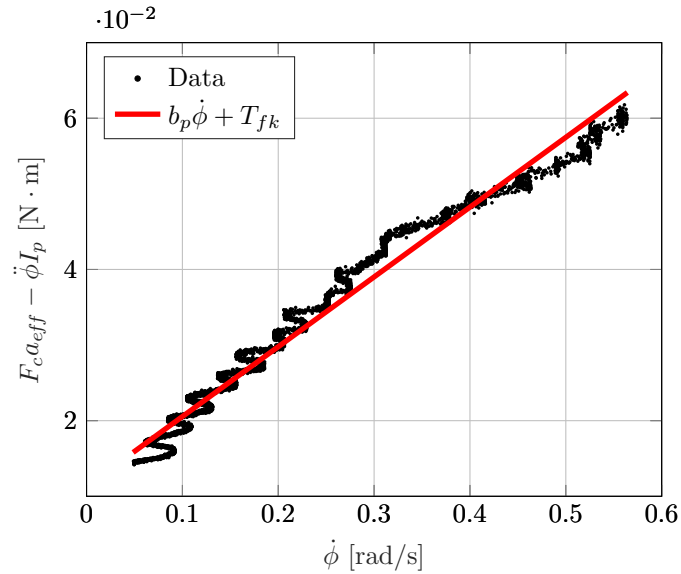


Figure 5.2: Pulley Rotational Constants Line Fit

5.1.3 Deployment Behaviour

The deployed boom length during a test with a manually controlled bus rate is presented in Figure 5.3. Deployment proceeded over the course of 507 s at a mean deployment rate of 2 mm/s. It is apparent that the boom deployment trend witnessed in the experimental case here closely matches that as was seen in Section 3.6.4. There are slight variations from the smooth simulated profile as the bus rate was not constantly maintained but otherwise the profile is as expected.

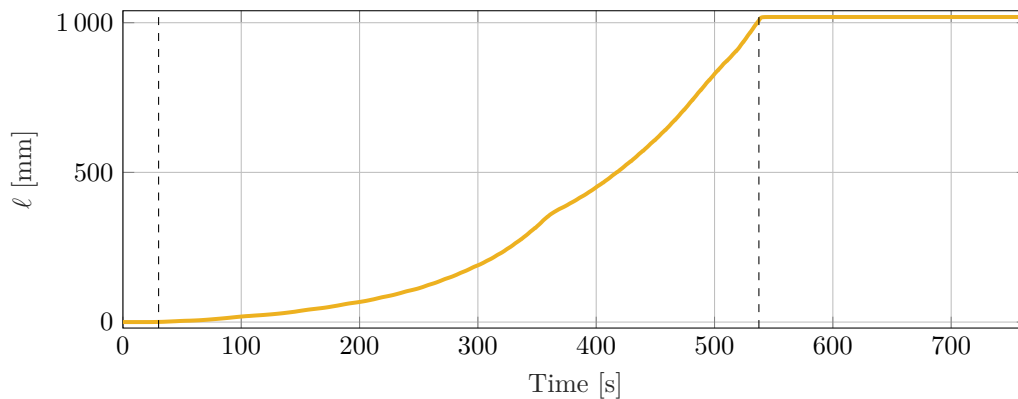


Figure 5.3: Deployed Boom Length Under Manual Control

The bus spin rate is presented in Figure 5.4. Both the measured bus rate as well as the spin rate set-point supplied to the spin controller are provided. During this test the bus spin was ramped to a rate of 2.8 rps and maintained there for some time. During the deployment stage the bus spin rate needed to be decreased. This was due to the spin controller output, and thus power consumption, starting to rapidly increase as the moment of inertia of the

spinning system increased. This is a constant amongst the tests conducted as neither the driving motor nor its power supply could maintain the high constant spin rate against the increasing moment of inertia and atmospheric drag.

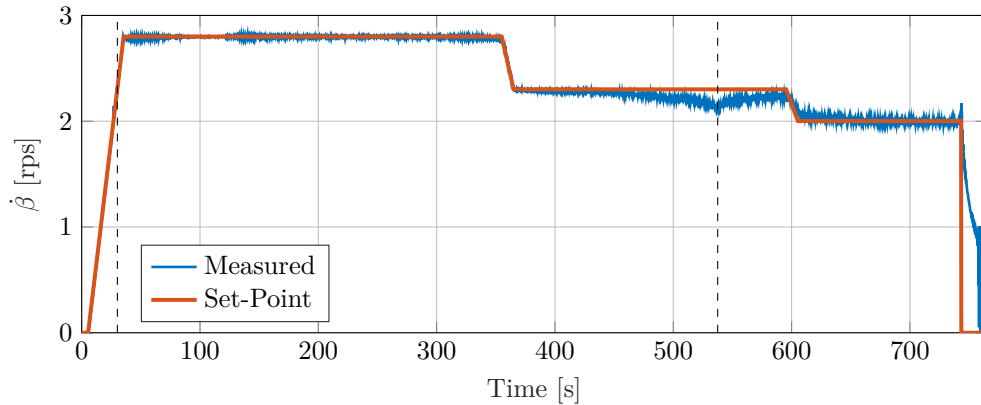
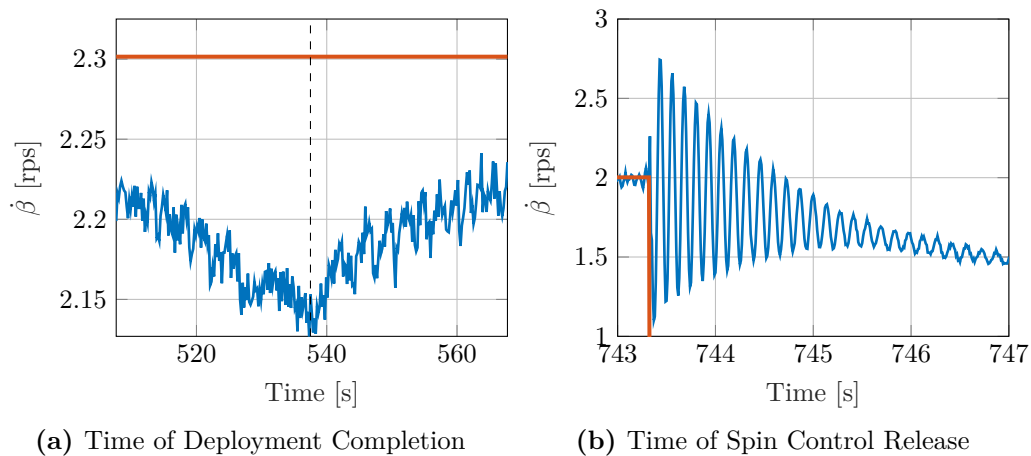


Figure 5.4: Experimental Bus Spin Rate Under Manual Control

The lack of sufficient input torque becomes more evident in the late deployment stages, after $t = 450$ s, as the bus spin rate can no longer maintain the necessary spin rate specified. The slight decrease in the spin rate caused by this occurs just before deployment and the negative effects thereof on the deployment are thus minimal. Deployment completes at $t = 537$ s, at this time the deployment rate of the booms suddenly ceases and $\dot{l} = 0$. The moment of inertia of the spinning system, and thus the energy input required to maintain the spin rate, becomes constant from this point onwards. As the system energy no longer has to constantly increase to maintain the spin rate of the mechanism, the spin rate is suddenly able to approach the set-point again, as can be seen in Figure 5.5a, causing a sharp change in the bus spin rate.



(a) Time of Deployment Completion

(b) Time of Spin Control Release

Figure 5.5: Focused Bus Spin Rate Behaviour

The measured bus spin rate as presented in Figure 5.4 also displays a quality which may be interpreted as noise, which suddenly grows after deployment has completed. While this measured signal does contain a component of noise due to the discrete measurement and numerical differentiation of the bus angle, the sudden increase in this perceived noise can be attributed to the expected oscillation of the in-plane boom offset angle. This oscillation is small in amplitude due to the fact that torque is still being applied to the spinning system at this stage, and it is thus almost lost in the measurement noise. The decreases in the bus spin rate would also contribute to greater in-plane boom offset angles.

More interestingly, this oscillation does not appear to dissipate notably in the 206 s from the time deployment completes to the point at which control over the spin rate is relinquished at $t = 743.3$ s. This may suggest that the boom damping value used in simulation was significantly greater than that experienced by the boom wire material used in the experiment; which is not completely unexpected. When control of the spin rate is ceased the oscillations induced in the bus rate are clear. At this point in the test the spin rate is 2 rps. As soon as control is released the spin rate falls to 1.1 rps and then is accelerated to 2.74 rps in the space of 0.1 s. This oscillation is clearly seen in Figure 5.5b. This offers greater confirmation of the presence of a significant in-plane boom offset angle which can have a large impact on the bus spin rate.

For comparison purposes as well as to better understand how the in-plane boom offset angle behaves during this deployment case, a simulated deployment was conducted which makes use of the known physical properties of the experimental set up and the damping and friction values found in Section 5.1.2. These results are seen in Figure 5.6.

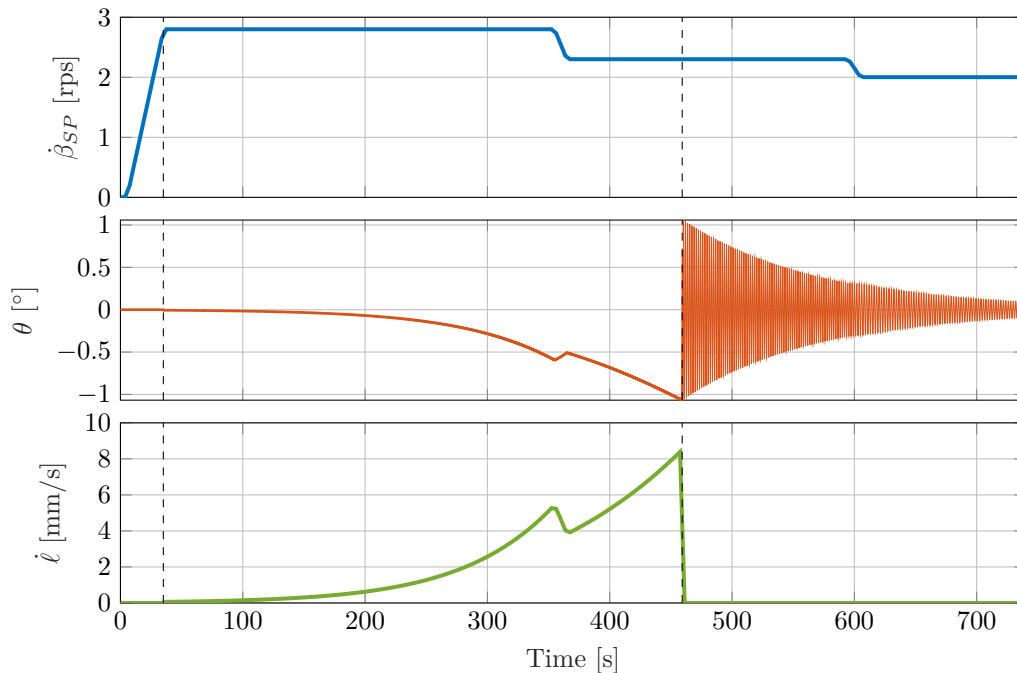


Figure 5.6: Simulated Deployment Result With Experimental Parameter Inputs

The same spin rate setpoint was used to drive the simulated deployment. It can be seen that as the deployment rate, $\dot{\ell}$, increases so does the boom offset angle, θ . Both the deployment rate and offset angle decrease when the bus spin rate is decreased mid-deployment. At

this point there is a minor oscillation in the boom offset angle as it suddenly changes. At the point of deployment completion, a far more prominent oscillation is induced in the booms' offset angle. A note on the time scale of the deployment: the practical deployment took 507s while the simulated deployment took only 424s. This is attributed to possibly imprecise values for the pulley rotary damping and friction as well as the perfect boom winding assumed in the simulated case. As was seen in Section 3.9, the deployment time can differ greatly with small differences in the pulley radius when the pulley hub radius is small, as is the case in the experimental deployment mechanism.

5.1.4 Bus Rate Spin Controller

The output of the spin controller during the manual deployment test under discussion can be seen in Figure 5.7. Once deployment commences and a steady bus spin rate is maintained, the increase in the spin controller output is very gradual for approximately the first half of the deployment process whereafter it begins to rapidly rise. A slight dip in the controller output can be seen where the bus rate set-point was decreased. As deployment reaches the final stages the gradient of the spin controller output becomes significantly steep. The general profile of this curve somewhat matches that of the increasing boom length as was seen in Figure 5.3. This is appropriate, as the increase in input energy required is proportional to the increasing moment of inertia of the spinning system.

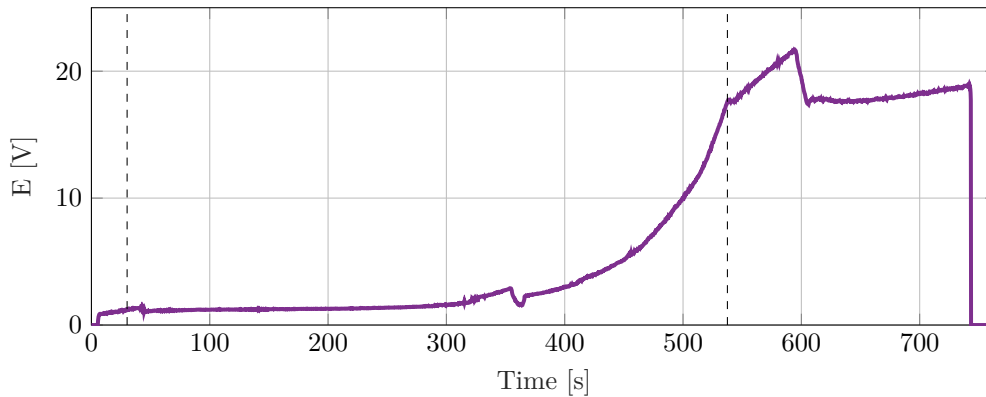


Figure 5.7: Spin Controller Output Under Manual Control

At the point of deployment completion there is a sudden decrease in the spin controller output gradient, clearly indicating that the boom length is no longer increasing. There is, however, still an unwarranted steep gradient to the controller output. This is a result of the integrator wind-up of the PID spin controller, leading to this slower and constant increase in the controller output. At about $t = 600$ s the spin rate was decreased to 2 rps and a command was issued to the spin controller to zero the integrator aspect of the PID controller. This results in the flat gradient of the controller output seen thereafter. After some time there is seen to be a slight renewed increase in the controller output. This is caused by the controller attempting to overcome the constantly oscillating bus spin rate due to the boom oscillations. The integrator and derivatives terms of the controller are particularly sensitive to this.

The spin controller output during deployment shows some clear characteristic trends under the influence of the increasing boom length. Initially there is the gentle increase in the controller output as deployment slowly begins. Once deployment is fully under way and a significant portion of the boom has been deployed, the gradient starts to increase more

rapidly; it is at this time that the bus rate can be safely decreased while still maintaining sufficient centrifugal force on the boom tips for deployment to continue. Finally, at deployment completion, there is an abrupt change in the gradient of the controller output as the energy input to the system no longer needs to constantly be increasing to such an extent. These features of the spin controller output can be used as a rudimentary means of detecting the stages of deployment, allowing some automated control of the bus spin rate.

5.2 Deployment Detection and Control

It is desirable to have some form of control over the deployment process even though the deployment proceeds in a passive manner. The only controllable input to the system was the bus rate, and through this the boom deployment behaviour could be indirectly controlled but the boom length could not be directly measured. While the deployment rate of the booms proceeds in a slow manner as seen in Section 5.1.4, the controller output increases rapidly in the later portion of the deployment process, requiring significant power to maintain spin of the mechanism. A method of control was desired to reduce the risk of such excessive motor power requirements. Methods of determining the status of the deployment as well as appropriately controlling this deployment were to be developed.

5.2.1 Deployment State Detection

Depending of the state of deployment, which could be either pre-, mid-, or post-deployment, the control strategy may differ. It is thus necessary to develop characteristics by which this state change may be detected. It is assumed that there may be no direct measurement of the pulley rotation and thus no means by which the deployment state can be directly observed. The effects of the deployment on the control of the system are thus observed instead, as these are the only direct measurements of the system behaviour available to inspection on the stationary side of the experiment.

If the spin control set-point is kept constant for a period of time the effects of deployment can be seen in the controller output, denoted as E . As boom deployment proceeds the moment of inertia of the spinning system increases, the torque input to the system has to increase accordingly in order to maintain the set constant spin rate. If the spin rate had to be maintained at that which was required to initiate deployment with the experimental mechanism, a large driving motor would be required. This problem of rapidly increasing motor torque output is compounded by the fact that these tests are conducted in atmospheric conditions, resulting in significant aerodynamic drag which also increases with increasing boom length.

The spin controller output, E , was used as the control input signal in determining the state of deployment progression. While the current consumed by the driving motor was also available, this proved to be an un-reliable stream of data because of the PWM driven nature of the motor driver. The PWM induces rapid current changes - an analogue motor driver would have been more appropriate in this regard.

The controller output was seen, in Figure 5.7, to have a very slow and slight increase in output at the initial moments of deployment as the centrifugal force and thus deployment rate is low; the controller output does however quickly rise in the later moments of deployment. Once deployment has completed, the spin controller output has a sudden and dramatic decline in its gradient as the torque required to maintain spin steadies. There may, however, still be a slight and constant gradient to the controller output as the integral term of the PID spin controller grows significantly during deployment.

To determine whether the deployment has commenced and whether the deployment state has transitioned from a not-deploying to deploying state, $S_0 \rightarrow S_1$, the initial small increase

in controller output is used. This is the most challenging state transition to reliably detect, as the change is gradual and sensitive to parameters such as signal noise and PID control variables. The input to the state change detection algorithm is thus a rolling averaged and filtered value taken over a long period of time. If the averaged spin controller output in one state control time step is appropriately higher than that in the previous it can be said, with a fair degree of certainty that deployment has commenced.

As mentioned, in the mid- to later period of the deployment process the mean (of that controller time step) controller output gradient, $\dot{\bar{E}}$, increases rapidly. This rapid increase can be easily detected to confirm the previous detection that deployment is under way. It is also an indication that deployment is in the later stages and the end may occur soon. This steep gradient of the spin controller output was used as an intermediate stage in order to avoid false positives, where the detection algorithm may falsely identify the low to zero gradient of the spin controller output at deployment completion as that which occurs before deployment initiation.

As mentioned a sudden change in, or lower gradient of, the spin controller output is indicative of deployment completion and was used as the primary means of detecting that deployment had come to completion. The condition that the intermediate deployment stage, $S_{1.5}$, previously discussed, must have been detected at least once was enforced. The various deployment stages as well as their defining transition features are summarised in Table 5.1. The various thresholds are indicated by ψ .

Table 5.1: Deployment Progression States

State	State Description	Defining Transition Feature
S_0	Not-Deploying	$S_0 \rightarrow S_1: (\bar{E})_{t=k-1} < (\bar{E})_{t=k} + \psi_0$
S_1	Deploying	$S_1 \rightarrow S_{1.5}: \dot{\bar{E}} > \psi_1$
$S_{1.5}$	Deploying: Late Stages	$S_{1.5} \rightarrow S_2: \dot{\bar{E}} < \psi_2$
S_2	Deployment Complete	

5.2.2 Deployment Controller Concept Design

As was mentioned, the very large change in inertia of the spinning system elements can easily cause the controller and motor to become saturated. The spin rate of the controller thus needed to be managed in such a way that this did not occur. It was also desired that the deployment controller could automatically find the spin rate at which deployment would initiate. A deployment controller was thus designed to this effect.

The conceptualised controller flow diagram is presented in Figure 5.8. The deployment controller adjusts the spin rate based on the current deployment state and spin controller output. The state transition conditions presented earlier in Table 5.1 are heavily dependent on how the controller output changes from one sample to the next. Any controlled changes to the spin rate will thus alter the spin controller output and result in false or invalid readings. Sampling periods where the spin rate set-point has or has recently changed cannot be used for deployment control or state transition determination and are thus ignored. This results in periods of no deployment control or state checks during the deployment process.

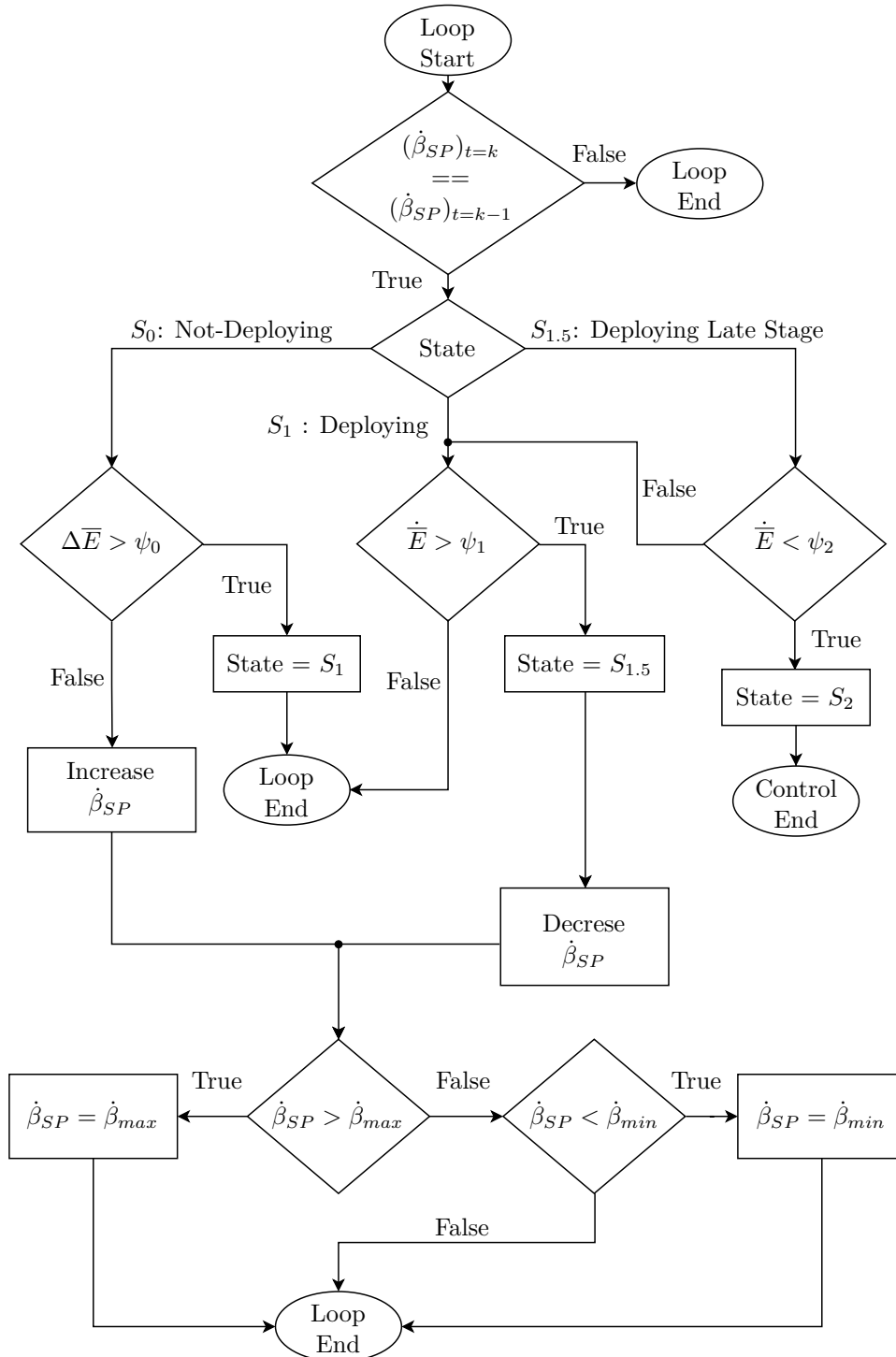


Figure 5.8: Deployment Controller Logic Diagram

Due to the slow nature of the experimental deployment process, the deployment controller's time step can be specified at quite a large value. This is particularly useful in the pre- and early-deployment stages, as the changes to the spin controller output are very gradual.

This also provides ample data points over which to filter and average the data, for a more representative reading to be supplied to the deployment detection algorithm. The control logic loop supplied in Figure 5.8 is repeated from the time the deployment controller is activated to such a time that it has transitioned through all the deployment stages to deployment completion at 5 s intervals. The deployment controller is then terminated.

In order to not request unreasonably high spin rates from the experimental platform, or rates that may cause the booms to collide with the work surface, limits are placed on the minimum and maximum rates. It is already known that deployment will commence at approximately 2.6 rps which is the highest rate which theoretically needs to be achieved. As deployment occurs this rate is lowered as the increased boom length increases the centrifugal force. A maximum allowable bus rate of 4 rps is enforced for the safety of the experimental components. When the booms are fully deployed the spin rate can be lowered to approximately 1 rps before the tip masses collide with the work surface due to gravity. The minimum bus rate is set at 1.5 rps to ensure that this collision does not happen even if the bus rate is dropped to the minimum when the booms are not fully deployed.

5.2.3 Controller Implementation and Results

The state detection and the deployment controller derived were implemented on the experimental platform. The behaviour of the controller is heavily dependent on the thresholds chosen. The values specified will determine how effectively, as well as how reliably, the state changes are detected. Thresholds were found by applying the detection algorithm and using the data captured from manually controlled cases as the input. This allowed initial values to be obtained for use in practical application of the controller. It is noted though, that the values and thresholds used are highly sensitive to the signal noise, even after the data has been filtered. This will be demonstrated later.

The output and results of both the spin and deployment controller is presented in Figure 5.9. This test proved very successful as deployment start and completion was detected quickly, and the spin controller driving motor never reached saturation. The test began by ramping the bus spin rate to 2.5 rps, just below the rate required to initiate deployment. The deployment controller then checks for an increasing spin controller output and, without the detection thereof, increases the spin rate by 0.1 rps. Deployment is detected shortly thereafter and the spin rate is maintained at a constant until a steep gradient is detected triggering a reduction in the spin rate set-point. This can be seen in Figure 5.10.

In Figure 5.9 the raw spin controller output data is provided as the semi-transparent plot and the deployment controller input average of this data by the solid purple plot. The deployment controller states are indicated by the shaded regions: no shading indicates S_0 where deployment has yet to be detected, blue represents S_1 and $S_{1.5}$ during the deployment phase, green is where deployment has completed in S_2 , and red shaded regions are where the detection and control is disabled due to a recent change in spin rate set-point. The deployment controller is disabled for both the control time step in which the rate change takes place and the one thereafter. As is the convention, the actual start and end of deployment is shown by vertical black dashed lines.

The spin rate was decreased by 0.25 rps three times during the deployment process. As the deployment controller operates with a large time step of 5 s, and the rate of the controller output tends to increase so rapidly in the late deployment stage, the reduction in spin rate needed to be substantial. Note that while the set-point decreases instantaneously the spin rate is allowed to decay to the new set-point without interference. The spin rate at deployment completion is 1.85 rps.

While there is a substantial change in the gradient of the spin controller output at the point of deployment completion, the gradient does not decrease to the degree that might be

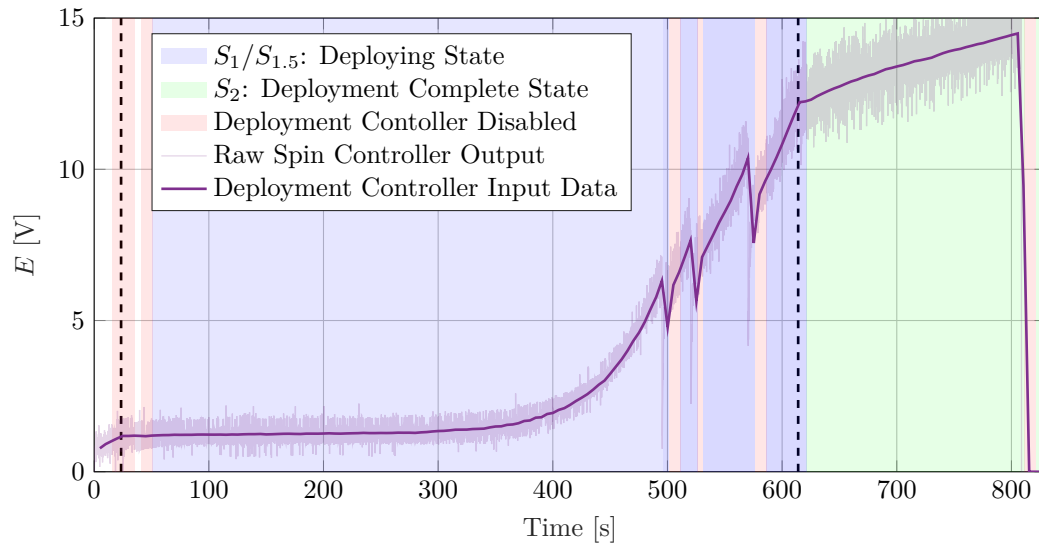


Figure 5.9: Spin Controller Output and Deployment Controller States

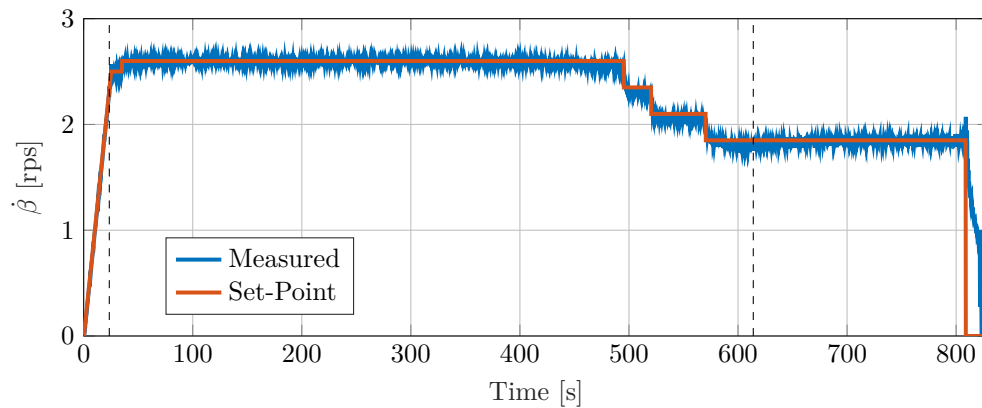


Figure 5.10: Spin Rate with Deployment Controller

anticipated. This again is believed to be primarily due to the integrator wind-up on the spin controller resulting from the increasing moment of inertia which had to be accommodated, as well as the in-plane boom oscillations which were present.

The changing boom length is presented in Figure 5.11. The rate of deployment is shown in Figure 5.11b. Here again the trend is similar to that as was in seen in simulation. There is a decrease in deployment rate corresponding to each decrease in bus spin rate. The deployment rate peaks at 5.44 mm/s before the bus rate is decreased for the first time while the average deployment rate over the entirety of deployment is 1.73 mm/s. The periodic variation seen in the deployment rate of Figure 5.11b is attributed to the non-perfect mounting of the encoder relative to the spinning magnet.

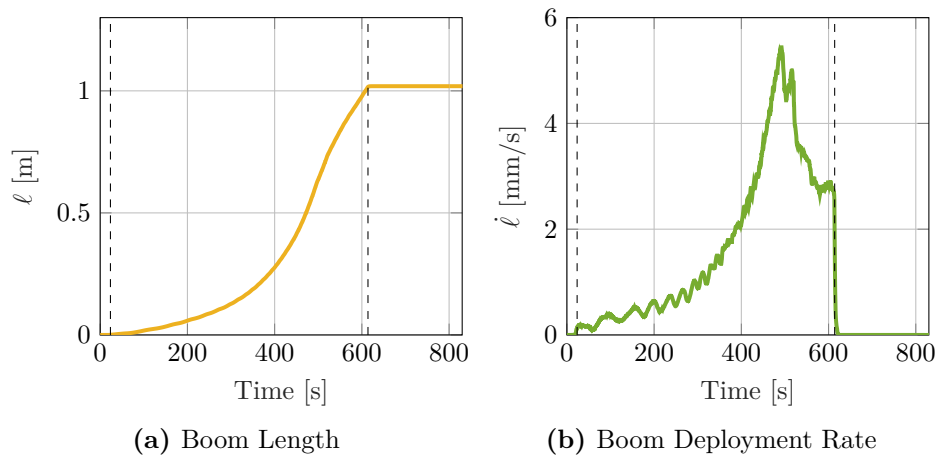


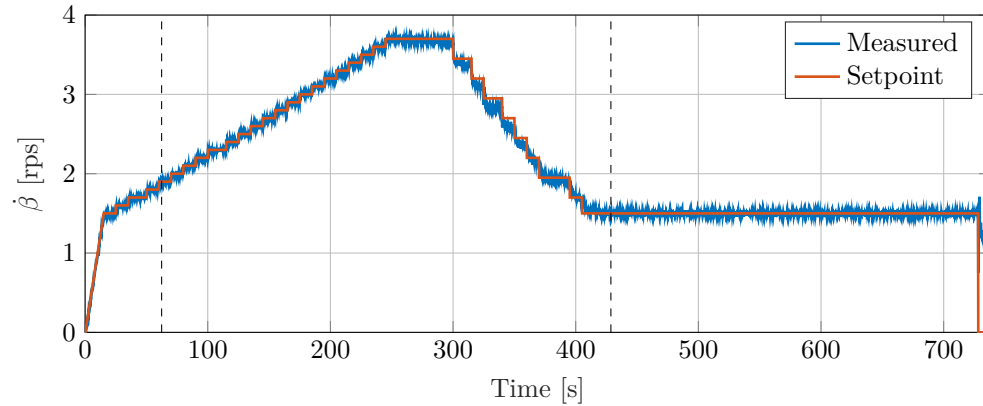
Figure 5.11: Boom Behaviour with Deployment Controller

Controlled Deployment With Late Detection

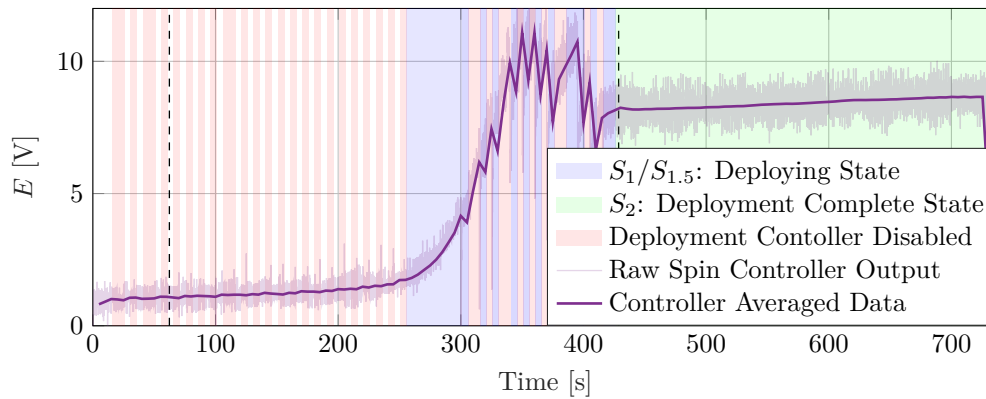
It was mentioned that the performance of the deployment controller is sensitive to not only the threshold values chosen, but also the initial spin rate that is ramped to before passing control to the deployment controller. This particularly impacts on how successfully the start of deployment was detected. To illustrate this, a test performed with a lower starting spin rate of 1.5 rps is presented in Figure 5.12. When the driving motor operates at lower spin rates the narrower pulse width of the PWM signal results in significantly more noise in the spin rate of the motor, which is fed back into the spin controller. In order to not falsely detect the start of deployment at these lower spin rates, it is required that the threshold which indicates deployment has begun be set higher. This results in the deployment being detected much later in the deployment processes; while the deployment controller continues to increase the bus spin rate.

In the presented dataset, deployment strictly begins at a bus spin rate of 1.9 rps, although deployment thereafter all but ceases again and only continues at $t = 164$ s when the spin rate reaches 2.8 rps. This small amount of deployment at the low spin rate can be attributed to the force impulses from the stepped increases in bus spin rate, allowing slight rotation of the pulley. Deployment however is only detected at $t = 256$ s at a spin rate of 3.7 rps. This initial high spin rate results in a significantly faster deployment overall of 2.78 mm/s. In addition to this the maximum output of the spin controller, and thus the input to the motor, is significantly less at almost half of the previously discussed case. The detection of $S_{1.5}$ was done efficiently and with somewhat greater ease as, because of the higher deployment rate, the gradient of the spin controller increase more rapidly than in the previous case; this state was triggered many more times however, to reduce the final spin rate to a manageable value. The spin rate in this case was decreased down to the minimum allowable rate. The detection of deployment was again successful.

The low gradient of the spin controller output post-deployment is here more akin to what would reasonably be expected. The higher deployment rate and resulting shorter deployment time provides a shorter time frame in which integrator wind-up of the PID controller can occur. Additionally, the higher bus spin rate, and thus higher centrifugal force, reduces the amplitude of the in-plane boom oscillations which occur, which produces less variation and noise in the bus spin rate, and leads to a smaller integrator controller component.



(a) Bus Spin Rate



(b) Controller Outputs

Figure 5.12: Deployment Controller; Late Detection

5.3 Chapter Summary

The experimental hardware designed was used to conduct a number of small-scale boom deployments with success. Some of the dynamic trends seen in simulation were observed in the practical results. Parameters such as the in-plane boom offset angle, which were not directly measured, could not be directly confirmed but the effects thereof could be. The clear oscillations in the spin rate (as seen in Figure 5.5b) of the deployment mechanism could not be induced without the presence of some form of boom oscillation. Reliable, passive deployment of a wire boom by the use of rotary dampers as been shown to be a viable design solution. It was also found that the static pulley friction in the design is highly sensitive to assembly cases but with careful assembly, of even a simplified design, the static friction can be nominally maintained.

A simple deployment state detection and logic controller was prototyped and implemented. The goal was to control the spin rate of the mechanism, and thus control deployment to a degree, with no direct measurement of the booms' deployment state. Changes in the output of the motor controller driving the spin rate was used to detect the state changes from pre-deployment, through mid-deployment, to completed deployment. The deployment controller implemented proved to be simple yet effective at detecting the changes in states. Deployment completion was consistently well-detected but the start of deployment proved

more difficult to reliably detect. Deployment proceeds tremendously slowly initially, leading to minimal changes in the controller output which, in some cases, is difficult to detect above the noise level of the data even when heavy filtering is applied to the signal. The noise in the data can partially be attributed to the under-sized motor and controller used. The use of a brush-less motor or an analogue motor driver would have reduced these negative effects, but this would add significant complication to the driving electronics required.

Sufficient practical insight was gained in the course of the experimental regime that significant improvements can be recommended for the mechanical design of the deployment mechanism. These will be presented in the following chapter.

Chapter 6

Practical and Mechanical Experimental Observations

After the practical experience gained from the conduction of numerous experimental tests, several observations can be made relating to the mechanical design and operation of the deployment mechanism, and improvements can be suggested. Revised mechanical designs are then presented, taking into account the lessons learnt from practical experience gathered during testing, which may be used as an engineering test unit for further refinement of the mechanism.

6.1 Lessons Learnt

During experimentation several aspects of the mechanism were seen to require refinement and redesign for more predictable and reliable operation. Here these issues, with their associated improvements, are discussed.

6.1.1 Boom Winding Inconsistencies

It was noticed very early on that the winding of the wire booms is severely prone to inconsistencies, the consequences of which manifest during the deployment stage. In the experimental deployment mechanism, the four booms were wound around a common central hub area constrained by two flanges. This fact, coupled with the small hub diameter of 5 mm, resulted in the individual booms being wound at an inconsistent rate leading to the booms having different "slop" lengths once wound. This varied between both individual booms and winding instances. The root cause of the issue is that the booms coil relatively unconstrained and thus do not fall in the same arrangement on the hub every time. The small hub diameter compounds this issue as many revolutions of the pulley are required to fully wind the booms. In order to rectify this, each of the four booms should be wound on individually separated areas of the hub. This does add additional complexity to the manufacture of the mechanism but should result in more consistent winding results. The diameter of the pulley also should be increased as much as possible, which has multiple effects on the mechanism's operations. A hub with a larger diameter requires fewer rotations to wind or unwind the boom. Fewer rotations of the bus leave less room for error in the winding and the estimations of the boom length. This also increases the torque that the deploying booms apply to the pulley through the increased lever arm. This increased torque will affect the deployment rate and the pulley damping required will need to be adjusted accordingly. The geared design of the damping mechanism allows some flexibility on this.

Figure 6.1 presents examples of both acceptable and poor winding instances. Note that the better wound case has a reasonably straight vertical profile to the outer winding layer and

that the booms leaving the pulley are staggered where one pair of opposite booms diverge from the pulley in the top portion, and the other pair of booms do so in the lower portion of the pulley hub height. The poorly wound booms example forms an unbalanced profile with the booms mostly wound around the upper portion of the pulley hub and the booms winding mostly in the same portion of the pulley. This is evident as the booms meet the pulley and windings in approximately the same plane. The vertical spacing of the boom followers was found to have a significant influence on how well the booms wound by guiding them to the correct vertical position.

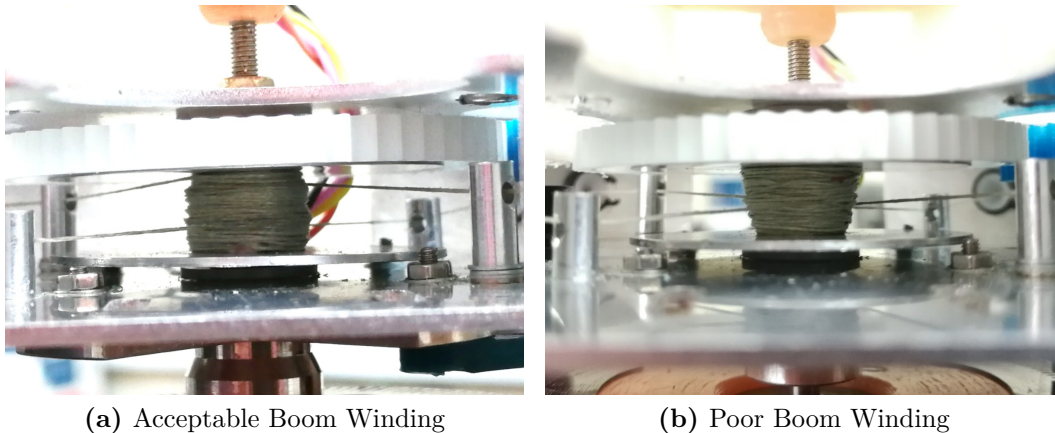


Figure 6.1: Boom Windings

It was also found that the booms must be wound up under tension. Thin braided line with a diameter of 0.2 mm was used for the boom wires in the experiments. This line is well suited to this application as it has a high tensile strength while being highly flexible, lightweight and having little to no shape memory or spring characteristics. The thin cross section allows more to be wound onto a smaller pulley and reduces the effects of the atmospheric damping during experiments. This thin cross section had an unforeseen consequence in that it was very easy for a coiled section of the boom to slip down between previously wound layers. This caused that section of boom to "hook" during deployment resulting in a discontinuity in the deployment rate and having erratic effects on the bus rotation rate. This was solved by winding the booms at a constant rate and tension as per the method previously discussed in Section 4.6.1.

The method of winding used during experimentation was simple and worked for the purposes of the experiments where the booms were kept short. For instances where booms of long lengths are required a different method is suggested: the winding cables are to be coiled around individual external spools with large radii where the spool rotation is constrained by a constant force coil spring. The winding cables are then attached to the tip masses and the booms retracted using a driving motor on the central pulley as before where the springs supply the winding tension required. This is illustrated in Figure 6.2. A similar winding apparatus was used in the winding of the deployable instrument probes of the DICE spacecraft [71].

The poor boom winding was not unanticipated, but the pulley hub radius was purposely designed small for the experiment in an attempt to see the effects of the decreasing effective radius, as well as to facilitate ease of manufacture. The winding correction factor during experiments was found to be approximately $k = 0.12$, where 1 would have represented perfect

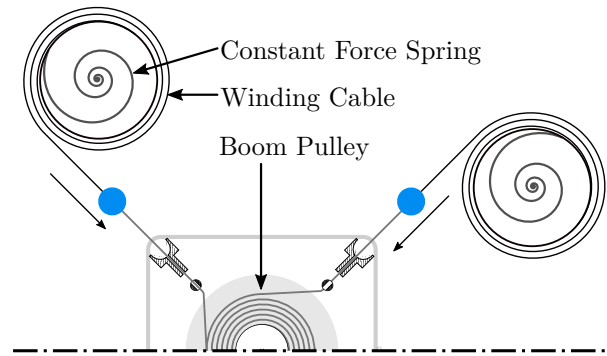


Figure 6.2: Proposed Winding Apparatus

winding. This shows how even what was deemed acceptable winding proved, empirically poor. This, however was not completely unanticipated, and the winding correction factor was known to be highly sensitive to wire diameter.

6.1.2 Pulley Friction

The static friction between the pulley and its mounting bushings has an effect on the bus rate required for deployment to commence. The simple cylindrical shaft design used in the experimental set up was effective but was very prone to inconsistencies during disassembly and reassembly. This is most likely due to deformation of the top and bottom plate of the bus assembly resulting in an axial load on the shaft shoulders increasing the friction. A bushing with low friction is desired, which can withstand the vibrations during testing and launch, have allowance for thermal expansion and have a very small footprint.

6.1.3 Tip Mass Mounting

The spring loaded tip mass locating method used was effective in absorbing the slight inconsistencies in differing boom lengths but proved insufficient in light of the large boom winding inconsistencies discussed. The experimental mechanism design allowed for up to about 4 mm variation in boom length, which often proved too little during experimentation because of the larger than anticipated winding inconsistencies. The rectifications to the pulley construction and winding methods discussed should allow this amount of play in the tip mass mounting to be sufficient.

The force applied to the tip masses by the spring exceeded the static friction of the pulley. Ideally this should not be the case as the purpose of the spring is merely to absorb the slight inconsistencies in boom length and not to initiate deployment. Springs of the appropriate size and stiffness could not be easily obtained for the experimental model and springs of too great a stiffness were used. This still allowed the effectiveness of the solution to be demonstrated but failed to retain the booms at the start of the experiments. It should be noted that the experimental deployment mechanism does not include a locking pin for the pulley as it was deemed an unnecessary complication, while the flight design model does require means of locking the rotation of the pulley within the mechanism before the desired time at which deployment should commence.

6.2 Revised Mechanical Design

Based on the practical knowledge garnered from experimentation the hardware designed can be improved. The notion of a mechanism which can be used on both full-spin as well as

dual- or tri-spin satellites with minimal design adjustments will be considered as was the case in the experimental deployment mechanism design.

6.2.1 Passive Deployment Design

The passive deployment method demonstrated in experimentation proved effective. A second iteration of the experimental deployment mechanism is presented. This design has some compromises due to the use of multiple dampers. A second design using a single damper is also presented which uses much of the same components and layout, except for the means by which the damping torque is applied to the pulley.

6.2.1.1 Geared Dampers

A direct evolution of the experimental deployment mechanism is presented which uses similar components and general component layout. An exploded view of the mechanism and its components can be seen in Figure 6.3

The same variety of dampers are used as previously but rather multiple smaller dampers of the same class are used. The use of multiple smaller dampers offers some advantages: more control over the damping acting on the pulley is possible, and the use of multiple dampers offers redundancy. If one of the four dampers were to fail, the deployment would proceed at a faster rate while still retaining a high likelihood of success, as even a small amount of pulley damping can still result in an acceptable deployment as was seen in simulation.

The tip mass mounting assembly saw a large design change. In order to fit a greater tip mass in a slimmer volume the shape of the tip mass was altered. This allowed use of almost the full internal height of the deployment mechanism to stow the tip mass. The deeper 'V' shaped tip mass seat offers a more secure mounting as well as a guide in the initial moments of deployment as it provides a hard stop to the initial boom-offset angle growth. The corner blocks remain as the primary structural supports for the mechanism between the top and bottom plates. Two springs on guides are now necessary due to the altered tip mass seat design.

The wire guides remain, as they are critical to guiding the boom wires on the correct path. The wire guides now act as additional support between the top and bottom plate at a position closer to the mechanism centre. They are threaded to attach to the bottom plate, and an interference fit secures them to the top where an adhesive may be applied upon final assembly of the mechanism.

The experimental deployment mechanism used a simple cylindrical shaft and pin bushing. This design proved simple to manufacture and easily facilitated the mounting of the pulley encoder magnet. It is, however, neither the only plausible solution nor possibly the best. While being simple, a cylindrical bushing design is prone to friction and can be sensitive to thermal fluctuations, which may cause binding of the pulley shaft. The use of bearings may alleviate these negative effects but at additional cost, mass and complication, which is difficult to justify on a component which will only complete a small number of low speed revolutions in its operational life-time. As there is no explicit requirement for electronic hardware, such as an encoder, other designs can be considered without this limitation.

A pin support provides a very small contact area with low friction as well as both radial and axial locating. Beyond this an extended cylindrical section of the pin with a loose tolerance provides additional support when necessary. The cylindrical section is normally without contact and allows for thermal fluctuations in size, but provides additional radial support if required when the mechanism experiences vibrations or a radial force is experienced by the pulley. A cross sectional view of the pulley with pin supports can be seen in Figure 6.4; note that the assembly is not sectioned in a straight line through the pulley but is rather angled at the centre such that both the locking pin and fastener can be shown.

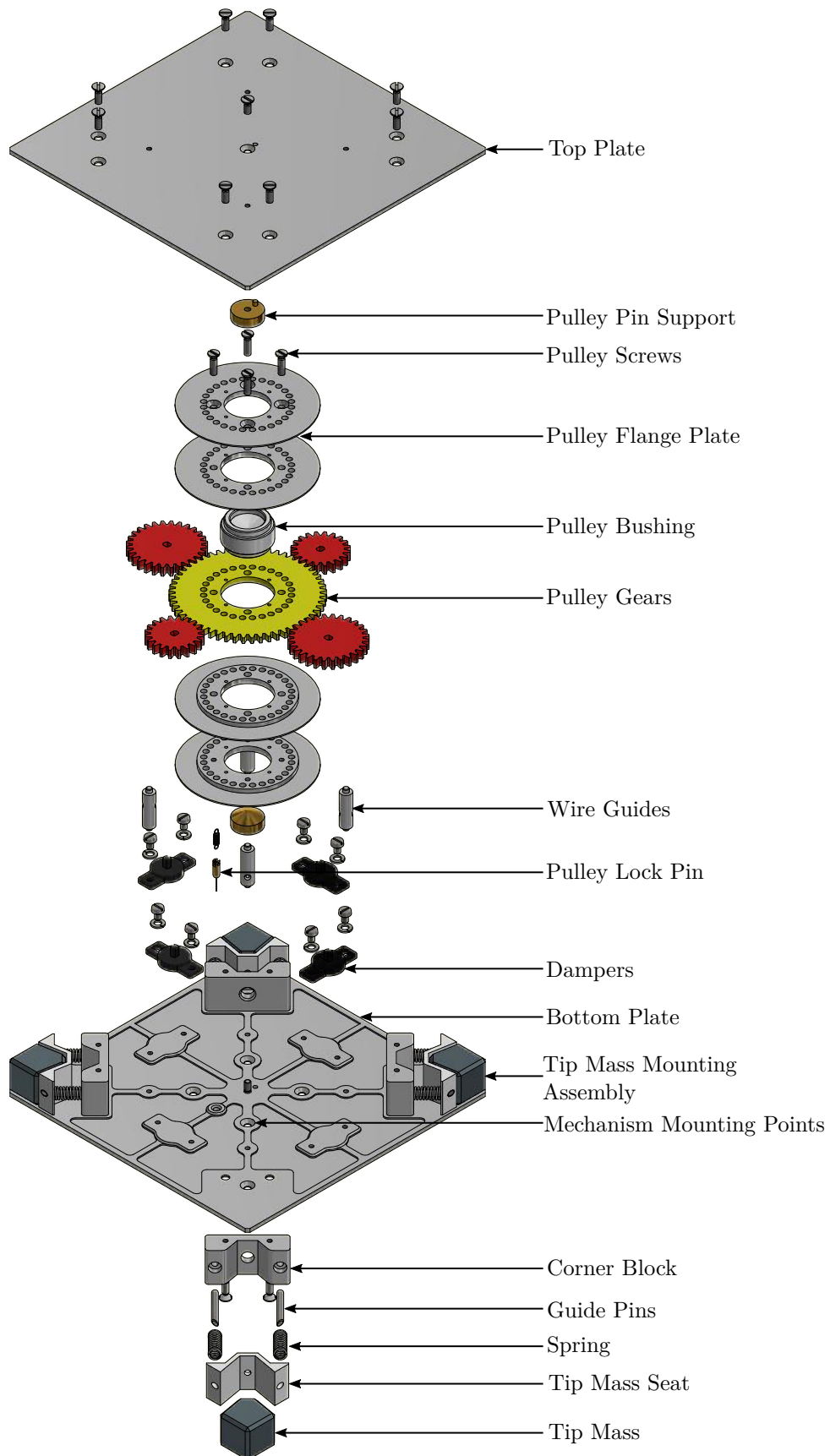


Figure 6.3: Revised Geared Damper Design Exploded View

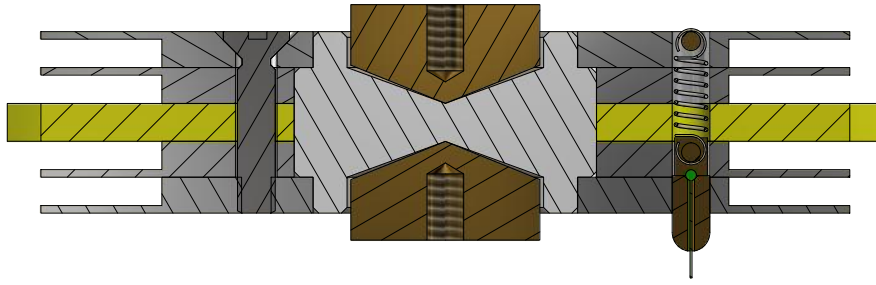


Figure 6.4: Pulley Assembly Cross Section

The pulley is constructed from a stack of individual components, allowing each boom to be stowed in a separate constrained volume. There are four pulley flange plates which make up the majority of the pulley and form the pulley hub, which the boom wires coil around, as well as the flanges which separate the discrete boom stowage volumes (Figure 6.4). The use of separate components to make up the pulley allows them to be more easily manufactured and allows the booms to be more easily attached through radial holes, much like in the experimental deployment mechanism. Central to the pulley is the pulley gear which engages the dampers. The gear is placed in the axial centre of the shaft to evenly distribute the radial forces from the gears between the two pin supports. A bushing constrained within the centre of the pulley assembly provides the interface to the pin supports and allows smooth rotation. The entire pulley component stack is held together by four fasteners.

The rotation of the pulley is locked prior to deployment by a locking pin located within the pulley (Figure 6.4). The pin locates in the bottom plate when extended, preventing rotation of the pulley within the mechanism. An extension spring is able to retract the pin into the pulley once a burn wire, illustrated in green in Figure 6.4, is severed externally to the mechanism. Multiple circumferential holes are provided around the pulley in which the locking pin can be placed during assembly. This adjustment provision is required as the angle of the pulley is fairly unpredictable once fully wound and any one of the provided holes may fall nearest to the locking pin hole in the bottom plate. The springs of the corner tip mass mounting assemblies provide the play necessary to perfectly align pin and hole.

6.2.1.2 Central Damper

An alternative design for the pulley within the mechanism is presented, which offers some benefits over the geared dampers design, with minor compromises. A single damper is used within the pulley. This allows for significantly more effective use of the mechanism volume and the accommodation of longer booms. A cross sectional view of the pulley design is provided in Figure 6.5, and exploded and assembled views are provided in Figure 6.6. The pulley is the major differing design element here from that of the geared damper design. The remainder of the mechanism requires minimal alterations to accommodate this pulley design. The tip mass mounting assembly remains mostly un-altered, except for the corner blocks which now also perform the function of the wire guides in ensuring the boom wire aligns with the pulley at the correct heights.

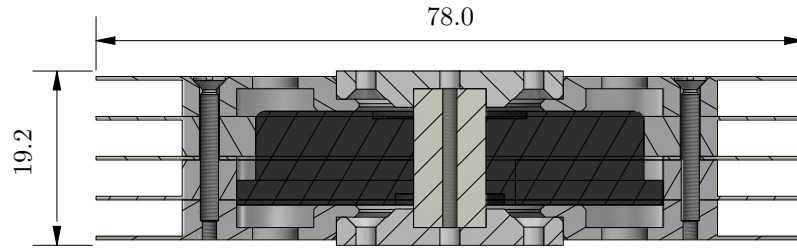


Figure 6.5: Central Damper Pulley Design Cross Section

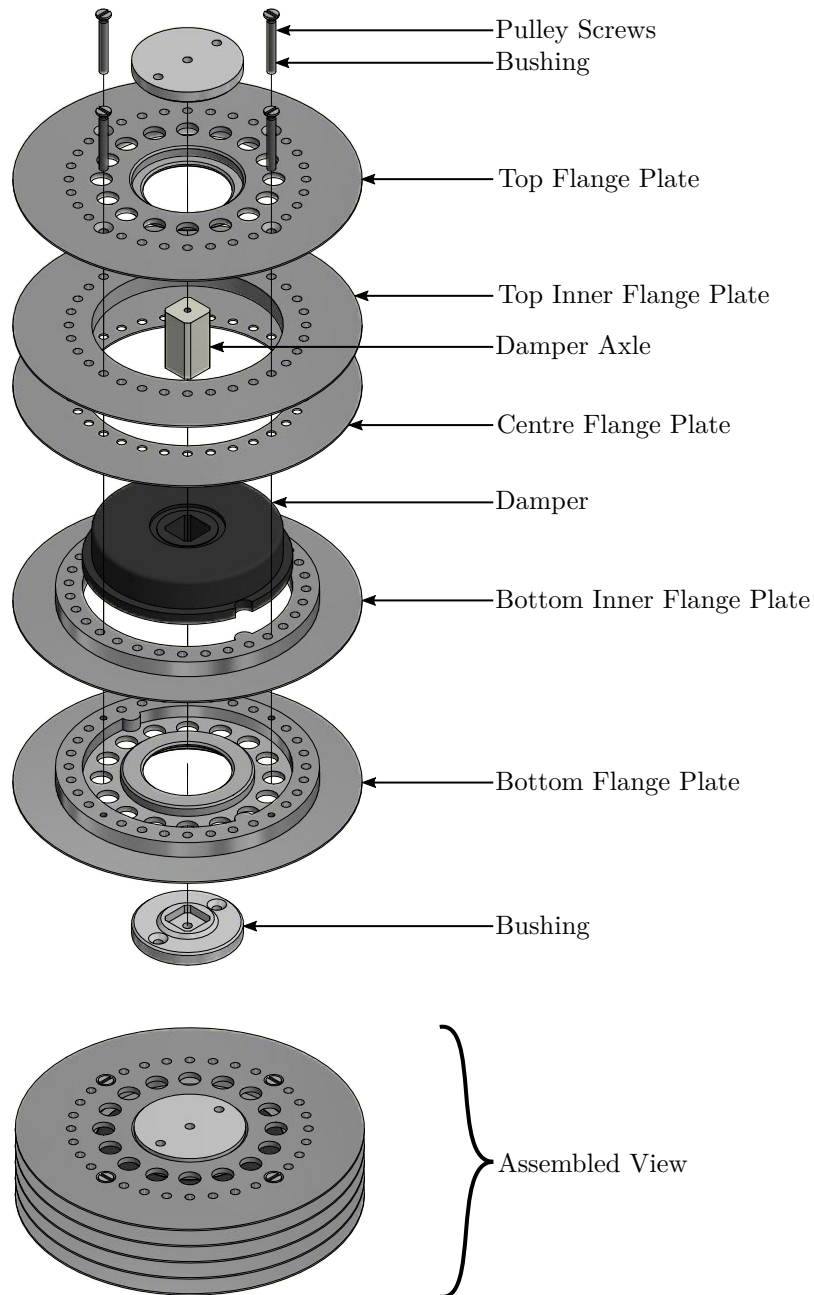


Figure 6.6: Central Damper Pulley Design

A FDT damper from ACE [74, p. 224] is used. This damper is physically significantly larger than the ones used in the previously proposed design but does not require any fluid for its operation; this possibly makes it more suited to conditions as would be experienced in space. The use of a single damper in the design is a compromise on any redundancy or fine adjustment in the design and requires a greater physical size of the mechanism. The height of this design, which is predominantly determined by the height of the damper, is 21.9 mm as opposed to the 14.9 mm of the geared damper design.

As is clear in Figure 6.5 the pulley, and boom stowage volumes, now make use of almost the full internal height of the mechanism as no gears need to be accommodated. A similar flange plate assembly stack design is used. The locking pin design and functional principal remains as with the previous design.

The pulley rotates on two cylindrical dampers fixed to the top and bottom plates. These fit within the outer pulley flange plates. The damper has a square axle which passes through the centre of the damper assembly and is fixed from rotating relative to the mechanism by recesses in the bushings. These recesses can clearly be seen in Figure 6.6. The damper and its axle may transmit no radial or axial loads. These are instead exerted between the mating surfaces of the bushings and flange plates.

6.2.2 Active Design

While a passive deployment mechanism offers many advantages to the active alternative there is one dominant drawback: the inability to directly control the deployment rate. In order to do this, an actuator is required through which the rotation of the pulley can be controlled. Several options exist for this such as the use of a DC motor or a ratchet-like mechanism as was used in the DICE spacecraft [71].

As was seen in the simulated active deployment case of a spinning solar sail in Section 3.7, where a constant deployment rate was used, torque opposing the pulley positive rotation is required rather than torque to drive the booms outwards. A means by which the input power required to deploy the booms can be greatly reduced is through the addition of a self-locking or anti-back drive mechanism. While specific mechanisms do exist which can achieve this, the function can be achieved by the use of gearing with high friction. The use of worm gears with low lead angles or high gear ratio gearboxes is common for this purpose [75]. High friction is a symptom of gearings with low efficiencies and high gear ratios; this is usually indicative of resistance against back driving. As a gearing may act as a friction brake to the deployment of the booms, a relatively low resultant torque motor and gearbox combination may be used.

A compact motor with a high gearing ratio and low efficiency is used, particularly a Faulhaber DC motor with integrated gearbox and encoder [76]. The motor has a high gear ratio of 814:1, an efficiency of only 43%, and can deliver a continuous output torque of $100 \text{ mN} \cdot \text{m}$. This is almost the same torque as was required in the simulated active deployment case, where a high friction was not present. Due to the high friction in the mechanism a smaller torque can be utilised as, assuming the gearing cannot be back driven, the motor only needs to apply the remaining force required to overcome the internal friction. A small pulley diameter is desired, such that the centrifugal force acting on the booms will apply a smaller torque on the pulley, allowing a smaller motor and gearbox to be used.

The motor is one of the few COTS components in the mechanism, as well as the largest, and thus would determine the size of the mechanism. The motor specified has a total length of 32.4 mm. The design of a pulley which surrounds the length of the motor may be used, which would effectively not add additional length to the assembled motor and pulley. This would, however, require the hub radius of the pulley to be larger, in turn increasing the

applied centrifugal torque and thus the size of motor required. A small pulley hub diameter is thus preferable.

The use of a small pulley allows a different design approach to be taken. The majority of the deployment mechanism may instead be incorporated into the "Tuna Can" volume allowed by the CubeSat standard [77]. A concept for such a mechanism is shown in Figure 6.7; the mechanism is shown without its cover, as well as with the Tuna Can placement on a 3U CubeSat.

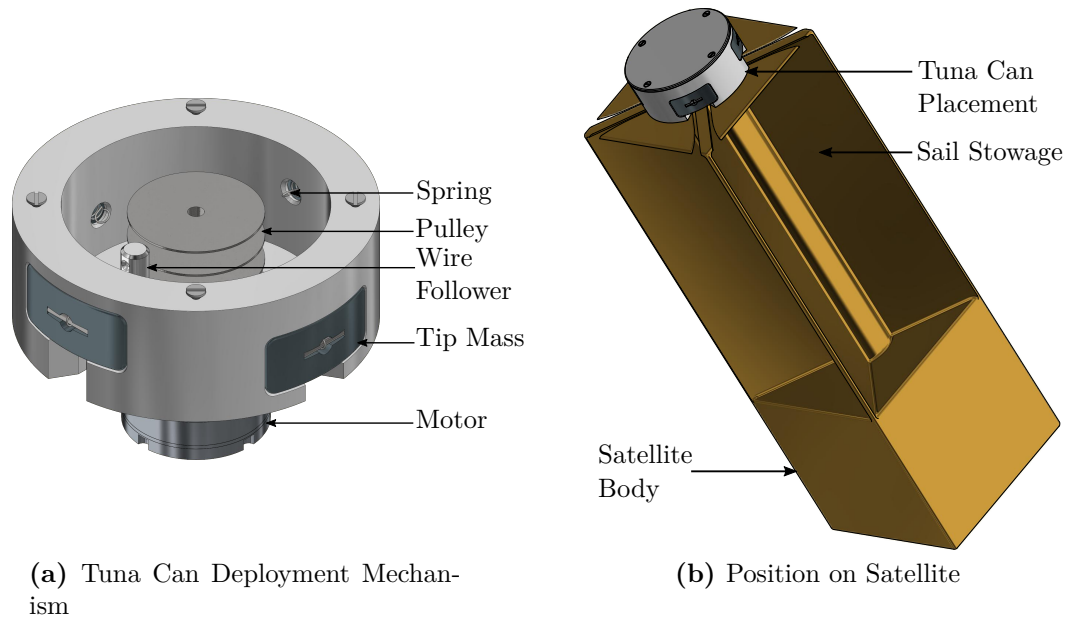


Figure 6.7: Active Deployment Mechanism Design Cross Section

A cross-sectional view of the mechanism can be seen in Figure 6.8. The pulley, booms, and tip masses reside within the Tuna Can volume, external to the main satellite body, while the actuating motor is within the main satellite body. The size limitations of the Tuna Can volume do not allow the entire mechanism, including motor, to be contained within this volume. The boom tip masses seat flush with the outside the of cylindrical volume and contain springs to absorb any slight differences in wound boom lengths. The tip masses are arranged vertically in opposite pairs to reduce the number of wire guides required, as well as to reduce the angles in the boom path. The boom tips are attached to the sail membrane corners by a short connecting tether which lies within the sail storage cavity and is pulled out along the slot seen in Figure 6.7b.

This proposed active deployment mechanism concept proves to be very small and compact and makes use of a volume allowed by the CubeSat standard not usually utilised, allowing more room for sail storage or other components. The use of this small volume is primarily facilitated by the small pulley hub radius, although this may potentially present some boom winding issues as has been discussed. As this mechanism is intended for use in a spinning sailcraft the centrifugal force drives the deployment, which in turn allows a very small actuator to be used relative to those required for semi-rigid boom sails, where the torque required is far greater. No locking pin is incorporated into the design, as it is assumed the high friction combined with electrically braking the motor will be sufficient to prevent premature boom deployment. As the stowed radius of the boom tips is small the centrifugal

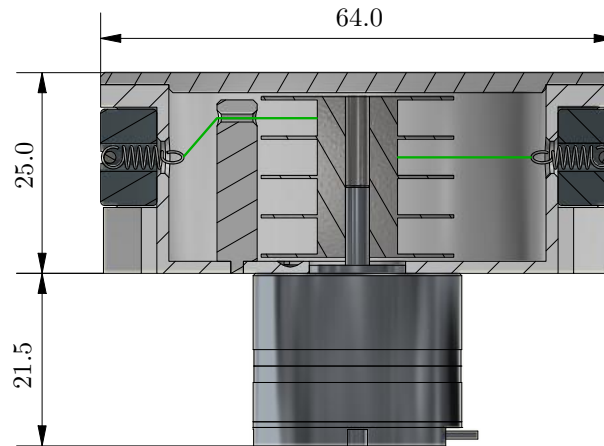


Figure 6.8: Active Deployment Mechanism Design

force acting on the booms is low, reducing the probability of a premature deployment. Testing of the components is required to confirm that these factors are sufficient to negate the use of a lock pin, however if a locking mechanism is found to be required this may be incorporated into the upper portion of the Tuna Can as the standard still allows 11 mm more height to be used.

6.3 Chapter Summary

Three deployment mechanism designs have been presented: two passive and one active. Both passive designs apply the principal of rotational damping to retard the rate of deployment. This has been shown to be an effective and stable means by which deployment can be achieved.

The geared damper design offers some redundancy but at a mechanical complexity cost. As multiple moving contact surfaces are present in the design, the static friction in the pulley may be large and could require high spin rates to initiate deployment; the use of pin supports and bushings should mitigate this effect. The central damper design uses only a single damper within the pulley itself. This greatly reduces the complexity of the mechanism assembly and allows for a larger pulley, as no geared dampers need to be accommodated. Then central damper may not support any forces on its axle and additional supporting bushings are thus required, adding some complication and friction to the assembly. Both these mechanisms are small at $0.15U$ and $0.2U$ respectively making them very compact. They have both been designed to deploy passively, requiring no external input or monitoring besides for the mechanism spin rate. This allows the designs to be used in any spacecraft spin configuration without the need for communication or control through a rotating connection. An encoder to monitor the pulley state can be incorporated into the designs with relative ease although the central damper design is more conducive to this.

The active deployment mechanism design concept proposed takes advantage of the small actuator and pulley used. The majority of the deployment mechanism components are housed within the Tuna Can volume allowed by the CubeSat standard. This is made possible by the use of a, centrifugal force driven, spinning solar sail design. This results in a novel, compact solution.

All the designs presented are capable of deploying long wire booms in a controlled manner. The core components of the designs, the dampers and brake, would require extensive testing and validation to determine their ultimate suitability for use in space.

Chapter 7

Conclusions

This chapter provides a final summary of the results and conclusions of this thesis. The most notable aspects of the deployment of a spinning solar sail which were established through simulation are reviewed. The insights gained from the conduction of practical experimentation are briefly presented along with a summary of the hardware design concepts which stemmed there from. Lastly, recommendations for future work are made, which may further develop and build on the findings of this thesis.

The focus of the thesis was on the deployment of a spinning solar sail from a 3 U CubeSat. A spinning sail offers many advantages over a non-spinning or three-axis stabilised sail, particularly that it possesses inherent gyroscopic stability and proves to be practically far more scalable. A means of deploying the sail booms passively was also desired, as this has the potential to provide a mechanically and electrically simple solution which requires minimal input power or control, as opposed to an active deployment strategy. A passive means of deployment is also more desirable when considering a satellite with multiple body spin rates, as no signal transmission is required over a rotating connection.

7.1 Modelling and Simulation

The conceptualised spin sail was subject to differing passive and active deployment strategies. The deployment strategies used in passive deployment cases exerted no direct control over the boom deployment, but rather only had control over the satellite bus spin rate, and thus the resulting centrifugal force produced. The strategies investigated included passive deployment under cases of free body spin, centrifugal force limited deployment, controlled centrifugal force deployment and constant bus spin rate deployment. In order to achieve a passive deployment, damping was applied to the rotation of the pulley on which the booms are stowed, thus retarding their deployment rate.

Due to the flexible nature of the wire booms used in spin-sails there exists an in-plane offset angle of the booms during deployment. This angle was found to rapidly grow in the initial moments of deployment; the trend followed by this offset angle, for the remainder of the deployment process, depends on the deployment strategy used. A distinct feature of passive deployment is that the deployment rate is neither constant nor linear during the deployment process, unless the control is tailored there for, such as the case of constant centrifugal force control. This changing deployment rate affects how energy is distributed amongst the system elements, resulting in some interesting dynamics. Upon the completion of deployment the in-plane boom offset angle is recovered in an oscillatory manner, which induces oscillations in the satellite body. The boom oscillations may be small in angular amplitude but, considering the long lengths of solar sail booms, result in significant displacements of the boom tips. This displacement poses a threat to the fragile sail membrane, which can easily be damaged

and rendered ineffective. The possibility of stable deployment of a solar sail by passive means was shown to be a viable and simple alternative to an active means of deployment.

An active deployment case for a spinning solar sail was also investigated in simulation, where an actuator which could directly control the deployment rate of the booms was present. This is a means similar to that used by solar sails with semi-rigid booms, but for the key difference of how the deploying force is applied to the booms. To deploy a semi-rigid boom on a non-spinning satellite the booms are "pushed" out of the mechanism. In the case of a spin-sail, centrifugal force remains the driving force behind the deployment process and the actuator instead has the role of restraining the deployment process.

The effects of stowing long lengths of boom wire on a relatively small pulley on the deployment dynamics were incorporated into the simulation regimes. It was readily shown that in a passive deployment scenario, where the deployment is governed by the torques acting on the pulley, consideration should be given to how the booms unwind and the effects thereof on the deployment dynamics.

Several cases of unbalanced deployment were investigated which illustrated some of the behaviours that may be experienced in a practical deployment. Inconsistencies between physical boom parameters, how they are wound, and the occurrences in the first moments of deployment, and how these may effect the behaviour of the spacecraft as a whole were investigated. As the equations of motion which describe the system behaviour are highly sensitive to the initial conditions, the behaviour seen between the different unbalanced cases differ notably and prove to be unpredictable. An unbalanced deployment generally has the net result of exerting a force on the satellite body in the sail plane. This force would induce angular oscillatory motion of the spacecraft body both in and out of the sail-plane.

7.2 Experimental Passive Deployment

An experimental deployment mechanism was designed and constructed that made use of geared rotary dampers to achieve a passive deployment. This experiment practically validated the notion of passive boom deployment of a solar sail. Many of the dynamic trends seen in simulation were seen in the experimental results, such as the boom deployment profile. The presence of dynamic aspects which were not directly measured, such as the in-plane boom offset angle, were confirmed as the effects thereof could be seen. Particularly, the oscillations in the bus spin rate witnessed when control was released is a clear indicator of the presence of a significant in-plane boom oscillation.

The experimental tests faced several challenges, which shows the great difficulty of terrestrially testing a spinning solar sail deployment. The effects of gravity and the atmosphere play large roles and limit the possible scope of the tests significantly; because of these restraints the boom length which can be tested is severely limited and the notion of incorporating a sail membrane into the tests is almost impossible without the necessary large scale facilities.

During the experimental tests, in line with the simulations conducted, no direct control of the deployment rate was possible. The deployment process was managed entirely by the control of the bus spin rate. Under manual control and visual observation, the friction and damping present in the deployment mechanism could be characterised. A simple logic-based control algorithm was designed which had the ability, based only on information provided by the spin controller, to detect the state of the deployment process as well as react accordingly to ensure that the capabilities of the system components were not surpassed. This demonstrated that, even through simple means, the deployment state of the booms can be detected without any knowledge of the deployment mechanism state but for the output of the spin controller.

Insight was gained into the practical aspects of using a spinning solar sail deployment mechanism. Of particular note is the sensitivity to winding large lengths of boom wire into a

small volume. Inconsistent winding has many potential negative affects on how deployment proceeds. An even and consistent method of winding the booms was found to be crucial.

7.3 Deployment Mechanism Designs

Based upon the experience and practical knowledge gained from the experimental deployment tests, the design of the deployment mechanism could be refined and others proposed. Three deployment mechanism designs were presented: two passive and one active.

The passive designs function on the same principle as the experimental mechanism. Rotary dampers are used to limit the rotation rate of the pulley and thus that of the boom deployment. The first passive design is a direct evolution of the experimental deployment mechanism. It features the same layout and functional principle of using multiple geared dampers acting on a central pulley. The second passive design uses a single damper embedded within the pulley to better utilise the available volume. The use of a single larger damper does, however, require the mechanism's overall size to be slightly larger.

Finally, the active deployment mechanism design proposed takes advantage of the small pulley and low torque requirements, and uses the additional Tuna Can volume allowed by the CubeSat standard to house the majority of the deployment mechanism. The deployment is actuated by a geared DC motor with high internal friction to control the deployment rate. The high gear ratio and friction prevents the motor from being back driven. A minimal amount of torque input is thus required to control the deployment process.

7.4 Future Development

A sufficient dynamic model of the solar sail boom deployment has been constructed, which presents the dynamic trends during deployment. The theoretical model can, however, be further expanded to include the effects of the sail membrane. This would prove to be useful in observing how the sail membrane behaves, and would assist in developing relations by which allowable deployment rates, the minimum centrifugal force and boom offset angles may be defined. It may also provide insight into the real damping and inertial effects of the sail membrane on the boom dynamics during deployment. Such a study could be conducted by the use of Finite Element Analysis (FEM), but this method may prove a challenging path as the number of simulated nodes would need to be constantly increased, or the distance between nodes increased, as deployment progresses. The dynamic model may also be expanded to include out-of-plane dynamics; including these would prove particularly useful in the study of the effects of an unbalanced deployment on the spacecraft body.

Extensive testing, particularly thermal, vacuum and vibration testing, needs to be conducted on the COTS components included in the deployment mechanism designs in order to determine their suitability for space based applications. The focus of the hardware testing was limited to the boom deployment, though there are many other aspects to explore such as the sail membrane stowage and extraction, and how this affects the forces involved in deployment. Further focus may too be placed on measuring the boom offset angle. An experiment may be devised to focus on this aspect where the sacrifices in others may not be so detrimental to the broader aim of the experiment. Further testing may need to be conducted, on both a component and assembly level, to determine and better model the friction forces involved between various mating surfaces.

Estimations techniques may be developed, which could not only estimate the deployment stage but also the deployed length based on the motor and controller behaviour. By using the motor input power, the torque applied can be estimated, and thus the load moment of inertia may also be estimated. This may allow the deployed length to be reasonably accurately known, with little to no direct knowledge of the deployment state.

The theoretical dynamics developed here may be easily applied to spinning, flexible deployable structures in space, such as scientific instruments, and the mechanisms developed can be used in applications such as drag sails.

Appendix A

Lagrangian Mechanics Derivation Algorithm

Algorithm 1 Lagrangian Mechanics: Derivation of Equations of Motion

1: **procedure** DERIVEEoM($BOOMS = n$, $INERTIAL$, $DEPLOYING$)

Phase 1 – Determine Element Positions and Velocities

```

2:   if  $INERTIAL$  then                                     ▷ Define bus centre position
3:        $\mathbf{P} = [P_x \ P_y]^T$ 
4:   else
5:        $\mathbf{P} = [0 \ 0]^T$ 
6:   end if
7:    $\dot{\mathbf{P}} = \dot{P}_x \cdot \text{diff}(\mathbf{P}, P_x) + \dot{P}_y \cdot \text{diff}(\mathbf{P}, P_y)$ 
8:
9:   for  $i \leftarrow 1, n$  do                                   ▷ Boom Tip Positions
10:       $\mathbf{r}_i = \begin{bmatrix} r \cos(\beta + \frac{2\pi}{n}(i-1)) + \ell_i \cos(\beta + \theta_i + \frac{2\pi}{n}(i-1)) \\ r \sin(\beta + \frac{2\pi}{n}(i-1)) + \ell_i \sin(\beta + \theta_i + \frac{2\pi}{n}(i-1)) \end{bmatrix}$ 
11:   end for
12:
13:   for  $i \leftarrow 1, n$  do                                   ▷ Boom Tip Velocities
14:       $\mathbf{v}_i = \dot{P}_x \cdot \text{diff}(\mathbf{r}_i, P_x) + \dot{P}_y \cdot \text{diff}(\mathbf{r}_i, P_y) + \dot{\beta} \cdot \text{diff}(\mathbf{r}_i, \beta) + \dot{\theta}_i \cdot \text{diff}(\mathbf{r}_i, \theta_i)$ 
15:      if  $DEPLOYING$  then
16:           $\mathbf{v}_i += \dot{\ell}_i \cdot \text{diff}(\mathbf{r}_i, \ell_i)$ 
17:      end if
18:   end for

```

Phase 2 – System Energies

```

19:    $T = \frac{1}{2}m_b \|\dot{\mathbf{P}}\|^2 + \frac{1}{2}I_b \|\dot{\beta}\|^2 + \sum_{i=1}^n \frac{1}{2}m_i \|\mathbf{v}_i\|^2$            ▷ Kinetic Energy
20:    $U = 0$                                                    ▷ Potential Energy
21:    $R = -\sum_{i=1}^n \frac{1}{2}b \|\dot{\theta}_i\|^2$                              ▷ Rayleigh Dissipation

```

<i>Phase 3 – Solve Euler-Lagrange Equations</i>	
22:	$\mathcal{L} = T - U$
23:	if <i>INERTIAL</i> then
24:	$EL_{P_x} = \text{solveEL}(\mathcal{L}, R, P_x, \dot{P}_x)$
25:	$EL_{P_y} = \text{solveEL}(\mathcal{L}, R, P_y, \dot{P}_y)$
26:	else
27:	$EL_{P_x} = 0$
28:	$EL_{P_y} = 0$
29:	end if
30:	$EL_{\beta} = \text{solveEL}(\mathcal{L}, R, \beta, \dot{\beta})$
31:	for $i \leftarrow 1, n$ do
32:	$EL_{\theta_i} = \text{solveEL}(\mathcal{L}, R, \theta_i, \dot{\theta}_i)$
33:	if <i>DEPLOYING</i> then
34:	$EL_{\ell_i} = \text{solveEL}(\mathcal{L}, R, \ell_i, \dot{\ell}_i)$
35:	else
36:	$EL_{\ell_i} = 0$
37:	end if
38:	end for
<i>Phase 4 – Decouple to Obtain Equations of Motion</i>	
39:	$EoM = \text{solve}([EL_{P_x}, EL_{P_y}, EL_{\beta}, EL_{\theta_1}, \dots, EL_{\theta_n}, EL_{\ell_1}, \dots, EL_{\ell_n}], \dots$
40:	$[\ddot{P}_x, \ddot{P}_y, \ddot{\beta}, \ddot{\theta}_1, \dots, \ddot{\theta}_n, \ddot{\ell}_1, \dots, \ddot{\ell}_n])$
41:	
42:	for $i \leftarrow 1, 3 + 2 \cdot n$ do ▷ Simplify the equations
43:	$EoM(i) = \text{simplify}(EoM(i))$
44:	end for
<i>Phase 5 – Write Equations of Motion as Function and Save to File</i>	
<p>The symbolic equations of motion are each subjected to a string replacing process which converts then to character strings, replaces the symbolic variables with those used in simulation and finally writes them, correctly formatted, to an executable function file which can be run from simulation. The function file is always structured the same way, regardless of input options, in that which ever configuration is used the same input and outputs arguments can be used. For instance when not investigating the inertial case the function returns a zero for \ddot{P}_x and \ddot{P}_y. This allows the same simulation code to be easily configurable to differing input cases.</p>	
45:	end procedure
<i>Supporting Functions</i>	
46:	function SOLVEEL($\mathcal{L}, R, p, \dot{p}$)
47:	$bar = \frac{\partial \mathcal{L}}{\partial \dot{p}} = \text{diff}(\mathcal{L}, \dot{p})$
48:	$Fus = \frac{d}{dt} \left(\frac{\partial \mathcal{L}}{\partial \dot{\theta}} \right) = \ddot{P}_x \cdot \text{diff}(foo, \dot{P}_x) + \dot{P}_x \cdot \text{diff}(foo, P_x) + \ddot{P}_y \cdot \text{diff}(foo, \dot{P}_y) + \dot{P}_y \cdot \text{diff}(foo, P_y) + \ddot{\beta} \cdot \text{diff}(foo, \dot{\beta}) + \dot{\beta} \cdot \text{diff}(foo, \beta) + \ddot{\theta}_1 \cdot \text{diff}(foo, \dot{\theta}_1) + \dots + \ddot{\theta}_n \cdot \text{diff}(foo, \dot{\theta}_n) + \dot{\theta}_1 \cdot \text{diff}(foo, \theta_1) + \dots + \dot{\theta}_n \cdot \text{diff}(foo, \theta_n)$
49:	if <i>DEPLOYING</i> then
50:	$Fus += \dot{\ell}_1 \cdot \text{diff}(foo, \ell_1) + \dots + \dot{\ell}_n \cdot \text{diff}(foo, \ell_n)$
51:	end if
52:	$Roh = \frac{\partial \mathcal{L}}{\partial p} = \text{diff}(\mathcal{L}, p)$
53:	$Da = \frac{\partial R}{\partial \dot{p}} = \text{diff}(R, \dot{p})$
54:	$EL = Fus - Roh - Da$
55:	$EL = \text{Simplify}(EL)$
56:	return EL
57:	end function

Appendix B

Equations of Motion

B.1 Single Boom Dynamics

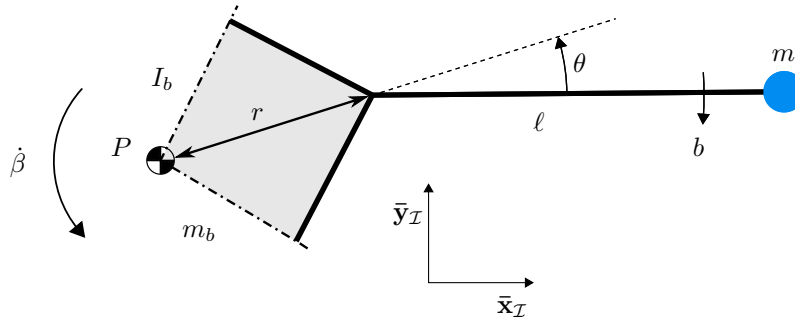


Figure B.1: Single Boom System

B.1.1 Single Boom non-Deploying

$$\ddot{\beta} = \frac{bl\dot{\theta} + br\dot{\theta}\cos(\theta) + \dot{\beta}^2\ell^2mr\sin(\theta) + \ell^2mr\dot{\theta}^2\sin(\theta) + \dot{\beta}^2\ell mr^2\cos(\theta)\sin(\theta) + 2\dot{\beta}\ell^2mr\dot{\theta}\sin(\theta)}{\ell(I_b + mr^2 - mr^2\cos(\theta)^2)} \quad (\text{B.1.1})$$

$$\ddot{\theta}_1 = -\frac{I_b b\dot{\theta} + bl^2m\dot{\theta} + bmr^2\dot{\theta} + \dot{\beta}^2\ell m^2r^3\sin(\theta) + \dot{\beta}^2\ell^3m^2r\sin(\theta) + \ell^3m^2r\dot{\theta}^2\sin(\theta) + \dot{\beta}^2\ell^2m^2r^2\sin(2\theta) + \frac{1}{2}(\ell^2m^2r^2\dot{\theta}^2\sin(2\theta)) + 2\dot{\beta}\ell^3m^2r\dot{\theta}\sin(\theta) + 2blmr\dot{\theta}\cos(\theta) + I_b\dot{\beta}^2\ell mr\sin(\theta) + \dot{\beta}\ell^2m^2r^2\dot{\theta}\sin(2\theta)}{\ell^2m(I_b + \frac{1}{2}(mr^2 - mr^2\cos(2\theta)))} \quad (\text{B.1.2})$$

B.1.2 Single Boom Freely Deploying

$$\ddot{\beta} = \frac{b\dot{\theta}(\ell + r\cos(\theta))}{I_b\ell} \quad (\text{B.1.3})$$

$$\ddot{\theta} = -\frac{I_b b \dot{\theta} + b \ell^2 m \dot{\theta} + 2I_b \dot{\beta} \ell m + 2I_b \ell \dot{m} \dot{\theta} + b m r^2 \dot{\theta} \cos(\theta)^2 + 2b \ell m r \dot{\theta} \cos(\theta) + I_b \dot{\beta}^2 \ell m r \sin(\theta)}{I_b \ell^2 m} \quad (\text{B.1.4})$$

$$\ddot{\ell} = \frac{I_b \dot{\beta}^2 \ell^2 + I_b \ell^2 \dot{\theta}^2 + 2I_b \dot{\beta} \ell^2 \dot{\theta} + I_b \dot{\beta}^2 \ell r \cos(\theta) - b r^2 \dot{\theta} \cos(\theta) \sin(\theta) - b \ell r \dot{\theta} \sin(\theta)}{I_b \ell} \quad (\text{B.1.5})$$

B.1.3 Single Boom Controlled Deployment

$$\ddot{\beta} = \frac{b \ell \dot{\theta} + b r \dot{\theta} \cos(\theta) + \dot{\beta}^2 \ell^2 m r \sin(\theta) + \ell^2 m r \dot{\theta}^2 \sin(\theta) - \ell \dot{m} r \sin(\theta) + \dot{\beta}^2 \ell m r^2 \cos(\theta) \sin(\theta) + 2\dot{\beta} \ell^2 m r \dot{\theta} \sin(\theta)}{\ell(I_b + m r^2 - m r^2 \cos(\theta)^2)} \quad (\text{B.1.6})$$

$$\ddot{\theta} = -\frac{I_b b \dot{\theta} + b \ell^2 m \dot{\theta} + b m r^2 \dot{\theta} + \dot{\beta}^2 \ell m^2 r^3 \sin(\theta) + \dot{\beta}^2 \ell^3 m^2 r \sin(\theta) - \frac{1}{2}(\ell \dot{m}^2 r^2 \sin(2\theta)) + \ell^3 m^2 r \dot{\theta}^2 \sin(\theta) + \dot{\beta} \ell m^2 r^2 + \ell m^2 r^2 \dot{\theta} + 2I_b \dot{\beta} \ell m + 2I_b \ell \dot{m} \dot{\theta} - \ell^2 \dot{m}^2 r \sin(\theta) + \dot{\beta}^2 \ell^2 m^2 r^2 \sin(2\theta) + \frac{1}{2}(\ell^2 m^2 r^2 \dot{\theta}^2 \sin(2\theta)) + 2\dot{\beta} \ell^3 m^2 r \dot{\theta} \sin(\theta) + 2b \ell m r \dot{\theta} \cos(\theta) - \dot{\beta} \ell m^2 r^2 \cos(2\theta) - \ell \dot{m}^2 r^2 \dot{\theta} \cos(2\theta) + I_b \dot{\beta}^2 \ell m r \sin(\theta) + \dot{\beta} \ell^2 m^2 r^2 \dot{\theta} \sin(2\theta)}{\ell^2 m(I_b + \frac{1}{2}(m r^2) - \frac{1}{2}(m r^2 \cos(2\theta)))} \quad (\text{B.1.7})$$

$$\ddot{\ell} = \dot{\beta}^2 \ell + \ell \dot{\theta}^2 - \dot{\beta} r \sin(\theta) + \dot{\beta}^2 r \cos(\theta) + 2\dot{\beta} \ell \dot{\theta} \quad (\text{B.1.8})$$

B.2 Two Booms Dynamics

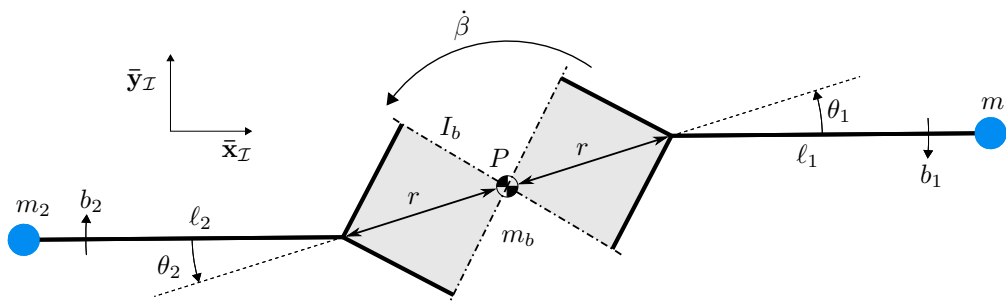


Figure B.2: Two Boom System

B.2.1 Two Booms non-Deploying

$$\ddot{\beta} = \frac{b \ell_1 \ell_2 \dot{\theta}_1 + b \ell_1 \ell_2 \dot{\theta}_2 + b \ell_2 r \dot{\theta}_1 \cos(\theta_1) + b \ell_1 r \dot{\theta}_2 \cos(\theta_2) + \dot{\beta}^2 \ell_1^2 \ell_2 m_1 r \sin(\theta_1) + \dot{\beta}^2 \ell_1 \ell_2^2 m_2 r \sin(\theta_2) + \ell_1^2 \ell_2 m_1 r \dot{\theta}_1^2 \sin(\theta_1) + \ell_1 \ell_2^2 m_2 r \dot{\theta}_2^2 \sin(\theta_2) + \frac{1}{2}(\dot{\beta}^2 \ell_1 \ell_2 m_1 r^2 \sin(2\theta_1)) + \frac{1}{2}(\dot{\beta}^2 \ell_1 \ell_2 m_2 r^2 \sin(2\theta_2)) + 2\dot{\beta} \ell_1^2 \ell_2 m_1 r \dot{\theta}_1 \sin(\theta_1) + 2\dot{\beta} \ell_1 \ell_2^2 m_2 r \dot{\theta}_2 \sin(\theta_2)}{\ell_1 \ell_2 (I_b + m_1 r^2 + m_2 r^2 - m_1 r^2 \cos(\theta_1)^2 - m_2 r^2 \cos(\theta_2)^2)} \quad (\text{B.2.1})$$

$$\begin{aligned}
& I_b b \ell_2 \dot{\theta}_1 + b \ell_1^2 \ell_2 m_1 \dot{\theta}_1 + b \ell_1^2 \ell_2 m_1 \dot{\theta}_2 + b \ell_2 m_1 r^2 \dot{\theta}_1 + b \ell_2 m_2 r^2 \dot{\theta}_1 \\
& - b \ell_2 m_2 r^2 \dot{\theta}_1 \cos(\theta_2)^2 + \dot{\beta}^2 \ell_1^2 \ell_2 m_1^2 r^2 \sin(2\theta_1) + \frac{1}{2} (\ell_1^2 \ell_2 m_1^2 r^2 \dot{\theta}_1^2 \sin(2\theta_1)) \\
& + \dot{\beta}^2 \ell_1 \ell_2 m_1^2 r^3 \sin(\theta_1) + \dot{\beta}^2 \ell_1^3 \ell_2 m_1^2 r \sin(\theta_1) + \ell_1^3 \ell_2 m_1^2 r \dot{\theta}_1^2 \sin(\theta_1) \\
& + b \ell_1^2 m_1 r \dot{\theta}_2 \cos(\theta_2) + I_b \dot{\beta}^2 \ell_1 \ell_2 m_1 r \sin(\theta_1) + \frac{1}{2} (\dot{\beta}^2 \ell_1^2 \ell_2 m_1 m_2 r^2 \sin(2\theta_2)) \\
& + \dot{\beta} \ell_1^2 \ell_2 m_1^2 r^2 \dot{\theta}_1 \sin(2\theta_1) + \dot{\beta}^2 \ell_1 \ell_2 m_1 m_2 r^3 \sin(\theta_1) + b \ell_1 m_1 r^2 \dot{\theta}_2 \cos(\theta_1) \cos(\theta_2) \\
& + 2 \dot{\beta} \ell_1^3 \ell_2 m_1^2 r \dot{\theta}_1 \sin(\theta_1) + 2 b \ell_1 \ell_2 m_1 r \dot{\theta}_1 \cos(\theta_1) + b \ell_1 \ell_2 m_1 r \dot{\theta}_2 \cos(\theta_1) \\
& + \dot{\beta}^2 \ell_1^2 \ell_2^2 m_1 m_2 r \sin(\theta_2) + \ell_1^2 \ell_2^2 m_1 m_2 r \dot{\theta}_2^2 \sin(\theta_2) + 2 \dot{\beta} \ell_1^2 \ell_2^2 m_1 m_2 r \dot{\theta}_2 \sin(\theta_2) \\
& + \dot{\beta}^2 \ell_1 \ell_2^2 m_1 m_2 r^2 \cos(\theta_1) \sin(\theta_2) - \dot{\beta}^2 \ell_1 \ell_2 m_1 m_2 r^3 \cos(\theta_2)^2 \sin(\theta_1) \\
& + \ell_1 \ell_2^2 m_1 m_2 r^2 \dot{\theta}_2^2 \cos(\theta_1) \sin(\theta_2) + \dot{\beta}^2 \ell_1 \ell_2 m_1 m_2 r^3 \cos(\theta_1) \cos(\theta_2) \sin(\theta_2) \\
& + 2 \dot{\beta} \ell_1 \ell_2^2 m_1 m_2 r^2 \dot{\theta}_2 \cos(\theta_1) \sin(\theta_2)
\end{aligned}$$

$$\ddot{\theta}_1 = - \frac{\ell_1^2 \ell_2 m_1 (I_b + m_1 r^2 + m_2 r^2 - m_1 r^2 \cos(\theta_1)^2 - m_2 r^2 \cos(\theta_2)^2)}{\ell_1^2 \ell_2 m_1 (I_b + m_1 r^2 + m_2 r^2 - m_1 r^2 \cos(\theta_1)^2 - m_2 r^2 \cos(\theta_2)^2)} \quad (\text{B.2.2})$$

$$\begin{aligned}
& I_b b \ell_1 \dot{\theta}_2 + b \ell_1 \ell_2^2 m_2 \dot{\theta}_1 + b \ell_1 \ell_2^2 m_2 \dot{\theta}_2 + b \ell_1 m_1 r^2 \dot{\theta}_2 + b \ell_1 m_2 r^2 \dot{\theta}_2 \\
& - b \ell_1 m_1 r^2 \dot{\theta}_2 \cos(\theta_1)^2 + \dot{\beta}^2 \ell_1 \ell_2^2 m_2^2 r^2 \sin(2\theta_2) + \frac{1}{2} (\ell_1 \ell_2^2 m_2^2 r^2 \dot{\theta}_2^2 \sin(2\theta_2)) \\
& + \dot{\beta}^2 \ell_1 \ell_2 m_2^2 r^3 \sin(\theta_2) + \dot{\beta}^2 \ell_1 \ell_2^2 m_2^2 r \sin(\theta_2) + \ell_1 \ell_2^2 m_2^2 r \dot{\theta}_2^2 \sin(\theta_2) \\
& + b \ell_2^2 m_2 r \dot{\theta}_1 \cos(\theta_1) + I_b \dot{\beta}^2 \ell_1 \ell_2 m_2 r \sin(\theta_2) + \frac{1}{2} (\dot{\beta}^2 \ell_1 \ell_2^2 m_1 m_2 r^2 \sin(2\theta_1)) \\
& + \dot{\beta} \ell_1 \ell_2^2 m_2^2 r^2 \dot{\theta}_2 \sin(2\theta_2) + \dot{\beta}^2 \ell_1 \ell_2 m_1 m_2 r^3 \sin(\theta_2) + b \ell_2 m_2 r^2 \dot{\theta}_1 \cos(\theta_1) \cos(\theta_2) \\
& + 2 \dot{\beta} \ell_1 \ell_2^2 m_2^2 r \dot{\theta}_2 \sin(\theta_2) + b \ell_1 \ell_2 m_2 r \dot{\theta}_1 \cos(\theta_2) + 2 b \ell_1 \ell_2 m_2 r \dot{\theta}_2 \cos(\theta_2) \\
& + \dot{\beta}^2 \ell_1^2 \ell_2^2 m_1 m_2 r \sin(\theta_1) + \ell_1^2 \ell_2^2 m_1 m_2 r \dot{\theta}_1^2 \sin(\theta_1) + 2 \dot{\beta} \ell_1^2 \ell_2^2 m_1 m_2 r \dot{\theta}_1 \sin(\theta_1) \\
& + \dot{\beta}^2 \ell_1^2 \ell_2 m_1 m_2 r^2 \cos(\theta_2) \sin(\theta_1) - \dot{\beta}^2 \ell_1 \ell_2 m_1 m_2 r^3 \cos(\theta_1)^2 \sin(\theta_2) \\
& + \ell_1^2 \ell_2 m_1 m_2 r^2 \dot{\theta}_1^2 \cos(\theta_2) \sin(\theta_1) + \dot{\beta}^2 \ell_1 \ell_2 m_1 m_2 r^3 \cos(\theta_1) \cos(\theta_2) \sin(\theta_1) \\
& + 2 \dot{\beta} \ell_1^2 \ell_2 m_1 m_2 r^2 \dot{\theta}_1 \cos(\theta_2) \sin(\theta_1)
\end{aligned}$$

$$\ddot{\theta}_1 = - \frac{\ell_1 \ell_2^2 m_2 (I_b + m_1 r^2 + m_2 r^2 - m_1 r^2 \cos(\theta_1)^2 - m_2 r^2 \cos(\theta_2)^2)}{\ell_1 \ell_2^2 m_2 (I_b + m_1 r^2 + m_2 r^2 - m_1 r^2 \cos(\theta_1)^2 - m_2 r^2 \cos(\theta_2)^2)} \quad (\text{B.2.3})$$

B.2.2 Two Booms Freely Deploying

$$\ddot{\beta} = b \frac{\ell_1 \ell_2 \dot{\theta}_1 + \ell_1 \ell_2 \dot{\theta}_2 + \ell_2 r \dot{\theta}_1 \cos(\theta_1) + \ell_1 r \dot{\theta}_2 \cos(\theta_2)}{I_b \ell_1 \ell_2} \quad (\text{B.2.4})$$

$$\begin{aligned}
& I_b b \ell_2 \dot{\theta}_1 + b \ell_1^2 \ell_2 m_1 \dot{\theta}_1 + b \ell_1^2 \ell_2 m_1 \dot{\theta}_2 + b \ell_2 m_1 r^2 \dot{\theta}_1 \cos(\theta_1)^2 + b \ell_1^2 m_1 r \dot{\theta}_2 \cos(\theta_2) \\
& + 2 I_b \dot{\beta} \ell_1 \ell_2 \dot{\ell}_1 m_1 + 2 I_b \ell_1 \ell_2 \dot{\ell}_1 m_1 \dot{\theta}_1 + I_b \dot{\beta}^2 \ell_1 \ell_2 m_1 r \sin(\theta_1) \\
& + b \ell_1 m_1 r^2 \dot{\theta}_2 \cos(\theta_1) \cos(\theta_2) + 2 b \ell_1 \ell_2 m_1 r \dot{\theta}_1 \cos(\theta_1) + b \ell_1 \ell_2 m_1 r \dot{\theta}_2 \cos(\theta_1)
\end{aligned}$$

$$\ddot{\theta}_1 = - \frac{I_b \ell_1^2 \ell_2 m_1}{I_b \ell_1^2 \ell_2 m_1} \quad (\text{B.2.5})$$

$$\begin{aligned}
& I_b b \ell_1 \dot{\theta}_2 + b \ell_1 \ell_2^2 m_2 \dot{\theta}_1 + b \ell_1 \ell_2^2 m_2 \dot{\theta}_2 + b \ell_1 m_2 r^2 \dot{\theta}_2 \cos(\theta_2)^2 + b \ell_2^2 m_2 r \dot{\theta}_1 \cos(\theta_1) \\
& + 2 I_b \dot{\beta} \ell_1 \ell_2 \dot{\ell}_2 m_2 + 2 I_b \ell_1 \ell_2 \dot{\ell}_2 m_2 \dot{\theta}_2 + I_b \dot{\beta}^2 \ell_1 \ell_2 m_2 r \sin(\theta_2) \\
& + b \ell_2 m_2 r^2 \dot{\theta}_1 \cos(\theta_1) \cos(\theta_2) + b \ell_1 \ell_2 m_2 r \dot{\theta}_1 \cos(\theta_2) + 2 b \ell_1 \ell_2 m_2 r \dot{\theta}_2 \cos(\theta_2)
\end{aligned}$$

$$\ddot{\theta}_2 = - \frac{I_b \ell_1 \ell_2^2 m_2}{I_b \ell_1 \ell_2^2 m_2} \quad (\text{B.2.6})$$

$$\begin{aligned}
& I_b \dot{\beta}^2 \ell_1^2 \ell_2 + I_b \ell_2^2 \ell_2 \dot{\theta}_1^2 + 2 I_b \dot{\beta} \ell_1^2 \ell_2 \dot{\theta}_1 - b \ell_2 r^2 \dot{\theta}_1 \cos(\theta_1) \sin(\theta_1) \\
& - b \ell_1 r^2 \dot{\theta}_2 \cos(\theta_2) \sin(\theta_1) - b \ell_1 \ell_2 r \dot{\theta}_1 \sin(\theta_1) - b \ell_1 \ell_2 r \dot{\theta}_2 \sin(\theta_1) + I_b \dot{\beta}^2 \ell_1 \ell_2 r \cos(\theta_1)
\end{aligned}$$

$$\ddot{\ell}_1 = \frac{I_b \ell_1 \ell_2}{I_b \ell_1 \ell_2} \quad (\text{B.2.7})$$

$$\ddot{\ell}_2 = \frac{I_b \dot{\beta}^2 \ell_1 \ell_2^2 + I_b \ell_1 \ell_2^2 \dot{\theta}_2^2 + 2I_b \dot{\beta} \ell_1 \ell_2^2 \dot{\theta}_2 - b \ell_2 r^2 \dot{\theta}_1 \cos(\theta_1) \sin(\theta_2) - b \ell_1 r^2 \dot{\theta}_2 \cos(\theta_2) \sin(\theta_2) - b \ell_1 \ell_2 r \dot{\theta}_1 \sin(\theta_2) - b \ell_1 \ell_2 r \dot{\theta}_2 \sin(\theta_2) + I_b \dot{\beta}^2 \ell_1 \ell_2 r \cos(\theta_2)}{I_b \ell_1 \ell_2} \quad (\text{B.2.8})$$

B.2.3 Two Booms Freely Deploying in Inertial Space

$$\ddot{P}_x = -b \frac{\ell_2 \dot{\theta}_1 \sin(\beta + \theta_1) - \ell_1 \dot{\theta}_2 \sin(\beta + \theta_2)}{m_b \ell_1 \ell_2} \quad (\text{B.2.9})$$

$$\ddot{P}_y = b \frac{\ell_2 \dot{\theta}_1 \cos(\beta + \theta_1) - \ell_1 \dot{\theta}_2 \cos(\beta + \theta_2)}{m_b \ell_1 \ell_2} \quad (\text{B.2.10})$$

$$\ddot{\beta} = b \frac{\ell_1 \ell_2 \dot{\theta}_1 + \ell_1 \ell_2 \dot{\theta}_2 + \ell_2 r \dot{\theta}_1 \cos(\theta_1) + \ell_1 r \dot{\theta}_2 \cos(\theta_2)}{m_b \ell_1 \ell_2 r^2} \quad (\text{B.2.11})$$

$$\ddot{\theta}_1 = - \frac{m_b b \ell_2 r^2 \dot{\theta}_1 + b \ell_1^2 \ell_2 m_1 \dot{\theta}_1 + b \ell_1^2 \ell_2 m_1 \dot{\theta}_2 + b \ell_2 m_1 r^2 \dot{\theta}_1 + b \ell_2 m_1 r^2 \dot{\theta}_1 \cos(\theta_1)^2 + b \ell_1^2 m_1 r \dot{\theta}_2 \cos(\theta_2) + m_b \dot{\beta}^2 \ell_1 \ell_2 m_1 r^3 \sin(\theta_1) + 2m_b \dot{\beta} \ell_1 \ell_2 \ell_1 m_1 r^2 + 2m_b \ell_1 \ell_2 \dot{\ell}_1 m_1 r^2 \dot{\theta}_1 - b \ell_1 m_1 r^2 \dot{\theta}_2 \sin(\theta_1) \sin(\theta_2) + 2b \ell_1 \ell_2 m_1 r \dot{\theta}_1 \cos(\theta_1) + b \ell_1 \ell_2 m_1 r \dot{\theta}_2 \cos(\theta_1)}{m_b \ell_1^2 \ell_2 m_1 r^2} \quad (\text{B.2.12})$$

$$\ddot{\theta}_2 = - \frac{m_b b \ell_1 r^2 \dot{\theta}_2 + b \ell_1 \ell_2^2 m_2 \dot{\theta}_1 + b \ell_1 \ell_2^2 m_2 \dot{\theta}_2 + b \ell_1 m_2 r^2 \dot{\theta}_2 + b \ell_1 m_2 r^2 \dot{\theta}_2 \cos(\theta_2)^2 + b \ell_2^2 m_2 r \dot{\theta}_1 \cos(\theta_1) + m_b \dot{\beta}^2 \ell_1 \ell_2 m_2 r^3 \sin(\theta_2) + 2m_b \dot{\beta} \ell_1 \ell_2 \ell_2 m_2 r^2 + 2m_b \ell_1 \ell_2 \dot{\ell}_2 m_2 r^2 \dot{\theta}_2 - b \ell_2 m_2 r^2 \dot{\theta}_1 \sin(\theta_1) \sin(\theta_2) + b \ell_1 \ell_2 m_2 r \dot{\theta}_1 \cos(\theta_2) + 2b \ell_1 \ell_2 m_2 r \dot{\theta}_2 \cos(\theta_2)}{m_b \ell_1 \ell_2^2 m_2 r^2} \quad (\text{B.2.13})$$

$$\ddot{\ell}_1 = \frac{m_b \dot{\beta}^2 \ell_1^2 \ell_2 r + m_b \ell_1^2 \ell_2 r \dot{\theta}_1^2 - b \ell_1 \ell_2 \dot{\theta}_1 \sin(\theta_1) - b \ell_1 \ell_2 \dot{\theta}_2 \sin(\theta_1) + 2m_b \dot{\beta} \ell_1^2 \ell_2 r \dot{\theta}_1 - b \ell_2 r \dot{\theta}_1 \cos(\theta_1) \sin(\theta_1) - b \ell_1 r \dot{\theta}_2 \cos(\theta_1) \sin(\theta_2) + m_b \dot{\beta}^2 \ell_1 \ell_2 r^2 \cos(\theta_1)}{m_b \ell_1 \ell_2 r} \quad (\text{B.2.14})$$

$$\ddot{\ell}_2 = \frac{m_b \dot{\beta}^2 \ell_1 \ell_2^2 r + m_b \ell_1 \ell_2^2 r \dot{\theta}_2^2 - b \ell_1 \ell_2 \dot{\theta}_1 \sin(\theta_2) - b \ell_1 \ell_2 \dot{\theta}_2 \sin(\theta_2) + 2m_b \dot{\beta} \ell_1 \ell_2^2 r \dot{\theta}_2 - b \ell_2 r \dot{\theta}_1 \cos(\theta_2) \sin(\theta_1) - b \ell_1 r \dot{\theta}_2 \cos(\theta_2) \sin(\theta_2) + m_b \dot{\beta}^2 \ell_1 \ell_2 r^2 \cos(\theta_2)}{m_b \ell_1 \ell_2 r} \quad (\text{B.2.15})$$

Bibliography

- [1] Fu, B., Sperber, E. and Eke, F.: Solar sail technology - A state of the art review. *Progress in Aerospace Sciences*, vol. 86, pp. 1–19, 2016. ISSN 03760421.
Available at:
<http://www.sciencedirect.com/science/article/pii/S0376042116300100>
- [2] Wright, J.L.: *Space Sailing*. Gordon and Breach Science Publishers S.A., Philadelphia, USA, 1992. ISBN 2-88124-803-9.
- [3] O’Shaughnessy, D.J., McAdams, J.V., Williams, K.E. and Page, B.R.: Fire Sail: MESSENGER’s use of Solar Radiation Pressure for Accurate Mercury Flybys. *Advances in the Astronautical Sciences*, vol. 133, no. 1, pp. 1–16, 2009.
Available at:
<http://messenger.jhuapl.edu/the{ }mission/publications/AAS09-014.pdf>
- [4] McInnes, C.R.: *Solar Sailing: Technology, Dynamics and Mission Applications*. Praxis Publishing Ltd, Chichester, UK, 1999. ISBN 3540210628.
- [5] McInnes, C.R.: Solar sailing : mission applications and engineering challenges. *Philosophical Transactions of the Royal Society of London A: Mathematical, Physical and Engineering Sciences*, vol. 361, no. 1813, pp. 2989–3008, 2003.
Available at: <http://rsta.royalsocietypublishing.org/content/361/1813/2989>
- [6] Betts, B., Nye, B., Vaughn, J., Greeson, E., Chute, R., Spencer, D.A., Ridenoure, R.W., Munakata, R., Wong, S.D., Diaz, A., Stetson, D.A., Foley, J.D., Bellardo, J.M. and Plante, B.A.: LightSail 1 Mission Results and Public Outreach Strategies. In: *4th International Symposium on Solar Sailing*. Kyoto, Japan, 2017.
- [7] Johnson, L., Castillo-Rogez, J., Dervan, J. and McNutt, L.: Near Earth Asteroid Scout Mission. In: *4th International Symposium on Solar Sailing*. Kyoto, Japan, 2017.
Available at: <http://www.lpi.usra.edu/sbag/meetings/jul2014/presentations/0930{ }Thu{ }Castillo{ }NEAScout.pdf>
- [8] Price, H., Ayon, J., Buehler, M., Garner, C., Klose, G., Mettler, E., Nakazono, B. and Sprague, G.: Design for a solar sail demonstration mission. Tech. Rep., Jet Propulsion Laboratory, California Institute of Technology, 2001.
Available at:
<http://trs-new.jpl.nasa.gov/dspace/bitstream/2014/12303/1/01-0335.pdf>
- [9] Wie, B.: Solar Sail Attitude Control and Dynamics, Part 1. *Journal of Guidance, Control, and Dynamics*, vol. 27, no. 4, pp. 526–535, 2004. ISSN 0731-5090.
Available at: <http://arc.aiaa.org/doi/10.2514/1.11134>
- [10] Bidy, C. and Svitek, T.: LightSail-1 Solar Sail Design and Qualification. *Proceedings of the 41st Aerospace Mechanisms Symposium*, pp. 451–463, 2012.

- [11] Parera, P.M.: *Deployment Simulations of a Composite Boom for Small Satellites*. Ph.D. thesis, Royal Institute of Technology, SE-100 44 Stockholm, Sweden, 2013.
- [12] Furuya, H., Sakamoto, H., Satou, Y., Yokomatsu, T., Yashima, K., Chubachi, T. and Akihito, W.: Boom / Membrane Integrated Deployable Space Structures for Small Satellites. In: *4th International Symposium on Solar Sailing*, pp. 28–31. Kyoto, Japan, 2017.
- [13] Fernandez, J.M.: Advanced Deployable Shell-Based Composite Booms For Small Satellite Structural Applications Including Solar Sails. In: *4th International Symposium on Solar Sailing*, vol. 1. Kyoto, Japan, 2017.
- [14] Chubachi, T., Hiroshi, F. and Akihito, W.: Hybrid Self-deployable Tubular CFRP Booms for Deployable Membrane. In: *4th International Symposium on Solar Sailing*. Kyoto, Japan, 2017.
- [15] Sznajder, M., Geppert, U. and Arc, M.M.: Degradation of thin solar-sail membrane films under interplanetary medium. In: *4th International Symposium on Solar Sailing*, pp. 1–6. Kyoto, Japan, 2017.
- [16] Mori, O., Shirasawa, Y., Miyazaki, Y., Sakamoto, H., Hasome, M., Okuizumi, N., Sawada, H., Furuya, H., Matunaga, S., Natori, M., Tsuda, Y., Saiki, T., Funase, R., Mimasu, Y. and Kawaguchi, J.: Deployment and steering dynamics of spinning solar sail "IKAROS". *Journal of Aerospace Engineering, Sciences and Applications*, vol. 4, no. 4, pp. 79–96, 2012. ISSN 2236577X.
- [17] Mori, O., Sawada, H., Funase, R., Endo, T., Morimoto, M., Yamamoto, T., Tsuda, Y., Kawakatsu, Y. and Kawaguchi, J.: Development of first solar power sail demonstrator - IKAROS. In: *21st International Symposium on Space Flight Dynamics, ISSFD 2009*, 1. 2009.
- [18] The Planetary Society: LightSail: Flight by Light for CubeSats. 2018. Available at: <http://www.planetary.org/explore/projects/lightsail-solar-sailing/>
- [19] Castillo-Rogez, J. and Johnson, L.: Near Earth Asteroid Scout Mission. *11th Meeting of the NASA Small Bodies Assessment Group*, 2014. Available at: <http://www.lpi.usra.edu/sbag/meetings/jul2014/presentations/0930{ }Thu{ }Castillo{ }NEAScout.pdf>
- [20] Betts, B., Spencer, D.A., Nye, B., Munakata, R., Bellardo, J.M., Wong, S.D., Diaz, A., Ridenoure, R.W., Plante, B.A., Foley, J.D. and Vaughn, J.: LightSail 2 : Controlled Solar Sailing Using a CubeSat. In: *4th International Symposium on Solar Sailing*. Kyoto, Japan, 2017. Available at: <https://planetary.s3.amazonaws.com/projects/lightsail/papers/betts-et-al-2017-ls-2.pdf>
- [21] Sloss, P.: EM-1 Update: Making progress, but still behind schedule. 2018. Available at: <https://www.nasaspaceflight.com/2018/04/em-1-update-progress-still-behind-schedule/>
- [22] Peloni, A., Dachwald, B. and Ceriotti, M.: Multiple NEA Rendezvous Mission : Solar Sailing Options. In: *4th International Symposium on Solar Sailing*. Kyoto, Japan, 2017.

- [23] Few, A., Lockett, T., Wilson, R. and Boling, D.: Testing and Development of the NEA Scout Solar Sail Deployer Mechanism. In: *44th Aerospace Mechanisms Symposium*, pp. 323–336. Cleveland, Ohio, 2018.
Available at:
<https://ntrs.nasa.gov/archive/nasa/casi.ntrs.nasa.gov/20180002828.pdf>
- [24] Sorbey, A.R. and Lockett, T.R.: Design and Development of NEA Scout Solar Sail Deployer Mechanism. 2016.
Available at: <https://ntrs.nasa.gov/search.jsp?R=20160008143>
- [25] Okada, T., Iwata, T., Matsumoto, J., Chujo, T., Kebukawa, Y., Aoki, J., Kawai, Y., Yokota, S., Saito, Y., Terada, K., Toyoda, M., Ito, M., Yabuta, H., Yurimoto, H., Okamoto, C., Matsuura, S., Tsumura, K., Yonetoku, D., Mihara, T., Matsuoka, A., Nomura, R., Yano, H., Hirai, T., Nakamura, R., Ulamec, S., Jaumann, R., Bibring, J.-p., Grand, N., Szopa, C., Palomba, E., Helbert, J., Herique, A., Grott, M., Auster, A., Klingelhofer, G., Saiki, T., Kato, H., Mori, O. and Kawaguchi, J.: Science and Exploration in the Solar Power Sail Okeanos Mission To a Jupiter Trojan Astroid. *49th Lunar and Planetary Science Conference 2018*, vol. 2018, no. 2083, pp. 9–10, 2018.
- [26] Mori, O., Kato, H., Matsumoto, J., Saiki, T., Tsuda, Y., Ogawa, N., Tsukizaki, R., Hosoda, S., Bando, N., Yamada, K., Okada, T., Okamoto, C., Matsuura, S., Yonetoku, D., Matsuoka, A. and Nomura, R.: Direct Exploration of Jupiter Trojan Asteroid using Solar Power Sail. In: *4th International Symposium on Solar Sailing*. Kyoto, Japan, 2017.
- [27] Matsumoto, J., Kato, H., Okuizumi, N. and Mori, O.: Design of Solar-Power-Sail Membrane for Jovian Trojan Explorer. In: *4th International Symposium on Solar Sailing*, pp. 1–4. Kyoto, Japan, 2017.
- [28] Okuizumi, N., Mori, O., Matsumoto, J., Saito, K., Sakamoto, H., Kayaba, A. and Shirasawa, Y.: Development of Deployment Structures and Mechanisms of Spinning Large Solar Power Sail. In: *4th International Symposium on Solar Sailing*, pp. 3–7. Kyoto, Japan, 2017.
- [29] Jordaan, H.W.: *Spinning Solar Sail: The Deployment and Control of a Spinning Solar Sail Satellite*. Thesis, University of Stellenbosch, 2016.
- [30] Johnson, L., Young, R., Barnes, N., Friedman, L., Lappas, V. and McInnes, C.: Solar sails: Technology and demonstration status. *International Journal of Aeronautical and Space Sciences*, vol. 13, no. 4, pp. 421–427, 2012. ISSN 2093274X.
- [31] Johnson, L., Whorton, M., Heaton, A., Pinson, R., Laue, G. and Adams, C.: NanoSail-D: A solar sail demonstration mission. *Acta Astronautica*, vol. 68, no. 5-6, pp. 571–575, 2011. ISSN 00945765.
Available at: <http://dx.doi.org/10.1016/j.actaastro.2010.02.008>
- [32] Alhorn, D.C., Casas, J.P., Agasid, E.F., Adams, C.L., Laue, G., Kitts, C. and O'Brien, S.: NanoSail-D: The Small Satellite That Could! *25th Annual AIAA/USU Conference on Small Satellites*, pp. 1–15, 2011.
- [33] Lappas, V., Pellegrino, S., Guenat, H., Straubel, M., Steyn, H., Kostopoulos, V., Sarris, E., Takinalp, O., Wokes, S. and Bonnema, A.: DEORBITSAIL: De-orbiting of satellites using solar sails. *2nd International Conference on Space Technology, ICST 2011*, pp. 2–4, 2011.

- [34] Massimiani, C.: DeorbitSail Update and Initial Camera Image. 2015.
Available at: <https://amsat-uk.org/2015/11/13/deorbitSail-update-and-initial-camera-image/>
- [35] Barnes, N.C., Derbes, W.B.C., Player, C.J. and Dierich, B.L.: Sunjammer: A Solar Sail Demonstration. In: *Advances in Solar Sailing*, pp. 115–126. Springer, 2014.
- [36] Viquerat, A., Schenk, M. and Lappas, V.: Functional and Qualification Testing of the InflateSail Technology Demonstrator. *American Institute of Aeronautics and Astronautics*, pp. 1–12, 2016.
- [37] Krebs, G.D.: Gunter's Space Page: CubeSail. 2018.
Available at: https://space.skyrocket.de/doc/_sdat/cubesail.htm
- [38] Burton, R. and Laystrom-Woodard, J.: Initial development of the cubesail/ultrasail spacecraft. , no. August 2014, pp. 1–32, 2004.
Available at: [http://onlinelibrary.wiley.com/doi/10.1002/cbdv.200490137/abstract%5Cnhttp://cuaerospace.com/pdfs/JANNAF_{_}Burton_{_}2010\(2\).pdf](http://onlinelibrary.wiley.com/doi/10.1002/cbdv.200490137/abstract%5Cnhttp://cuaerospace.com/pdfs/JANNAF_{_}Burton_{_}2010(2).pdf)
- [39] Nakanishi, H., Sakamoto, H., Furuya, H., Yamazaki, M., Miyazaki, Y., Watanabe, A., Watanabe, K., Torisaka-Kayaba, A. and Oda, M.: Development of Nano-Satellite OrigamiSat-1 with Highly Functional Deployable Membrane. In: *4th International Symposium on Solar Sailing*, pp. 2–5. Kyoto, Japan, 2017.
- [40] Hohmann, B., Sakamoto, H., Furuya, H. and Okuizumi, N.: Verification of numerical deployment analysis for membrane structures using micro-gravity experiment. *AIAA Spacecraft Structures Conference, 2018*, , no. 210019, pp. 1–9, 2018.
- [41] Plante, B.A., Spencer, D.A., Betts, B., Chait, S., Bellardo, J.M., Diaz, A. and Pham, I.: LightSail 2 ADCS : From Simulation to Mission Readiness. In: *4th International Symposium on Solar Sailing*. Kyoto, Japan, 2017.
- [42] Lockett, T.R., Few, A. and Wilson, R.: Near Earth Asteroid Solar Sail Engineering Development Unit Test Program. In: *4th International Symposium on Solar Sailing*, pp. 2–6. Kyoto, Japan, 2017.
- [43] Sproewitz, T., Seefeldt, P., Grundmann, J.-t., Spietz, P., Toth, N., Hillebrandt, M., Straubel, M. and Zander, M.: Design of the Gossamer-1 Deployment Demonstrator. In: *4th International Symposium on Solar Sailing*, pp. 1–7. Kyoto, Japan, 2017.
- [44] Lappas, V., Adeli, N., Visagie, L., Fernandez, J., Theodorou, T., Steyn, W. and Perren, M.: CubeSail: A low cost CubeSat based solar sail demonstration mission. Tech. Rep. 11, 2011.
Available at: <http://dx.doi.org/10.1016/j.asr.2011.05.033>
- [45] Nerovny, N., Mayorova, V., Tenenbaum, S., Rachkin, D. and Kotsur, O.: BMSTU-Sail Space Experiment. In: *4th International Symposium on Solar Sailing*, January 2010, pp. 1–5. Kyoto, Japan, 2017.
- [46] United Nations Office For Outer Space Affairs and Committee on the Peaceful Uses of Outer Space: Space Debris Mitigation Guidelines of the Committee on the Peaceful Uses of Outer Space. *United Nations Publication*, p. 1, 2010. ISSN 02784017. SalesNo.E.99.I.17.
Available at: http://www.unoosa.org/pdf/publications/st_{_}space_{_}49E.pdf

- [47] Forshaw, J.L., Aglietti, G.S., Navarathinam, N., Kadhem, H., Salmon, T., Pisseloup, A., Joffre, E., Chabot, T., Retat, I., Axthelm, R., Barraclough, S., Ratcliffe, A., Bernal, C., Chaumette, F., Pollini, A. and Steyn, W.H.: RemoveDEBRIS: An in-orbit active debris removal demonstration mission. *Acta Astronautica*, vol. 127, no. 2016, pp. 448–463, 2016. ISSN 00945765. [j.actaastro.2016.06.018](https://doi.org/10.1016/j.actaastro.2016.06.018). Available at: <http://dx.doi.org/10.1016/j.actaastro.2016.06.018>
- [48] Inoue, S., Tamura, A., Tada, N. and Miyazaki, Y.: Dynamic Characteristics of Self-Deployable Structure Consisting of Tape Springs. In: *International Symposium on Space Technology and Science*, pp. 1–6. Kobe-Hyogo, Japan, 2015. ISSN 0022-3913. Available at: https://archive.ists.or.jp/upload/_pdf/2015-c-21.pdf
- [49] Tada, N., Inoue, S., Miyazaki, Y. and Yamazaki, M.: Membrane Deployment de-orbit System by Convex Tapes. *4th AIAA Spacecraft Structures Conference*, , no. January, pp. 1–12, 2017. Available at: <http://arc.aiaa.org/doi/10.2514/6.2017-0619>
- [50] Peral, E., Im, E., Wye, L., Lee, S., Tanelli, S., Rahmat-Samii, Y., Horst, S., Hoffman, J., Yun, S.H., Imken, T. and Hawkins, D.: Radar Technologies for Earth Remote Sensing from CubeSat Platforms. *Proceedings of the IEEE*, vol. 106, no. 3, pp. 404–418, 2018. ISSN 00189219.
- [51] Wye, L., Lee, S., Buonocore, J., Stevens, T., Novosolev, R., Watt, D., Chen, S., Wilhelm, J., Rennich, P. and Zebker, H.: SRI CubeSat Imaging Radar for Earth Science (SRI-CIRES). In: *Earth Science Technology Forum*, June. SRI International, 2016.
- [52] Warren, P., Steinbeck, J., Minelli, R. and Mueller, C.: Large, Deployable S-Band Antenna for a 6U Cubesat. In: *AIAA/USU Conference on Small Satellites*. Logan, UT, 2015. Available at: <http://digitalcommons.usu.edu/smallsat/2015/all2015/41>
- [53] Steiner, M., Freeland, B. and Veal, G.: Preliminary Mission Report: Spartan 207 / Inflatable Antenna Experiment Flown on STS-77. Tech. Rep., NASA, 1997.
- [54] Fulton, J.A. and Schaub, H.: Fixed-axis electric sail deployment dynamics analysis using hub-mounted momentum control. *Acta Astronautica*, vol. 144, no. March 2017, pp. 160–170, 2018. ISSN 00945765. Available at: <https://doi.org/10.1016/j.actaastro.2017.11.048>
- [55] Lightsey, P.A., Atkinson, C., Clampin, M. and Feinberg, L.D.: James Webb Space Telescope: large deployable cryogenic telescope in space. *Optical Engineering*, vol. 51, no. 1, p. 011003, 2012. ISSN 0091-3286. Available at: <http://opticalengineering.spiedigitallibrary.org/article.aspx?doi=10.1117/1.OE.51.1.011003>
- [56] NASA: James Webb Space Telescope. Available at: <https://jwst.nasa.gov>
- [57] The Space Telescope Science Institute: The James Webb Space Telescope. Available at: <http://webbtelescope.org/>
- [58] McElwain, M.W., Niedner, M.B., Bowers, C.W., Kimble, R.A., Smith, E.C. and Clampin, M.: The James Webb Space Telescope : Observatory Status and Preparations for Launch (Conference Presentation). In: *Space Telescopes and Instrumentation 2018: Optical, Infrared, and Millimeter Wave*. International Society for Optics and Photonics, 2018.

- [59] Daukantas, P.: Breakthrough Starshot. *Optics and Photonics News*, vol. 1047-6938, no. May, pp. 26–33, 2017. ISSN 15413721.
Available at: <http://breakthroughinitiatives.org/Initiative/3>
- [60] Popkin, G.: First Trip To the Stars. *Nature*, vol. 542, pp. 20–22, 2017.
- [61] Breakthrough Initiatives: Breakthrough Starshot Challenges. 2018.
Available at: <http://breakthroughinitiatives.org/challenges/3>
- [62] Matloff, G.L.: Thermal Limitations of Starwisp-Type Interstellar Probes. In: *4th International Symposium on Solar Sailing*, 1, pp. 1–5. Kyoto, Japan, 2017.
- [63] Christian, P. and Loeb, A.: Interferometric Measurement of Acceleration at Relativistic Speeds. *The Astrophysical Journal Letters*, vol. 834, no. 2, pp. 1–5, 2016. ISSN 20418213. 1608.08230.
Available at: <http://arxiv.org/abs/1608.08230>
<http://dx.doi.org/10.3847/2041-8213/834/2/L20>
- [64] Bandyopadhyay, S., Subramanian, G.P., Foust, R., Morgan, D., Chung, S.-J. and Hadaegh, F.: A Review of Impending Small Satellite Formation Flying Missions. *53rd AIAA Aerospace Sciences Meeting*, pp. 1–17, 2015.
Available at: <http://arc.aiaa.org/doi/10.2514/6.2015-1623>
- [65] Manchester, Z., Peck, M. and Filo, A.: KickSat : A Crowd-Funded Mission To Demonstrate The World’s Smallest Spacecraft. *Annual AIAA/USU Conference on Small Satellites*, pp. SSC13–IX–5, 2013.
- [66] Lai, S., Mahon, H. and Smiddy, M.: Dynamics of Wire Boom Oscillations on a Spinning Satellite Part 1, Lagrangian Equations of Motion and Transient Response. *Journal of Applied Mathematics and Physics (ZAMP)*, vol. 30, no. 1, pp. 1–11, 1979.
Available at: <https://link.springer.com/article/10.1007/s00033-019-01597-4>
- [67] Morbhat, P.: *Wire Boom Deployment Dynamics and Control System Model for Small Satellites*. Ph.D. thesis, 2012.
- [68] Auslander, D., Cermenska, J., Dalton, G., De La Pena, M., Dharan, C.K., Donokowski, W., Duck, R., Kim, J., Pankow, D., Plauche, A., Rahmani, M., Sulack, S., Tan, T.F., Turin, P. and Williams, T.: Instrument boom mechanisms on the THEMIS satellites; Magnetometer, radial wire, and axial booms. *Space Science Reviews*, vol. 141, no. 1-4, pp. 185–211, 2008. ISSN 00386308.
- [69] Fish, C., Swenson, C., Neilsen, T., Bingham, B., Gunther, J., Stromberg, E., Burr, S., Burt, R., Whitely, M. and Petersen, J.: DICE Mission Design, Development, and Implementation: Success and Challenges. *26th Annual AIAA/USU Conference on Small Satellites*, 2012.
- [70] Minguzzi, E.: Rayleigh’s Dissipation Function at Work. *European Journal of Physics*, vol. 36, no. 3, pp. 1–10, 2015. ISSN 13616404. 1409.4041.
Available at:
<http://iopscience.iop.org/article/10.1088/0143-0807/36/3/035014/pdf>
- [71] Bradford, K.R.: *Miniature Wire Boom System for Cubsat Application*. Ph.D. thesis, Utah State University, 2013.
- [72] Austria Micro Systems: AS5040 Rotary Sensor. 2018.
Available at: <https://ams.com/as5040>

- [73] Pololu Corporation: Pololu G2 High-Power Motor Driver 24v21. 2018.
Available at: <https://www.pololu.com/product/2995>
- [74] ACE: *ACE Damping Technology Main Catalogue 2016*. Issue 11.2 edn. ACE (Automation Control Equipment), 2016.
- [75] Kapelevich, A. and Taye, E.: Applications for Self-Locking Gears. 2012.
Available at: http://gearsolutions.com/media/uploads/uploads/assets/PDF/Articles/May_{_}12/0512_{_}Kapplavich.pdf
- [76] Faulhaber: DC-Gearmotors Precious Metal Commutation with integrated Encoder 100 mNm Series 2619 ... SR ... IE2-16. 2018.
Available at: https://www.faulhaber.com/fileadmin/Import/Media/EN_{_}2619_{_}SR_{_}IE2-16_{_}DFD.pdf
- [77] Mehrpavar, A., Pignatelli, D., Carnahan, J., Munakata, R., Lan, W., Toorian, A., Hutputanasin, A. and Lee, S.: Cubesat design specification. *The CubeSat Program, California Polytechnic State ...*, 13. ISSN 1110662X.